Title
Power Control and Optimization of Photovoltaic and Wind Energy Conversion Systems /

Author
Ghaffari, Azad

Publication Date
2013

UNIVERSITY OF CALIFORNIA, SAN DIEGO

SAN DIEGO STATE UNIVERSITY

Power Control and Optimization of Photovoltaic and Wind Energy Conversion Systems

A dissertation submitted in partial satisfaction of the
requirements for the degree
Doctor of Philosophy

in

Engineering Science (Mechanical and Aerospace Engineering)

by

Azad Ghaffari

Committee in charge:

University of California, San Diego

Professor Miroslav Krstić, Chair
Professor Robert Bitmead
Professor Farrokh Najmabadi

San Diego State University

Professor Sridhar Seshagiri, Co-Chair
Professor Gordon Lee

2013

The dissertation of Azad Ghaffari is approved, and it is acceptable in quality and form for publication on microfilm and electronically:

Co-Chair

Chair

University of California, San Diego
San Diego State University

2013

DEDICATION

To Farinaz.

TABLE OF CONTENTS

LIST OF FIGURES

LIST OF TABLES

ACKNOWLEDGEMENTS

Undoubtedly, Prof. Krstić has been a great support and a trustful source of advise from the point I decided to join the Joint Doctoral Program (JDP). His remarkable insight and his concise thinking always have been my best companions during the term of my study. These few words of gratitude by no means can respond all his supports and concerns in my favor.

From my first contact with the JDP and during the lengthy application process, Prof. Seshagiri showed unusual amount of care and help in my support. He has been more than an intelligent critical advisor for me and I am proud to count him as one of my closest friends. Without his persistent support and his leading management role to interact with the JDP this work could have not been done.

I started this work with establishing an academic connection with Prof. Nesić at The University of Melbourne. I am grateful for his comments and view points on the theoretical expansion of the Newton-based Extremum seeking.

I also would like to thank my Doctoral Committee members to their time, effort, and willing to read this dissertation.

To Donovan Geiger, thank you for your help and advise in the JDP.

My words are speechless in response to the unconditional love and friendship I have received from Farinaz, my wife. We have been students together in these years and she showed a great deal of courage and hardworking both in her school and in our life.

My mother, Khadijeh, and my sister, Golaleh, are both deserved special thanks for their unexpected supports during this work. Farinaz's Father, Ebrahim, is obviously one of those people who cannot be found very often. I would like to thank them for their endless favors in our support which we will never forget.

I would like to extend my gratitude to my friend, Aziz Rasouli, whom is like an older brother and a source of wisdom to me.

This dissertation includes reprints or adaptations of the following papers:

A. Ghaffari, M. Krstić, and D. Nesić,"Multivariable Newton-Based Extremum

Seeking," *Automatica*, vol. 48, pp. 1759-1767, 2012. (Chapter 2)

A. Ghaffari, S. Seshagiri, and M. Krstić, "High-fidelity PV array modeling for advanced MPPT design," in *Proc. of IEEE Canadian Conference on Electrical and Computer Engineering*, 2012. (Chapter 3)

A. Ghaffari, S. Seshagiri, and M. Krstić, "High-fidelity DC-DC converter modeling for advanced MPPT design," in *Proc. of IEEE Canadian Conference on Electrical and Computer Engineering*, 2012. (Chapter 3)

A. Ghaffari, M. Krstić, and S. Seshagiri, "Power Optimization for Photovoltaic Micro-Converters using Multivariable Newton-Based Extremum-Seeking," in *Proc. of IEEE Conference on Decision and Control*, 2012. (Chapter 4)

A. Ghaffari, S. Seshagiri, and M. Krstić, "Power Optimization for Photovoltaic Micro-Converters using Multivariable Gradient-Based Extremum-Seeking," Submitted to the *IEEE Transactions on Industrial Electronics.* (Chapter 4)

A. Ghaffari, M. Krstić, and S. Seshagiri, "Power Optimization and Control in Wind Energy Conversion Systems using Extremum Seeking," Submitted to the *IEEE Transactions on Control Systems Technology.* (Chapter 5)

The dissertation author is the primary author in these publications.

VITA

2001	B. S. in Electrical Engineering, K. N. Toosi University of Technology, Tehran, Iran
2004	M. S. in Control Engineering, K. N. Toosi University of Technology, Tehran, Iran
2004-2006	Design Engineer, Conscription, Tehran, Iran
2006-2007	Research Engineer, Niroo Research Institute, Tehran, Iran
2007	Instructor of Electrical Engineering, Azad University, Sanandaj, Kurdistan, Iran
2007-2009	Design Engineer, Monenco Iran Company, Tehran, Iran
2013	Ph. D. in Engineering Science (Mechanical and Aerospace Engineering), Joint Doctoral Program between University of California, San Diego and San Diego State University, CA, USA

PUBLICATIONS

A. Ghaffari, S. Seshagiri, and M. Krstić, "Power Optimization for Photovoltaic Micro-Converters using Multivariable Gradient-Based Extremum Seeking," Submitted to the *IEEE Transactions on Industrial Electronics*.

A. Ghaffari, M. Krstić, and S. Seshagiri, "Power Optimization and Control in Wind Energy Conversion Systems using Extremum Seeking," Submitted to the *IEEE Transactions on Control Systems Technology*.

A. Ghaffari, M. Krstić, and D. Nesić,"Multivariable Newton-Based Extremum Seeking," *Automatica*, vol. 48, pp. 1759-1767, 2012.

A. Ghaffari, M. Krstić, and S. Seshagiri, "Power Optimization and Control in Wind Energy Conversion Systems using Extremum Seeking," *Accepted in the American Control Conference*, 2013.

A. Ghaffari, M. Krstić, and S. Seshagiri, "Power Optimization for Photovoltaic Micro-Converters using Multivariable Newton-Based Extremum-Seeking," in *Proc. of IEEE Conference on Decision and Control*, 2012.

A. Ghaffari, S. Seshagiri, and M. Krstić, "High-fidelity PV array modeling for advanced MPPT design," in *Proc. of IEEE Canadian Conference on Electrical and Computer Engineering*, 2012.

A. Ghaffari, S. Seshagiri, and M. Krstić, “High-fidelity DC-DC converter modeling for advanced MPPT design,” in *Proc. of IEEE Canadian Conference on Electrical and Computer Engineering*, 2012.

A. Ghaffari, S. Seshagiri, and M. Krstić, “Power Optimization for Photovoltaic Micro-Converters using Multivariable Gradient-Based Extremum-Seeking,” in *Proc. of American Control Conference*, 2012.

A. Ghaffari, M. Krstic, and D. Nesić, “Multivariable Newton-Based Extremum Seeking,” in *Proc. of IEEE Conference on Decision and Control*, 2011.

ABSTRACT OF THE DISSERTATION

Power Control and Optimization of Photovoltaic and Wind Energy Conversion Systems

by

Azad Ghaffari

Doctor of Philosophy in Engineering Science (Mechanical and Aerospace Engineering)

University of California, San Diego, 2013
San Diego State University, 2013

Professor Miroslav Krstić, Chair
Professor Sridhar Seshagiri, Co-Chair

Power map and Maximum Power Point (MPP) of Photovoltaic (PV) and Wind Energy Conversion Systems (WECS) highly depend on system dynamics and environmental parameters, e.g., solar irradiance, temperature, and wind speed. Power optimization algorithms for PV systems and WECS are collectively known as Maximum Power Point Tracking (MPPT) algorithm. Gradient-based Extremum Seeking (ES), as a non-model-based MPPT algorithm, governs the system to its peak point on the steepest descent curve regardless of changes of the system dynamics and variations of the environmental parameters. Since the power map

shape defines the gradient vector, then a close estimate of the power map shape is needed to create user assignable transients in the MPPT algorithm. The Hessian gives a precise estimate of the power map in a neighborhood around the MPP. The estimate of the inverse of the Hessian in combination with the estimate of the gradient vector are the key parts to implement the Newton-based ES algorithm. Hence, we generate an estimate of the Hessian using our proposed perturbation matrix. Also, we introduce a dynamic estimator to calculate the inverse of the Hessian which is an essential part of our algorithm. We present various simulations and experiments on the micro-converter PV systems to verify the validity of our proposed algorithm.

The ES scheme can also be used in combination with other control algorithms to achieve desired closed-loop performance. The WECS dynamics is slow which causes even slower response time for the MPPT based on the ES. Hence, we present a control scheme, extended from Field-Oriented Control (FOC), in combination with feedback linearization to reduce the convergence time of the closed-loop system. Furthermore, the nonlinear control prevents magnetic saturation of the stator of the Induction Generator (IG). The proposed control algorithm in combination with the ES guarantees the closed-loop system robustness with respect to high level parameter uncertainty in the IG dynamics. The simulation results verify the effectiveness of the proposed algorithm.

Chapter 1

Introduction

Environmental parameters and systems dynamics are two main factors which affect the power map of Distributed Generators (DG), including Photovoltaic (PV) and Wind Energy Conversion Systems (WECS). Since the DG systems are exposed to the sun and wind for a long period of time they experience degradation in addition to normal wear and tear, which cause variation of the power map in unpredictable ways. Also the DG systems have a peak power point which moves with system degradation and environmental parameters. Figure 1.1 shows a typical power map of the PV and WECS under a wide range of temperature, solar irradiance, and wind speed. Maximum Power Point Tracking (MPPT) algorithms are designed to guarantee maximum power extraction independent of system dynamics or environmental parameters.

1.1 Model-Free Gradient-Based Optimization Algorithms

One of the most common algorithms to MPPT in the DG systems are based on the idea of Perturb and Observe (P& O) which has other derivations like Hill Climbing (HC) and Increment Conductance (IC) methods. More details and thorough investigation on these methods can be found in [25, 32, 35]. A basic HC algorithm is shown in Fig. 1.2. This algorithm moves the system to its peak point

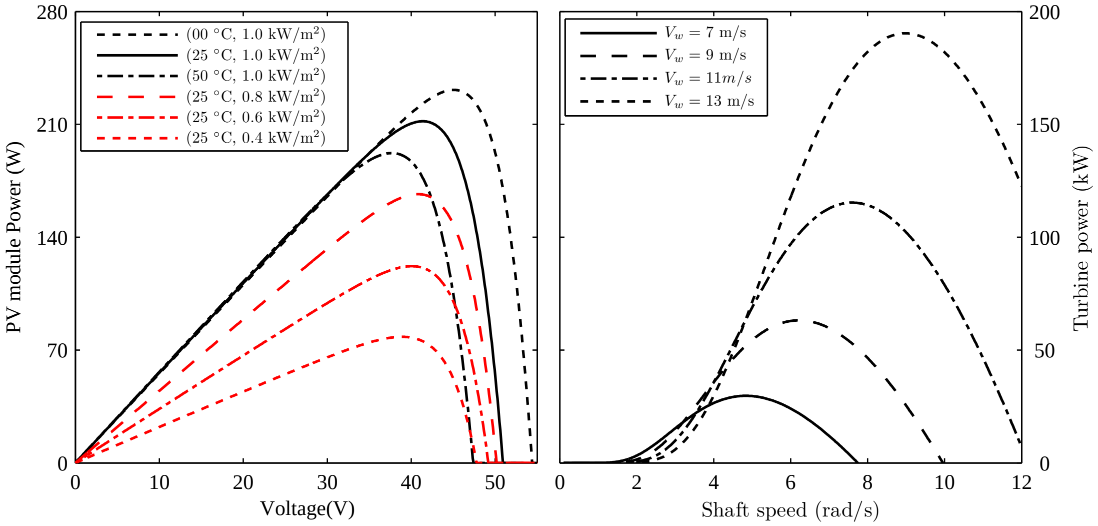

Figure 1.1: Typical power map of PV and WECS under different environmental conditions.

by detecting the gradient of the cost function. There is not a generalization of the P& O techniques for cost functions with input vector parameter, multivariable maps, which motivates the researcher to employ other techniques, among which we refer the reader to [53, 63]. Reference [53] uses Particle Swarm Optimization (PSO), which is an algorithm that employs multiple agents to "search" for the peak power. When applying this technique for MPPT of a PV system including a group of PV modules in series and parallel, the process of reinitialization and the tracking performance depend strongly on variable conditions like environmental factors, the nature of the PV modules, and the shading area. The method also has a lengthy adaptation time. The presented algorithm in [63] computes the optimal parameter at each dimension of the input vector parameter, one after the other one. Obviously, because the latter algorithm does not give an estimate of the gradient vector of the cost function, then this so-called multivariable P& O technique may fail to find the Maximum Power Point (MPP) of a PV system under partial shading or sudden changes in solar irradiance.

Among the gradient-based MPPT algorithm we select Extremum Seeking (ES) which its local stability has been analytically proved and its expansion to

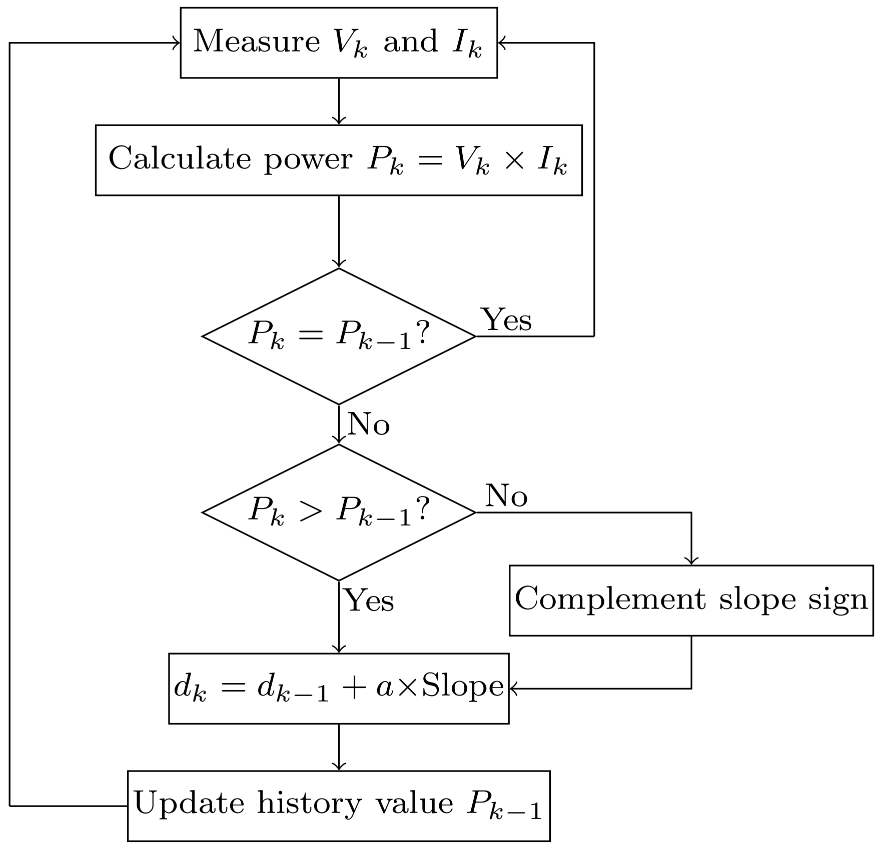

Figure 1.2: Hill climbing algorithm to MPPT in DG systems.

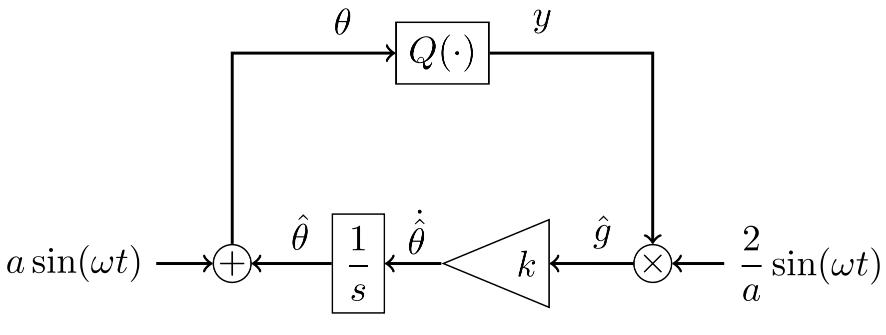

Figure 1.3: Scalar extremum seeking for a static cost function.

MPPT of multivariable cost functions is fairly straight forward. Figure 1.3 shows a basic scheme of the gradient-based ES for a static map $Q(\theta)$ with peak value Q^* at θ^*. Suppose that we have the following quadratic cost function

$$Q(\theta) = Q^* + \frac{1}{2}h(\theta - \theta^*)^2, \quad h < 0, \tag{1.1}$$

where h is the Hessian of the cost function and its gradient is $g = h(\theta - \theta^*)$. By injecting a perturbation signal with low amplitude and low frequency and multiplying the output of the system by the same perturbation with a properly scaled amplitude, we can calculate the estimate of the gradient of the cost function as follows

$$\begin{align}
Q(\theta) &= Q^* + \frac{1}{2}h\left(\tilde{\theta} + a\sin(\omega t)\right), \quad \tilde{\theta} = \hat{\theta} - \theta^* \tag{1.2}\\
\hat{g} &= \frac{2}{a}\sin(\omega t) \times y \tag{1.3}\\
&= h\tilde{\theta} + \frac{2}{a}Q^*\sin(\omega t) + \frac{h}{a}\sin(\omega t)\tilde{\theta}^2 - h\cos(2\omega t)\tilde{\theta} + ha\sin^3(\omega t) \tag{1.4}
\end{align}$$

The average value of $\hat{g}$ over one period of the probing function equals to the average value of the gradient

$$\begin{align}
\hat{g}^{ave} &= \frac{1}{T}\int_0^T \hat{g}\mathrm{d}t, \quad T = \frac{2\pi}{\omega} \tag{1.5}\\
&= h\tilde{\theta}. \tag{1.6}
\end{align}$$

Since $\dot{\tilde{\theta}} = \dot{\hat{\theta}}$, then $\dot{\tilde{\theta}} = kh\tilde{\theta}$, which shows that the Hessian defines transient of the closed-loop system. A simple simulation can explain this issue more clearly. Applying the gradient-based ES to a scalar non-symmetric cost function as shown in Fig. 1.4 results in vastly different transients for different initial conditions. Clearly, the shape of the cost function has a great impact on the convergence rate of the parameter. This issue can create more complicated transient performances in a multivariable cost functions. Newton algorithm is an apparent option to overcome the challenges of the gradient-based algorithm for which we need the estimate of the Hessian and its inverse.

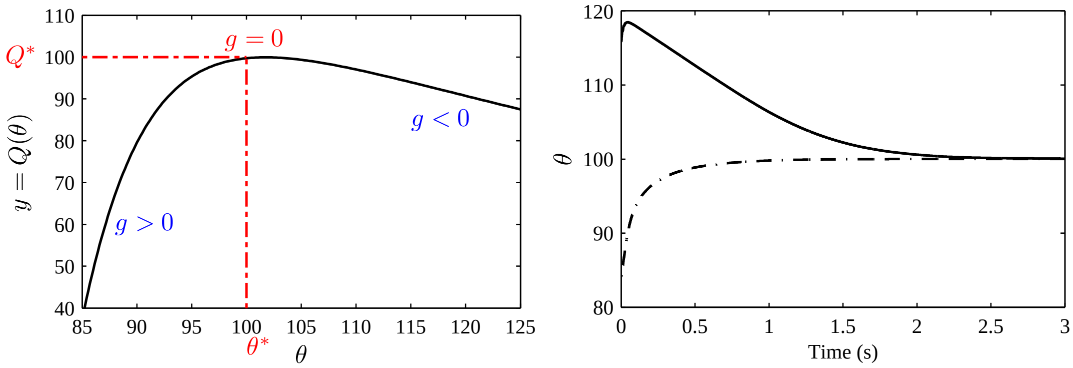

Figure 1.4: (left) A sample non-symmetric cost function and (right) the adaptation process using gradient-based ES for two different initial conditions.

1.2 Newton-based ES

First we develop theoretical basis of Newton-based ES for multivariable cost functions with dynamic systems. The traditional ES is based on the estimate of the gradient vector of the cost function which causes the dependence of the convergence rate on the cost function shape. For non-symmetric cost functions which are elongated in one direction the governing process is non-uniform which creates a lengthy adaptation process including a wide range of transients for different parameters. To maintain the same transient and to guarantee a reasonable convergence time, the designer needs to select the gain matrix cautiously with an eye on the selected perturbation frequencies for the gradient-based ES. The Newton-based ES uses the estimate of the Hessian which is an indication of the cost function shape to create a uniform transient in all channels of the ES algorithm. The proposed scheme includes two main parts: first we present an estimate of the Hessian by generating a perturbation matrix which includes sinusoidal signals, then we develop a dynamic matrix inverter algorithm to ensure avoiding singularities in the inverse of the Hessian. The presented nonlinear filter is in the shape of a Riccati equation.

1.3 Maximum Power Point Tracking

Since PV and WECS power level are defined by the environmental parameters like solar irradiance and wind speed, we use ES which is a non-model-based power optimization algorithm to remove the obstacle of working with an unknown system model. Extremum seeking has the ability to deal with unknown dynamics by reducing the design requirements to two basic assumptions about the cost function, namely zero gradient vector and negative definite Hessian matrix around the peak point.

Photovoltaic systems include an arbitrary combination of series and parallel PV modules to create a desired power and voltage level. In order to extract power from PV modules we construct our system based on the micro-converter scheme (DC power optimizer) which involves one DC/DC converter per each PV module. The micro-converter architecture guarantees the highest economical level of power extraction from PV systems. Each DC/DC converter has two roles: first it regulates the voltage level to a constant value and second it implements the MPPT algorithm to ensure power maximization. Conventionally, one MPPT algorithm is employed per each module in the micro-converter scheme which requires two sensors per each PV module, one for current and one for voltage measurement. Also this distributed MPPT structure gives no consideration to the interaction between modules and creates vastly different transients under sudden changes in irradiance level or partial shading. We present a centralized MPPT algorithm using multivariable ES to keep all the PV modules under the same transient. Since the centralized algorithm uses the total generated power of the PV system for MPPT, then the number of sensors reduces to two for the entire system, one for current and one for voltage measurement. We also develop an experimental setup to validate our proposed MPPT algorithm.

As shown in Fig. 1.1 the WECS shows different peak points under various wind speeds. In order to find the optimal shaft speed of the WECS under any wind speed regime, a close estimate of the WECS power map and wind speed measurement are required. Nevertheless, non-model-based optimization algorithms like the ES do not require the information about system power map and wind speed measurement. Hence, we employ a gradient-based ES for MPPT of the WECS. The system includes a Matrix Converter (MC) as the control actuator which governs the electrical frequency and voltage amplitude of the Induction Generator (IG) to desired values. The open-loop dynamics of the WECS is stable with left half-plane poles in the linearized model. In order to improve the transient of the WECS and and to encompass other control features like v/f or Field-Oriented Control (FOC), a controller needs to be included in the system. We employ a nonlinear control developed based on the FOC to achieve a fast transient and to prevent magnetic saturation of the IG stator. The proposed controller in combination with the ES is highly robust with respect to the variation in the IG parameters.

1.4 Thesis Overview

The contents of this thesis are as follows.

Chapter 2 develops the theoretical basis of multivariable Newton-based ES using the averaging and singular perturbation analysis.

Chapter 3 describes the fundamentals of PV module modeling based on the manufacturer's data sheet. This chapter also provides the design guidelines for buck and boost DC/DC power converters for MPPT in PV systems.

Chapter 4 is dedicated to MPPT of PV systems using the ES including multivariable Newton-based, multivariable gradient-based, and distributed ES. We present the simulation and experimental results to show the effectiveness of the proposed algorithms.

Chapter 5 concentrates on the WECS modeling and its MPPT. We employ a nonlinear transformation and feedback linearization based on the concept of the FOC to achieve desired closed-loop performance. Power optimization is implemented using ES.

Chapter 6 presents a summary of this dissertation and presents an overview of the future work direction.

Chapter 2

Multivariable Newton-Based Extremum Seeking

In this chapter we develop the theoretical basis of the Newton-based ES using the averaging and singular perturbation analysis. Our main contributions are presenting a disturbance matrix to create a precise estimate of the Hessian and providing the estimate of the inverse of the Hessian using a dynamic filter in form of a Riccati equation. User assignable transient performance occurs in all channels of the input vector parameter.

2.1 Introduction

Dramatic advances have occurred over the past decade both in the theory [5, 6, 20, 45, 66, 70–73, 76] and in applications [7, 10, 17, 21, 22, 31, 41, 51, 77, 81] of Extremum Seeking (ES) control. All these references employ gradient-based ES.

A Newton-based ES algorithm was introduced in [54] where, for the single-input case, an estimate of the second derivative of the map was employed in a Newton-like continuous-time algorithm. A generalization, employing a different approach than in [54], was presented in [56], where a methodology for generating estimates of higher-order derivatives of the unknown single-input map was introduced, for emulating more general continuous-time optimization algorithms, with a Newton algorithm being a special case.

The key distinction of the Newton algorithm relative to the gradient algorithm is that, while the convergence of the gradient algorithm is dictated by the second derivative (Hessian) of the map, the convergence of the Newton algorithm is independent of the Hessian and can be arbitrarily assigned. This is particularly important in non-model based algorithms, like extremum seeking, where the Hessian is unknown.

The power of the Newton algorithm is particularly evident in multi-input optimization problems. With the Hessian being a matrix in this case, and with it being typically very different from the identity matrix, the gradient algorithm typically results in different elements of the input vector converging at vastly different speeds. This problem is inherent to gradient-based schemes. To rectify it one would need to modify the algorithm using the inverse of the Hessian matrix which is not available as the model of the system is assumed to be unavailable. On the other hand, the Newton algorithm, if equipped with a convergent estimator of the Hessian matrix, achieves convergence of all the elements of the input vector at the same, or at arbitrarily assignable, rates.

We present a multivariable Newton-based ES algorithm, which yields arbitrarily assignable convergence rates for each of the elements of the input vector. We generate the estimate of the Hessian matrix by generalizing the idea proposed in [56] for the scalar case.

Generating an estimate of the Hessian matrix in non-model-based optimization is not the only challenge. The other challenge is that the Newton algorithm requires an inverse of the Hessian matrix. The estimate of this matrix, as it evolves in continuous time, need not necessarily remain invertible. We tackle this challenge by employing a dynamic system for generating the inverse asymptotically. This dynamic system is a filter in the form of a Riccati differential equation. When fed with a positive/negative-definite estimate of the Hessian matrix over a longer period of time, this filter converges to a positive/negative-definite inverse of the Hessian matrix. Hence, after a transient, our non-model-based algorithm behaves (on average) as a model-based Newton algorithm.

While the basic idea of our algorithm is developed for static maps, we provide the analysis of convergence when the algorithm is applied to general nonlinear systems, as in [45]. We apply classical averaging and singular perturbation methods, so our stability result is local—the parameter estimates start not too far from the true parameters and the estimate of the Hessian matrix starts not too far from the true Hessian matrix. It is also possible to prove non-local stability of the proposed scheme in a similar manner as [72] where a gradient-based algorithm was investigated.

The continuous-time Newton algorithm that we propose is novel, to our knowledge, even in the case when the cost function being optimized is known. The state-of-the-art continuous-time Newton algorithm in [3] employs a Lyapunov differential equation for estimating the inverse of the Hessian matrix—see (3.2) in [3]. The convergence of this estimator is actually governed by the Hessian matrix itself. This means that the algorithm in [3] removes the difficulty with inverting the estimate of the Hessian, but does not achieve independence of the convergence rate from the Hessian. In contrast, our algorithm's convergence rate is independent from the Hessian and is user-assignable.

We state the problem and review the gradient-based ES algorithm for a static map in Section 2.2. Section 2.3 presents our Newton-based scheme for the static map. In this section we explain how we generate the estimate of the Hessian matrix and the estimate of its inverse. A generalization of the Newton-based scheme to dynamic plants is introduced in Section 2.4. The main stability result is stated in Section 2.5. Stability analysis based on the averaging and singular perturbation methods is presented, respectively, in Section 2.6 and Section 2.7. Section 2.8 presents an illustrative example to highlight the difference between the proposed scheme and the standard gradient-based ES.

2.2 Review of the Gradient Algorithm for Static Map

Consider a convex static map

$$y = Q(\theta), \quad \theta = \begin{bmatrix} \theta_1 & \theta_2 & \cdots & \theta_n \end{bmatrix}^T, \tag{2.1}$$

with a local maximum at θ^*. The cost function is not known in (2.1), but we can measure y and we can manipulate θ. The gradient-based ES scheme for this multivariable static map is shown in Fig. 2.1, where K is a positive diagonal matrix, and the perturbation signals are defined as

$$S(t) = \begin{bmatrix} a_1 \sin(\omega_1 t) & \cdots & a_n \sin(\omega_n t) \end{bmatrix}^T, \tag{2.2}$$

$$M(t) = \begin{bmatrix} \frac{2}{a_1} \sin(\omega_1 t) & \cdots & \frac{2}{a_n} \sin(\omega_n t) \end{bmatrix}^T, \tag{2.3}$$

where ω_i/ω_j are rational and a_i are real numbers, with the frequencies chosen such that $\omega_i \neq \omega_j$ and $\omega_i + \omega_j \neq \omega_k$ for distinct $i,\ j$, and k.

Remark 1 A gradient-based ES for the static map (2.1) is given by $\dot{\hat{\theta}} = KM(t)y$, $\theta = \hat{\theta} + S(t)$. In the parameter error variable $\tilde{\theta} = \hat{\theta} - \theta^*$, the closed-loop system in Fig. 2.1 is given by $\dot{\tilde{\theta}} = KM(t)Q\left(\theta^* + S(t) + \tilde{\theta}\right)$. The basic idea of the scheme, as well as of the choice of the perturbation signals, is understood by noting that, for the case of a quadratic map, $Q(\theta) = Q^* + \frac{1}{2}(\theta - \theta^*)^T H(\theta - \theta^*)$, the averaged system is given by

$$\dot{\tilde{\theta}} = KH\tilde{\theta}, \tag{2.4}$$

where H is the Hessian of the static map, and it is negative definite. This observation reveals two things: (i) the gradient-based ES algorithm is locally convergent, and (ii) the convergence rate is governed by the unknown Hessian matrix H. One of the features of the Newton algorithm presented in the next section is to eliminate the dependence of the convergence rate on the unknown H.

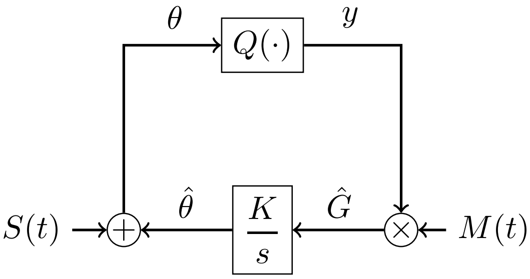

Figure 2.1: Gradient-based ES for a static map.

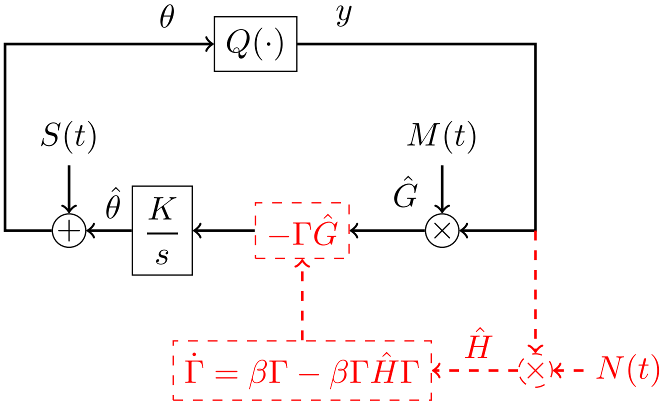

Figure 2.2: Newton-based ES for a static map.

2.3 Newton Algorithm for Static Map

The Newton-based ES algorithm for a static map is shown in Fig. 2.2, where β is a positive real number. There are two vital parts in the Newton-based algorithm: the perturbation matrix $N(t)$, which generates an estimate of the Hessian, and the Riccati equation, which generates an estimate of the inverse of Hessian matrix, even when the estimate of the Hessian is singular.

The idea for producing the estimate of the Hessian matrix $H := \partial^2 Q(\theta^*)/\partial\theta^2$ is borrowed from the scalar design in [56]. Referring to the Taylor series expansion of the cost function around the peak, we have

$$\begin{aligned} y &= Q(\theta^* + \tilde{\theta} + S(t)) \\ &= Q(\theta^*) + \frac{1}{2}\Big(\tilde{\theta} + S(t)\Big)^T H \Big(\tilde{\theta} + S(t)\Big) + R(\tilde{\theta} + S(t)), \end{aligned} \tag{2.5}$$

where $\partial Q(\theta^*)/\partial\theta = 0$ and $R(\tilde{\theta} + S(t))$ stands for higher order terms in $\tilde{\theta} + S(t)$. Product of $N(t)$ and y needs to generate an estimate of the Hessian in an average sense. We show that by an appropriate selection of matrix $N(t)$, the average value of $\hat{H} = N(t)y$ over the period Π, which is related to ω_i's (see (2.10)), is an estimate of the Hessian. We start with

$$\begin{aligned} &\frac{1}{\Pi}\int_0^{\Pi} N(\sigma) y \mathrm{d}\sigma = \\ &= I + J + \bar{H} + \frac{1}{\Pi}\int_0^{\Pi} R(\tilde{\theta} + S(\sigma)) N(\sigma) \mathrm{d}\sigma, \end{aligned} \tag{2.6}$$

$$I := \frac{1}{\Pi}\int_0^{\Pi} \left(Q(\theta^*) + \frac{1}{2}\tilde{\theta}^T H \tilde{\theta} \right) N(\sigma) \mathrm{d}\sigma, \tag{2.7}$$

$$J := \frac{1}{\Pi}\int_0^{\Pi} \tilde{\theta}^T H S(\sigma) N(\sigma) \mathrm{d}\sigma, \tag{2.8}$$

$$\begin{aligned} \bar{H} &:= \frac{1}{\Pi}\int_0^{\Pi} \frac{1}{2} S(\sigma)^T H S(\sigma) N(\sigma) \mathrm{d}\sigma \\ &= \frac{1}{\Pi}\int_0^{\Pi} \frac{1}{2}\sum_{i=1}^{n}\sum_{j=1}^{n} H_{i,j} \sin(\omega_i \sigma) \sin(\omega_j \sigma) N(\sigma) \mathrm{d}\sigma. \end{aligned} \tag{2.9}$$

By taking Π as

$$\Pi = 2\pi \times \mathrm{LCM}\Big\{\frac{1}{\omega_i}\Big\}, \quad i \in \{1,\ 2,\ \cdots\ ,\ n\}, \tag{2.10}$$

where LCM stands for the least common multiple, we have $I = 0$ if N has zero average over Π. Also, taking N such that

$$\frac{1}{\Pi}\int_0^{\Pi} \sin(\omega_i \sigma) N_{j,k}(\sigma) \mathrm{d}\sigma = 0, \tag{2.11}$$

holds for all i, j, and $k \in \{1, 2, \cdots, n\}$, makes the integral J equal to zero.

Furthermore, $\bar{H}$ is equal to H if we choose N such that

$$\frac{1}{\Pi}\int_0^{\Pi} \sin^2(\omega_i\sigma)N_{i,i}(\sigma)\mathrm{d}\sigma \neq 0 \tag{2.12}$$

$$\frac{1}{\Pi}\int_0^{\Pi} \sin(\omega_i\sigma)\sin(\omega_j\sigma)N_{i,j}(\sigma)\mathrm{d}\sigma \neq 0 \tag{2.13}$$

$$\frac{1}{\Pi}\int_0^{\Pi} \sin^2(\omega_i\sigma)N_{i,j}(\sigma)\mathrm{d}\sigma = 0 \tag{2.14}$$

$$\frac{1}{\Pi}\int_0^{\Pi} \sin(\omega_i\sigma)\sin(\omega_j\sigma)N_{i,i}(\sigma)\mathrm{d}\sigma = 0, \tag{2.15}$$

for all distinct i and j. Noting that Π is the common period of the probing frequencies we have

$$\frac{1}{\Pi}\int_0^{\Pi} \sin^2(\omega_i\sigma)\cos(2\omega_i\sigma)\mathrm{d}\sigma = -\frac{1}{4} \tag{2.16}$$

$$\frac{1}{\Pi}\int_0^{\Pi} \sin^2(\omega_i\sigma)\sin^2(\omega_j\sigma)\mathrm{d}\sigma = \frac{1}{4} \tag{2.17}$$

$$\frac{1}{\Pi}\int_0^{\Pi} \sin^3(\omega_i)\sin(\omega_j)\mathrm{d}\sigma = 0 \tag{2.18}$$

$$\frac{1}{\Pi}\int_0^{\Pi} \sin(\omega_i\sigma)\sin(\omega_j\sigma)\cos(2\omega_i\sigma)\mathrm{d}\sigma = 0, \tag{2.19}$$

for all $i \neq j$. Hence, one possible choice of elements of the $n\times n$ matrix $N(t)$ that satisfy all of the aforementioned constraints is given by

$$N_{i,i} = \frac{16}{a_i^2}\Big(\sin^2(\omega_i t) - \frac{1}{2}\Big) \tag{2.20}$$

$$N_{i,j} = \frac{4}{a_i a_j}\sin(\omega_i t)\sin(\omega_j t), \qquad i \neq j, \tag{2.21}$$

where $N^T(t) = N(t)$. Based on this selection, we have

$$\frac{1}{\Pi}\int_0^{\Pi} N(\sigma)y\mathrm{d}\sigma = H + \frac{1}{\Pi}\int_0^{\Pi} R(\tilde{\theta} + S(\sigma))N(\sigma)\mathrm{d}\sigma. \tag{2.22}$$

In Section 2.6 we show that this averaged value converges to the actual value of the Hessian, under specific conditions on ω_i and a_i.

Computing the inverse of the Hessian matrix is the next step. Calculating Γ, the estimate of the inverse of the Hessian, in an algebraic fashion creates difficulties when the matrix $\hat{H}$ is close to singularity, or it is indefinite. To deal with this problem, a dynamic estimator is employed to calculate the inverse of $\hat{H}$ using a Riccati equation. Consider the following filter

$$\dot{\mathcal{H}} = -\beta\mathcal{H} + \beta\hat{H}. \tag{2.23}$$

Note that the state of this filter converges to $\hat{H}$, an estimate of H. Denote Γ=$\mathcal{H}^{-1}$. Since $\dot{\Gamma} = -\Gamma\dot{\mathcal{H}}\Gamma$, then equation (2.23) is transformed to the differential Riccati equation

$$\dot{\Gamma} = \beta\Gamma - \beta\Gamma\hat{H}\Gamma. \tag{2.24}$$

The equilibria of the Riccati equation (2.24) are $\Gamma^* = 0_{n\times n}$ and $\Gamma^* = \hat{H}^{-1}$, provided $\hat{H}$ settles to a constant. Since $\beta > 0$, the equilibrium $\Gamma^* = 0$ is unstable, whereas the linearization of (2.24) around $\Gamma^* = \hat{H}^{-1}$ has the Jacobian $-\beta I$, so the equilibrium at $\Gamma^* = \hat{H}^{-1}$ is locally exponentially stable. This shows that, after a transient, the Riccati equation converges to the actual value of the inverse of Hessian matrix if $\hat{H}$ is a good estimate of H.

A good estimate of the region of attraction of the exponentially stable equilibrium $\Gamma^* = \hat{H}^{-1}$ of (2.24) is difficult to obtain. An easy but conservative estimate makes the region of attraction inversely proportional to the largest eigenvalue of $\hat{H}$, which, due to the convergence of $\hat{H}$ to H, which we shall prove to be achieved locally (in an average sense), means that an estimate of the region of attraction of $\Gamma^* = H^{-1}$ is $1/\lambda_{\max}\{H\}$.

Remark 2 To highlight the contrast between the Newton and gradient algorithms, we refer to Remark 1 where the average behavior of the gradient algorithm is discussed. For the Newton algorithm in Fig. 2.2, the algorithm is given by

$$\dot{\hat{\theta}} = -K\Gamma M(t)y \tag{2.25}$$

$$\dot{\Gamma} = \beta\Gamma - \beta\Gamma N(t)y\Gamma, \tag{2.26}$$

where $\theta = \hat{\theta} + S(t)$. In the error variables $\tilde{\theta} = \hat{\theta} - \theta^*, \tilde{\Gamma} = \Gamma - H^{-1}$, when the map is quadratic, $Q(\theta) = Q^* + \frac{1}{2}(\theta - \theta^*)^T H(\theta - \theta^*)$, the averaged closed-loop system is given by

$$\dot{\tilde{\theta}} = -K\tilde{\theta} - K\tilde{\Gamma}H\tilde{\theta} \tag{2.27}$$

$$\dot{\tilde{\Gamma}} = -\beta\tilde{\Gamma} - \beta\tilde{\Gamma}H\tilde{\Gamma}, \tag{2.28}$$

where $K\tilde{\Gamma}H\tilde{\theta}$ is quadratic in $(\tilde{\Gamma},\tilde{\theta})$, and $\beta\tilde{\Gamma}H\tilde{\Gamma}$ is quadratic in $\tilde{\Gamma}$. The linearization of this system has all of its eigenvalues at $-K$ and $-\beta$. Hence, unlike the gradient algorithm, whose convergence is governed by the unknown Hessian H, the convergence rate of the Newton algorithm can be arbitrarily assigned by the designer with an appropriate choice of K and β.

2.4 Newton Algorithm for Dynamic Systems

Consider a general Multi-Input-Single-Output (MISO) nonlinear model

$$\dot{x} = f(x,u), \tag{2.29}$$

$$y = h(x), \tag{2.30}$$

where $x \in \mathbb{R}^m$ is the state, $u \in \mathbb{R}^n$ is the input, $y \in \mathbb{R}$ is the output, and $f : \mathbb{R}^m \times \mathbb{R}^n \to \mathbb{R}^m$ and $h : \mathbb{R}^m \to \mathbb{R}$ are smooth. Suppose that we know a smooth control law $u = \alpha(x,\theta)$ parametrized by a vector parameter $\theta \in \mathbb{R}^n$. The closed loop system $\dot{x} = f(x,\alpha(x,\theta))$ then has equilibria parametrized by θ. We make the following assumptions about the closed-loop system, as in [45].

Assumption 1 *There exists a smooth function* $l{:}\mathbb{R}^n{\to}\mathbb{R}^m$ *such that* $f(x,\alpha(x,\theta)) = 0$ *if and only if* $x = l(\theta)$.

Assumption 2 *For each* $\theta \in \mathbb{R}^n$*, the equilibrium* $x = l(\theta)$ *of the system* $\dot{x} = f(x,\alpha(x,\theta))$ *is locally exponentially stable uniformly in* θ.

Assumption 3 *There exists* $\theta^* \in \mathbb{R}^n$ *such that*

$$\frac{\partial}{\partial\theta}(h{\circ}l)(\theta^*){=}0, \tag{2.31}$$

$$\frac{\partial^2}{\partial\theta^2}(h{\circ}l)(\theta^*){=}H < 0, \qquad H = H^T. \tag{2.32}$$

Our objective is to develop a feedback mechanism which maximizes the steady-state value of y but without requiring the knowledge of either θ^* or the functions h and l. The gradient-based ES design that achieves this objective, suitably adapted from [45] to the multivariable case, is shown schematically in

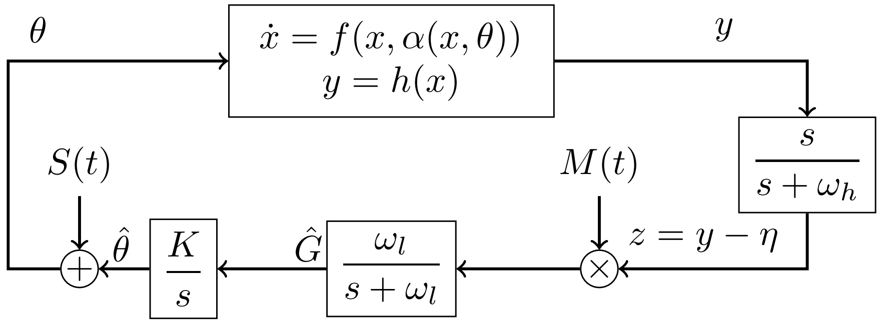

Figure 2.3: Gradient-based ES.

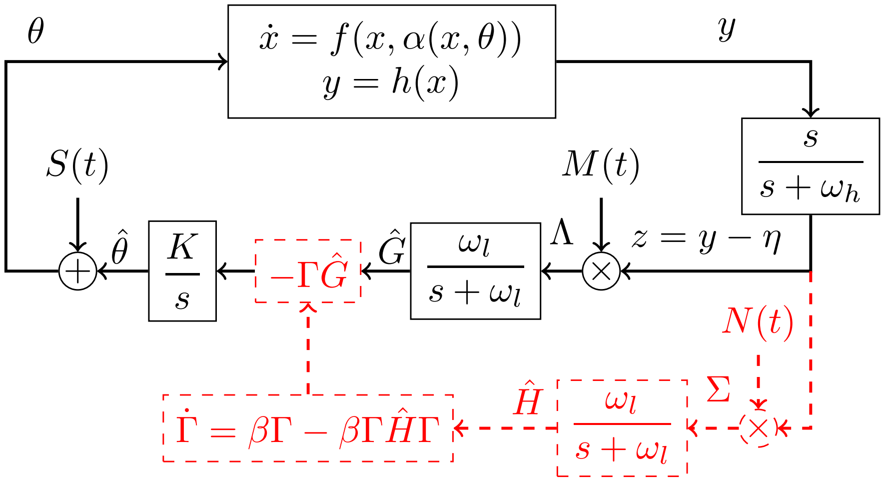

Figure 2.4: Newton-based ES. The initial condition $\Gamma(0)$ should be chosen negative definite and symmetric.

Fig. 2.3. Parallel to this, we present the generalized scheme for multivariable Newton-based ES as shown in Fig. 2.4.

The perturbation signals are defined by equations (2.2), (2.3), (2.20) and (2.21). The probing frequencies ω_i's, the filter coefficients ω_h, ω_l, and β and gain K are selected as

$$\omega_i = \epsilon\omega_i' = O(\epsilon), \qquad i \in \{1, 2, \cdots, n\} \tag{2.33}$$

$$\omega_h = \epsilon\omega_h' = \epsilon\delta\omega_h'' = O(\epsilon\delta) \tag{2.34}$$

$$\omega_l = \epsilon\omega_l' = \epsilon\delta\omega_l'' = O(\epsilon\delta) \tag{2.35}$$

$$\beta = \epsilon\beta' = \epsilon\delta\beta'' = O(\epsilon\delta) \tag{2.36}$$

$$K = \epsilon K' = \epsilon\delta K'' = O(\epsilon\delta), \tag{2.37}$$

where ϵ and δ are small positive constants, ω_i' is a rational number, ω_h'', ω_l'', and β'' are $O(1)$ positive constants, and K'' is a $n \times n$ diagonal matrix with $O(1)$ positive elements.

The analysis of [5, 45, 66] shows that, in the gradient-based scheme, for "sufficiently small" ϵ and $|a|$, where $a = [a_1\ a_2\ \cdots\ a_n]^T$, and sufficiently small δ, which imply small filter cut-off frequencies, the states $(x, \hat{\theta})$ of the closed-loop system exponentially converge to an $O(\epsilon + \delta + |a|)$-neighborhood of $(l(\theta^*), \theta^*)$, and the output y converges to an $O(\epsilon + \delta + |a|)$-neighborhood of the optimum output $y^* = (h \circ l)(\theta^*)$.

In Section 2.6 we prove that the average value of $\Sigma(t)$ over the period Π is close enough to the actual value of the Hessian, under specific conditions on ϵ, δ and a. Since we are integrating over a finite time period, and we set the phase delays of the periodic perturbation signals equal to zero, it is possible to exclude condition $\omega_i \neq \omega_j + \omega_k$. The probing frequencies need to satisfy

$$\omega_i' \notin \left\{\omega_j', \frac{1}{2}(\omega_j' + \omega_k'), \omega_j' + 2\omega_k', \omega_j' + \omega_k' \pm \omega_m'\right\}, \tag{2.38}$$

for all distinct i, j, k, and m. As we see in section 2.6, ignoring the conditions (2.38) is shifting the estimate of the parameter away from its true value, and leading to inaccurate estimates of the gradient vector and Hessian matrix.

2.5 Stability of the Closed-Loop System with the Newton-Based ES Algorithm

We summarize the system in Fig. 2.4 as

$$\frac{\mathrm{d}}{\mathrm{d}t}\begin{bmatrix} x \\ \tilde{\theta} \\ \hat{G} \\ \tilde{\Gamma} \\ \tilde{H} \\ \tilde{\eta} \end{bmatrix} = \begin{bmatrix} f(x, \alpha(x, \theta^* + \tilde{\theta} + S(t))) \\ -K(\tilde{\Gamma} + H^{-1})\hat{G} \\ -\omega_l \hat{G} + \omega_l \Big(y - h{\circ}l(\theta^*) - \tilde{\eta} \Big) M(t) \\ \beta(\tilde{\Gamma} + H^{-1}) \Big(I - (\tilde{H} + H)(\tilde{\Gamma} + H^{-1}) \Big) \\ -\omega_l \tilde{H} - \omega_l H + \omega_l \Big(y - h{\circ}l(\theta^*) - \tilde{\eta} \Big) N(t) \\ -\omega_h \tilde{\eta} + \omega_h \Big(y - h{\circ}l(\theta^*) \Big) \end{bmatrix}. \tag{2.39}$$

To conduct a stability analysis we have introduced error variables $\tilde{\theta} = \hat{\theta} - \theta^*$, $\theta = \hat{\theta} + S(t)$, $\tilde{\eta} = \eta - h{\circ}l(\theta^*)$, $\tilde{\Gamma} = \Gamma - H^{-1}$, and $\tilde{H} = \hat{H} - H$, where η is governed by $\dot{\eta} = -\omega_h \eta + \omega_h y$. We perform a slight abuse of notation by stacking matrix quantities $\tilde{\Gamma}$ and $\tilde{H}$ along with vector quantities, as alternative notational choices would be more cumbersome.

Our main stability result is stated in the following theorem.

Theorem 1 *Consider the feedback system (2.39) under Assumptions 1, 2 and 3. There exists* $\bar{\epsilon} > 0$ *and for any* $\epsilon \in (0, \bar{\epsilon})$ *there exist* $\bar{\delta}, \bar{a} > 0$ *such that for the given* ϵ *and any* $|a| \in (0, \bar{a})$ *and* $\delta \in (0, \bar{\delta})$ *there exists a neighborhood of the point* $(x, \hat{\theta}, \hat{G}, \Gamma, \hat{H}, \eta) = (l(\theta^*), \theta^*, 0, H^{-1}, H, h{\circ}l(\theta^*))$ *such that any solution of systems (2.39) from the neighborhood exponentially converges to an* $O(\epsilon + \delta + |a|)$*-neighborhood of that point. Furthermore,* $y(t)$ *converges to an* $O(\epsilon + \delta + |a|)$*-neighborhood of* $h{\circ}l(\theta^*)$*.*

To prepare for the proof of Theorem 1, which is given in Sections 2.6 and

2.7, we summarize the system (2.39) in the time scale $\tau = \epsilon t$ as

$$\epsilon \frac{\mathrm{d}x}{\mathrm{d}\tau} = f(x, \alpha(x, \theta^* + \tilde{\theta} + \bar{S}(\tau))) \tag{2.40}$$

$$\frac{\mathrm{d}}{\mathrm{d}\tau} \begin{bmatrix} \tilde{\theta} \\ \hat{G} \\ \tilde{\Gamma} \\ \tilde{H} \\ \tilde{\eta} \end{bmatrix} = \delta \begin{bmatrix} -K''(\tilde{\Gamma} + H^{-1})\hat{G} \\ -\omega_l''\hat{G} + \omega_l''\Big(y - h \circ l(\theta^*) - \tilde{\eta}\Big)\bar{M}(\tau) \\ \beta''(\tilde{\Gamma} + H^{-1})\Big(I - (\tilde{H} + H)(\tilde{\Gamma} + H^{-1})\Big) \\ -\omega_l''(\tilde{H} + H) + \omega_l''\Big(y - h \circ l(\theta^*) - \tilde{\eta}\Big)\bar{N}(\tau) \\ -\omega_h''\tilde{\eta} + \omega_h''\Big(y - h \circ l(\theta^*)\Big) \end{bmatrix}, \tag{2.41}$$

where $\bar{S}(\tau) = S(t/\epsilon)$, $\bar{M}(\tau) = M(t/\epsilon)$ and $\bar{N}(\tau) = N(t/\epsilon)$.

2.6 Averaging Analysis

The first step in our analysis is to study the system in Fig. 2.4. We "freeze" x in (2.40) at its equilibrium value $x = l(\theta^* + \tilde{\theta} + \bar{S}(\tau))$ and substitute it into (2.41), getting the reduced system

$$\frac{\mathrm{d}}{\mathrm{d}\tau} \begin{bmatrix} \tilde{\theta}_r \\ \hat{G}_r \\ \tilde{\Gamma}_r \\ \tilde{H}_r \\ \tilde{\eta}_r \end{bmatrix} = \delta \begin{bmatrix} -K''(\tilde{\Gamma}_r + H^{-1})\hat{G}_r \\ -\omega_l''\hat{G}_r + \omega_l''\Big(\nu(\tilde{\theta}_r + \bar{S}(\tau)) - \tilde{\eta}_r\Big)\bar{M}(\tau) \\ \beta''(\tilde{\Gamma}_r + H^{-1})\Big(I + (\tilde{H}_r + H)(\tilde{\Gamma}_r + H^{-1})\Big) \\ -\omega_l''\tilde{H}_r - \omega_l''H + \omega_l''\Big(\nu(\tilde{\theta}_r + \bar{S}(\tau)) - \tilde{\eta}_r\Big)\bar{N}(\tau) \\ -\omega_h''\tilde{\eta}_r + \omega_h''\nu(\tilde{\theta}_r + \bar{S}(\tau)) \end{bmatrix}, \tag{2.42}$$

where $\nu(z) = h \circ l(\theta^* + z) - h \circ l(\theta^*)$. In view of Assumption 3, $\nu(0) = 0$, $\partial\nu(0)/\partial z = 0$, and $\partial^2\nu(0)/\partial z^2 = H < 0$.

To prove the overall stability of (2.39), first we show that the reduced system (2.42) has a unique exponentially stable periodic solution around its equilibrium.

Theorem 2 *Consider system (2.42) under Assumption 3. There exist $\bar{\delta}, \bar{a} > 0$ such that for all $\delta \in (0, \bar{\delta})$ and $|a| \in (0, \bar{a})$ system (2.42) has a unique exponentially stable periodic solution $\Big(\tilde{\theta}_r^{\Pi}(\tau), \hat{G}_r^{\Pi}(\tau), \tilde{\Gamma}_r^{\Pi}(\tau), \tilde{H}_r^{\Pi}(\tau), \tilde{\eta}_r^{\Pi}(\tau)\Big)$ of period Π and this* *solution satisfies*

$$\left|\tilde{\theta}^{\Pi}_{r,i}(\tau) - \sum_{j=1}^{n} c^{i}_{j,j} a_j^2\right| \leq O(\delta + |a|^3) \tag{2.43}$$

$$\left|\hat{G}^{\Pi}_{r}(\tau)\right| \leq O(\delta) \tag{2.44}$$

$$\left|\tilde{\Gamma}^{\Pi}_{r}(\tau) + \sum_{i=1}^{n}\sum_{j=1}^{n} H^{-1} W^{i} H^{-1} c^{i}_{j,j} a_j^2\right| \leq O(\delta + |a|^3) \tag{2.45}$$

$$\left|\tilde{H}^{\Pi}_{r}(\tau) - \sum_{i=1}^{n}\sum_{j=1}^{n} W^{i} c^{i}_{j,j} a_j^2\right| \leq O(\delta + |a|^3) \tag{2.46}$$

$$\left|\tilde{\eta}^{\Pi}_{r}(\tau) - \frac{1}{4}\sum_{i=1}^{n} H_{i,i} a_i^2\right| \leq O(\delta + |a|^4) \tag{2.47}$$

for all $\tau \geq 0$*, where*

$$\begin{bmatrix} c^{1}_{j,j} \\ \vdots \\ c^{i-1}_{j,j} \\ \\ c^{i}_{j,j} \\ \\ c^{i+1}_{j,j} \\ \vdots \\ c^{n}_{j,j} \end{bmatrix} = -\frac{1}{12} H^{-1} \begin{bmatrix} \frac{\partial^3 \nu}{\partial z_j \partial z_1^2}(0) \\ \vdots \\ \frac{\partial^3 \nu}{\partial z_j \partial z_{j-1}^2}(0) \\ \\ \frac{3}{2}\frac{\partial^3 \nu}{\partial z_j^3}(0) \\ \\ \frac{\partial^3 \nu}{\partial z_j \partial z_{j+1}^2}(0) \\ \vdots \\ \frac{\partial^3 \nu}{\partial z_j \partial z_n^2}(0) \end{bmatrix}, \forall i, j \in \{1, 2, \cdots, n\} \tag{2.48}$$

$$\left(W^{i}\right)_{j,k} = \frac{\partial^3 \nu(0)}{\partial z_i \partial z_j \partial z_k}, \quad \forall i, j, \text{and } k \in \{1, 2, \cdots, n\}. \tag{2.49}$$

System (2.42) is in the form to which the averaging method is applicable. The average model of (2.42) is

$$\frac{\mathrm{d}}{\mathrm{d}\tau}\begin{bmatrix} \tilde{\theta}^{aT}_{r} & \hat{G}^{aT}_{r} & \tilde{\Gamma}^{aT}_{r} & \tilde{H}^{aT}_{r} & \tilde{\eta}^{a}_{r} \end{bmatrix}^{T} =$$
$$\delta \begin{bmatrix} -K''(\tilde{\Gamma}^{a}_{r} + H^{-1})\hat{G}^{a}_{r} \\ -\omega''_{l}\hat{G}^{a}_{r} + \omega''_{l}\frac{1}{\Pi}\int_0^{\Pi} \nu(\tilde{\theta}^{a}_{r} + \bar{S}(\sigma))\bar{M}(\sigma)\mathrm{d}\sigma \\ \beta''(\tilde{\Gamma}^{a}_{r} + H^{-1})\Big(I - (\tilde{H}^{a}_{r} + H)(\tilde{\Gamma}^{a}_{r} + H^{-1})\Big) \\ -\omega''_{l}\tilde{H}^{a}_{r} - \omega''_{l}H + \omega''_{l}\frac{1}{\Pi}\int_0^{\Pi} \nu(\tilde{\theta}^{a}_{r} + \bar{S}(\sigma))\bar{N}(\sigma)\mathrm{d}\sigma \\ -\omega''_{h}\tilde{\eta}^{a}_{r} + \omega''_{h}\frac{1}{\Pi}\int_0^{\Pi} \nu(\tilde{\theta}^{a}_{r} + \bar{S}(\sigma))\mathrm{d}\sigma \end{bmatrix}. \tag{2.50}$$

Average equilibrium $\left(\tilde{\theta}_r^{a,e}, \hat{G}_r^{a,e}, \tilde{\Gamma}_r^{a,e}, \tilde{H}_r^{a,e}, \tilde{\eta}_r^{a,e}\right)$ satisfies

$$\hat{G}_r^{a,e} = 0 \tag{2.51}$$

$$\int_0^{\Pi} \nu(\tilde{\theta}_r^{a,e} + \bar{S}(\sigma))\bar{M}(\sigma)\mathrm{d}\sigma = 0 \tag{2.52}$$

$$\tilde{\eta}_r^{a,e} = \frac{1}{\Pi}\int_0^{\Pi} \nu(\tilde{\theta}_r^{a,e} + \bar{S}(\sigma))\mathrm{d}\sigma \tag{2.53}$$

$$\tilde{H}_r^{a,e} + H = \frac{1}{\Pi}\int_0^{\Pi} \nu(\tilde{\theta}_r^{a,e} + \bar{S}(\sigma))\bar{N}(\sigma)\mathrm{d}\sigma \tag{2.54}$$

$$(\tilde{H}_r^{a,e} + H)(\tilde{\Gamma}_r^{a,e} + H^{-1}) = I. \tag{2.55}$$

As we shall see, for small $|a|$, $\tilde{\Gamma}_r^{a,e}+H^{-1}<0$. By postulating $\tilde{\theta}_{r,i}^{a,e}$ in the form

$$\tilde{\theta}_{r,i}^{a,e} = \sum_{j=1}^{n} b_j^i a_j + \sum_{j=1}^{n}\sum_{k=1}^{n} c_{j,k}^i a_j a_k + O(|a|^3), \tag{2.56}$$

where b_j^i and $c_{j,k}^i$ are real numbers, substituting (2.56) in (2.51)-(2.55) and equating the like powers of a_j, we get $b_j^i = 0$, for all $i, j \in \{1, 2, \cdots, n\}$, $c_{j,k}^i = 0$, for all $i, j{\neq}k \in \{1, 2, \cdots, n\}$, and (2.48). The equilibrium of the average system is:

$$\begin{aligned}
\tilde{\theta}_{r,i}^{a,e} &= \sum_{j=1}^{n} c_{j,j}^i a_j^2 + O(|a|^3) \\
\hat{G}_r^{a,e} &= 0_{n\times 1} \\
\tilde{\Gamma}_r^{a,e} &= -\sum_{i=1}^{n}\sum_{j=1}^{n} H^{-1}W^i H^{-1} c_{j,j}^i a_j^2 + \left[O(|a|^3)\right]_{n\times n} \\
\tilde{H}_r^{a,e} &= \sum_{i=1}^{n}\sum_{j=1}^{n} W^i c_{j,j}^i a_j^2 + \left[O(|a|^3)\right]_{n\times n} \\
\tilde{\eta}_r^{a,e} &= \frac{1}{4}\sum_{i=1}^{n} H_{i,i} a_i^2 + O(|a|^4),
\end{aligned} \tag{2.57}$$

where W^i is a $n\times n$ matrix defined by (2.49). The Jacobian of the average system at the equilibrium is

$$\begin{aligned}
J_r^{a,e} &= \delta \begin{bmatrix} A_{2n\times 2n} & 0_{2n\times(2n+1)} \\ B_{(2n+1)\times 2n} & C_{(2n+1)\times(2n+1)} \end{bmatrix}, \qquad (2.58)\\
A &= \begin{bmatrix} 0_{n\times n} & -K''\Big(H^{-1}+\tilde{\Gamma}_r^{a,e}\Big) \\ \frac{\omega_l''}{\Pi}\int_0^\Pi \frac{\partial}{\partial\tilde{\theta}}(\nu\bar{M})\mathrm{d}\sigma & -\omega_l'' I_{n\times n} \end{bmatrix},\\
B &= \begin{bmatrix} 0_{n\times n} & 0_{n\times n} \\ \omega_l''\frac{1}{\Pi}\int_0^\Pi \frac{\partial}{\partial\tilde{\theta}}(\nu\bar{N})\mathrm{d}\sigma & 0_{n\times n} \\ \omega_h''\frac{1}{\Pi}\int_0^\Pi \frac{\partial}{\partial\tilde{\theta}}(\nu)\mathrm{d}\sigma & 0_{1\times n} \end{bmatrix},\\
C &= \begin{bmatrix} -\beta'' I_{n\times n}+\mathcal{O}_1 & -\beta'' H^{-2}+\mathcal{O}_2 & 0_{n\times 1} \\ 0_{n\times n} & -\omega_l'' I_{n\times n} & 0_{n\times 1} \\ 0_{1\times n} & 0_{1\times n} & -\omega_h'' \end{bmatrix},\\
\mathcal{O}_1 &= \beta''\sum_{i=1}^{n}\sum_{j=1}^{n} H^{-1}W^i c_{j,j}^i a_j^2 + \left[O(|a|^3)\right],\\
\mathcal{O}_2 &= \beta''\sum_{i=1}^{n}\sum_{j=1}^{n} H^{-1}\Big(W^i H^{-1} - H^{-1}W^i\Big)H^{-1}c_{j,j}^i a_j^2 + \\
&\quad + \left[O(|a|^3)\right].
\end{aligned}$$

Since $J_r^{a,e}$ is block-lower-triangular, it is Hurwitz if and only if

$$A_{21} := \frac{\omega_l''}{\Pi}\int_0^\Pi \bar{M}(\sigma)\frac{\partial}{\partial\tilde{\theta}}\nu(\tilde{\theta}_r^{a,e}+\bar{S}(\sigma))\mathrm{d}\sigma < 0. \tag{2.59}$$

With a Taylor expansion we get that $A_{21} = \omega_l'' H + O(|a|)$. We then have

$$\begin{aligned}
&\det(\lambda I_{2n\times 2n} - \delta A) = \\
&= \det\Big(\lambda(\lambda+\omega_l''\delta)I_{n\times n} + \delta^2 K''(H^{-1}+\tilde{\Gamma}_r^{a,e})A_{21})\Big)\\
&= \det\Big((\lambda^2+\omega_l''\delta\lambda)I_{n\times n} + \\
&+\delta^2 K''(H^{-1}+[O(|a|^2)])(\omega_l'' H + [O(|a|)])\Big)\\
&= \det\big((\lambda^2+\omega_l''\delta\lambda)I_{n\times n}+\omega_l''\delta^2 K''+[O(\delta^2\,|a|)]_{n\times n}\big),
\end{aligned} \tag{2.60}$$

which, in view of $H<0$, proves that $J_r^{a,e}$ is Hurwitz for a that is sufficiently small in norm. This implies that the equilibrium (2.57) of the average system (2.50) is exponentially stable if all elements of vector a are sufficiently small. Then, according to the averaging theorem [40], the proof is completed.

2.7 Singular Perturbation Analysis

Now, we address the full system in Fig. 2.4 whose state space model is given by (2.40) and (2.41) in the time scale $\tau = \epsilon\, t$. To make the notation in our further analysis compact, we write (2.41) as

$$\frac{\mathrm{d}\xi}{\mathrm{d}\tau} = \delta E(\tau, x, \xi), \tag{2.61}$$

where $\xi = (\tilde{\theta}, \hat{G}, \tilde{\Gamma}, \tilde{H}, \tilde{\eta})$. By Theorem 2, there exists an exponentially stable periodic solution $\xi_r^{\Pi}(\tau)$ such that

$$\frac{\mathrm{d}\xi_r^{\Pi}(\tau)}{\mathrm{d}\tau} = \delta E(\tau, L(\tau, \xi_r^{\Pi}(\tau)), \xi_r^{\Pi}(\tau)), \tag{2.62}$$

where $L(\tau, \xi) = l(\theta^* + \tilde{\theta} + \bar{S}(\tau))$. To bring the system (2.40) and (2.61) into the standard singular perturbation form,we shift the state ξ using the transformation $\tilde{\xi} = \xi - \xi_r^{\Pi}(\tau)$ and get

$$\frac{\mathrm{d}\tilde{\xi}}{\mathrm{d}\tau} = \delta \tilde{E}(\tau, x, \tilde{\xi}) \tag{2.63}$$

$$\epsilon \frac{\mathrm{d}x}{\mathrm{d}\tau} = \tilde{F}(\tau, x, \tilde{\xi}) \tag{2.64}$$

where

$$\tilde{E}(\tau, x, \tilde{\xi}) = E(\tau, x, \tilde{\xi} + \xi_r^{\Pi}(\tau)) - E(\tau, L(\tau, \xi_r^{\Pi}(\tau)), \xi_r^{\Pi}(\tau)) \tag{2.65}$$

$$\tilde{F}(\tau, x, \tilde{\xi}) = f\Big(x, \alpha\big(x, \tilde{\xi}_1 + \theta^* + \tilde{\theta}_r^{\Pi}(\tau) + \bar{S}(\tau)\big)\Big). \tag{2.66}$$

We note that $x = L(\tau, \tilde{\xi}_r + \xi_r^{\Pi}(\tau))$ is the quasi-steady state, and that the reduced model

$$\frac{\mathrm{d}\tilde{\xi}_r}{\mathrm{d}\tau} = \delta \tilde{E}\Big(\tau, L\big(\tau, \tilde{\xi}_r + \xi_r^{\Pi}(\tau)\big), \tilde{\xi}_r + \xi_r^{\Pi}(\tau)\Big) \tag{2.67}$$

has an equilibrium at the origin $\tilde{\xi}_r = 0$. This equilibrium has been shown in Section 2.6 to be exponentially stable for a small $|a|$.

To complete the singular perturbation analysis, we also study the boundary layer model (in the time scale $t-t_0=\tau/\epsilon$):

$$\begin{aligned}\frac{\mathrm{d}x_\mathrm{b}}{\mathrm{d}t} &= \tilde{F}(\tau, x_\mathrm{b} + L(\tau, \tilde{\xi} + \xi_r^\Pi(\tau)), \tilde{\xi}), \\ &= f(x_\mathrm{b} + l(\theta), \alpha(x_\mathrm{b} + l(\theta), \theta)), \end{aligned} \tag{2.68}$$

where $\theta = \theta^* + \tilde{\theta} + \bar{S}(\tau)$ should be viewed as a parameter independent from the time variable t. Since $f(l(\theta), \alpha(l(\theta), \theta)) \equiv 0$, then $x_\mathrm{b} \equiv 0$ is an equilibrium of (2.68). By Assumption 2, this equilibrium is locally exponentially stable uniformly in θ (and hence $l(\theta)$).

By combining exponential stability of the reduced model (2.67) with the exponential stability of the boundary layer model (2.68), using Tikhonov's Theorem on the Infinite Interval (Theorem 9.4 in [40]), we conclude the following:

a) The solution $\xi(\tau)$ of (2.61) is $O(\epsilon)$-close to the solution $\xi_r(\tau)$ of (2.67), and therefore, it exponentially converges to an $O(\epsilon)$-neighborhood of the periodic solution $\xi_r^\Pi(\tau)$, which is $O(\delta)$-close to the equilibrium $\xi_r^{a,e}$. This, in turn, implies that the solution $\tilde{\theta}(\tau)$ of (2.41) exponentially converges to an $O(\epsilon+\delta)$-neighborhood of

$$\sum_{j=1}^{n} \begin{bmatrix} c_{j,j}^1 & c_{j,j}^2 & \cdots & c_{j,j}^n \end{bmatrix}^T a_j^2 + [O(|a|^3)]_{n\times 1}. \tag{2.69}$$

It follows then that $\theta(\tau) = \theta^* + \tilde{\theta}(\tau) + \bar{S}(\tau)$ exponentially converges to an $O(\epsilon + \delta + |a|)$-neighborhood of θ^*.

b) The solution $x(\tau)$ of (2.64) satisfies

$$x(\tau) - l(\theta^* + \tilde{\theta}_r(\tau) + \bar{S}(\tau)) - x_\mathrm{b}(t) = O(\epsilon), \tag{2.70}$$

where $\tilde{\theta}_r(\tau)$ is the solution of the reduced model (2.42) and $x_\mathrm{b}(t)$ is the solution of the boundary layer model (2.68). From (2.70) we get

$$x(\tau) - l(\theta^*) = O(\epsilon) + l(\theta^* + \tilde{\theta}_r(\tau) + \bar{S}(t)) - l(\theta^*) + x_\mathrm{b}(t). \tag{2.71}$$

Since $\tilde{\theta}_r(\tau)$ exponentially converges to the periodic solution $\tilde{\theta}_r^\Pi(\tau)$, which is $O(\delta)$-close to the average equilibrium (2.69), and since the solution $x_\mathrm{b}(t)$ of (2.68) is exponentially decaying, then by (2.71), $x(\tau) - l(\theta^*)$ exponentially converges to an

$O(\epsilon+\delta+|a|)$-neighborhood of zero. Consequently, $y = h(x)$ exponentially converges to an $O(\epsilon + \delta + |a|)$-neighborhood of its maximal equilibrium value $h \circ l(\theta^*)$.

This completes the proof of Theorem 1.

2.8 Simulation Results

To illustrate the results and highlight the difference between the gradient-based and Newton-based ES methods, the following static quadratic input-output map is considered:

$$y = Q(\theta) = Q^* + \frac{1}{2}(\theta - \theta^*)^T H(\theta - \theta^*). \tag{2.72}$$

To make a fair comparison between the two methods, all parameters are chosen the same except the gain matrix. Before selecting matrix K we investigate the performance of the gradient-based scheme versus the Newton-based scheme.

Recall (2.27) and (2.28). The initial convergence rate for the Newton-based scheme is governed by the time-varying matrix $-K_n\Gamma(t)H$. Equation (2.4) shows that in the gradient-based scheme the convergence depends on the eigenvalues of K_gH. This means that, to have a fair comparison between the two methods, we should select K_g and K_n such that $K_g = -K_n\Gamma(0)$.

We perform our tests with the following parameters, $\delta = 0.1$, $\epsilon = 0.1$, $\omega_1' = 70\,\mathrm{rad/s}$, $\omega_2' = 50\,\mathrm{rad/s}$, $\omega_l'' = 10\,\mathrm{rad/s}$, $\omega_h'' = 8\,\mathrm{rad/s}$, $\beta'' = 10$, $a = [0.1\ \ 0.1]^T$, $K_g'' = 10^{-4}\mathrm{diag}([25\ 25])$, $K_n'' = \mathrm{diag}([1\ 1])$, $\Gamma_0^{-1} = -400\mathrm{diag}([1\ 1])$, $\hat{\theta}_0 = [2.5\ \ 5]^T$, $Q^* = 100$, $\theta^* = [2\ \ 4]^T$, $H_{11} = -100$, $H_{12} = H_{21} = -30$, and $H_{22} = -20$.

Fig. 2.5 illustrates the estimate of the maximum. Evolution of the parameters is depicted in Fig. 2.6. Since the initial estimate of the Hessian is not true, each parameter starts to update with a different rate. As seen in Fig. 2.7, after 40 seconds the estimate of the Hessian is close enough to its actual value. Hence, the convergence rates of both parameters are the same after 40 seconds. Furthermore, Fig. 2.6(c) shows that, except for a short initial transient that is due to the estimation of the inverse of the Hessian, the Newton-based ES moves the parameters to the peak along a straight trajectory. In contrast, the trajectory of the gradient-based algorithm is curved and of greater length. Figs. 2.6(a) and

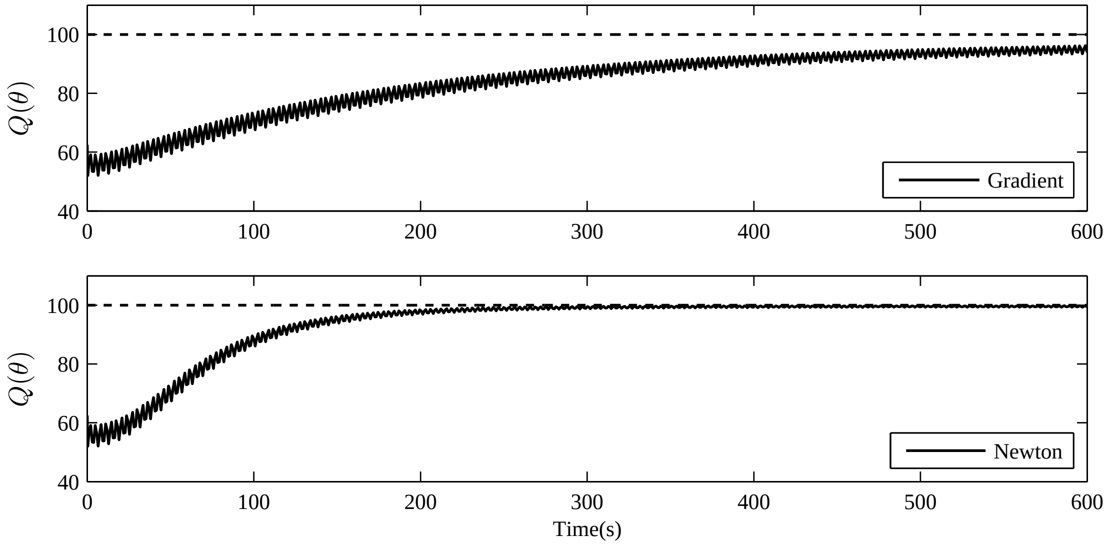

Figure 2.5: The estimate of the maximum versus time.

2.6(c) show that the gradient algorithm, which follows the steepest-descent path, results in the parameter $\hat{\theta}_1$ undershooting below its true value, which is not the case with the Newton algorithm whose parameter transients are monotonic. The Hessian matrix converges to its actual value as depicted in Fig. 2.7. Also it is worth noting that the Hessian converges faster to its actual value than $\hat{G}$ and $\hat{\theta}$. As illustrated in Fig. 2.8 the estimate of the gradient vector converges to zero after Hessian matrix finds its true value.

2.9 Conclusions

Using the gradient-based ES in the multivariable case without having a good information about the curvature of the cost function, namely, the Hessian matrix, may result inappropriate performance. With a growing number of the parameters, it is almost impossible to tune the convergence rate of all parameters in a desirable fashion. The Newton-based ES, which relies on the estimation of the gradient and Hessian matrix of the cost function at the same time, removes the trial and error process to update all parameters uniformly. Furthermore, the proposed Newton scheme eliminates the concern about the inversion of the Hessian estimate

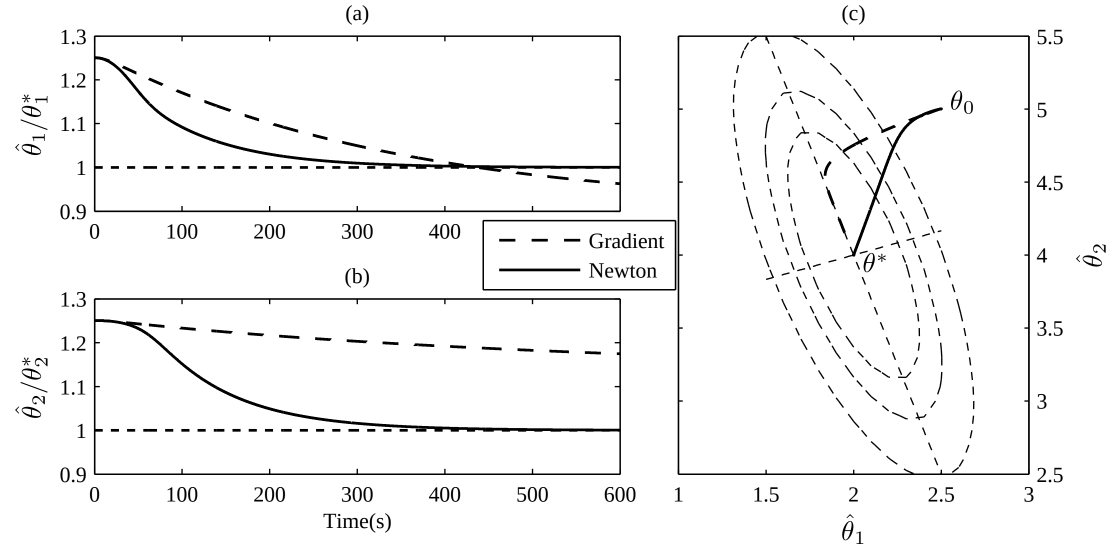

Figure 2.6: Parameter estimates. (a and b) time responses. (c) phase portrait. The Newton trajectory is straight to the extremum, whereas the gradient trajectory follows the curved, steepest-descent path.

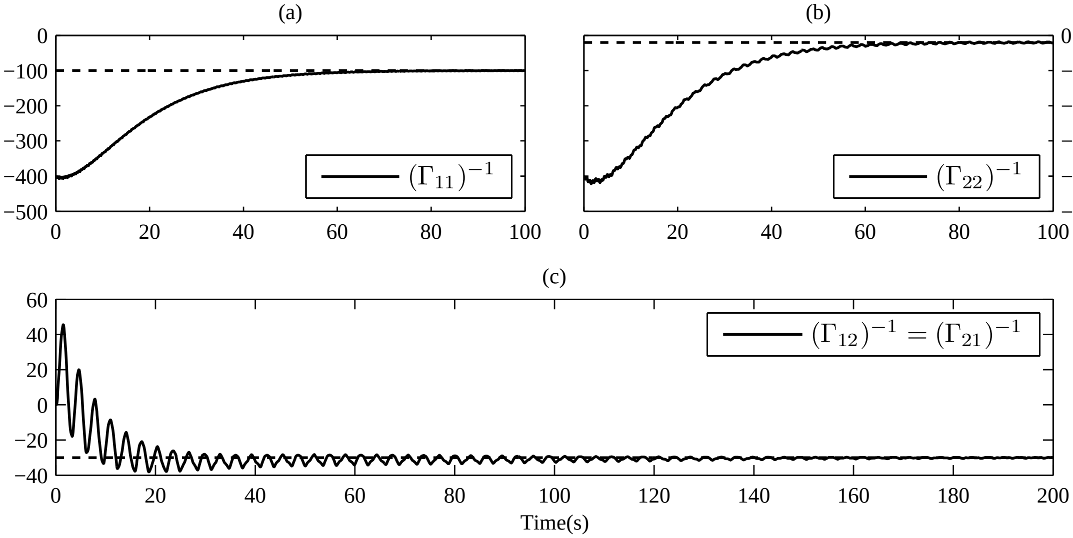

Figure 2.7: Time evolution of the Hessian matrix estimator Γ^{-1}. The true value of H is reached in 40 seconds. Note in Fig. 2.6 that the Newton and gradient trajectories coincide for the first 40 seconds, after which, Newton takes a straight path.

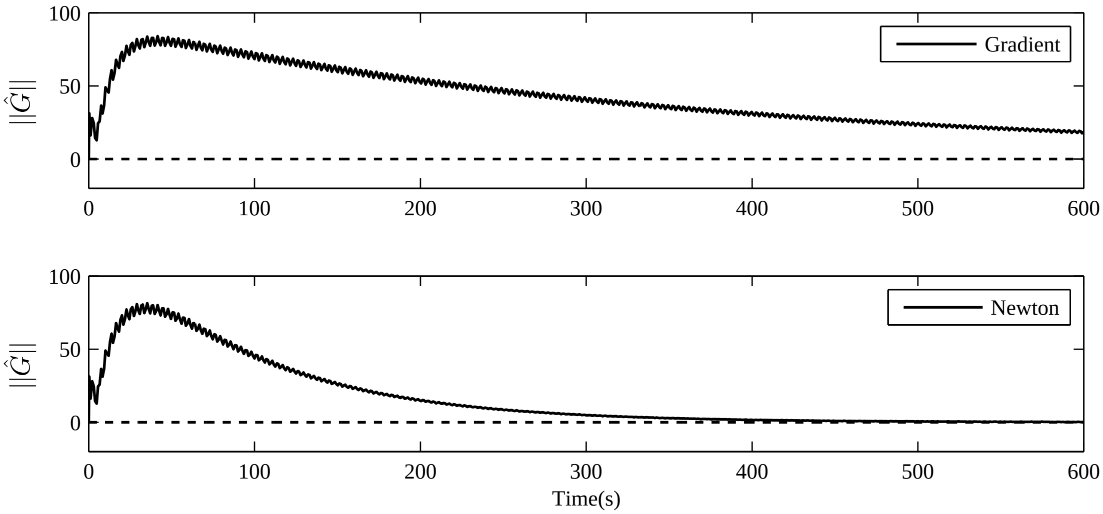

Figure 2.8: The estimate of the gradient vector versus time.

matrix by performing the inversion dynamically using a Riccati equation filter. The convergence rates of both the parameter and of the estimator of the Hessian inverse are independent of the unknown Hessian and can be assigned arbitrary by the user.

This chapter contains material from Aazad Ghaffari, Miroslav Krstić, and Dragan Nesić,"Multivariable Newton-Based Extremum Seeking," *Automatica*, vol. 48, pp. 1759-1767, 2012. Of which the dissertation author was the primary author.

Chapter 3

Photovoltaic Modules and Power Extraction

In order to perform simulations to verify the analytical results of our proposed Newton-based ES algorithm for power optimization of a Photovoltaic (PV) system, we need an accurate mode for the PV module and a reliable method to design the DC/DC converters. The converters are assumed to work in Continuous Conduction Mode (CCM) and the DC bus voltage is held constant with an appropriate controller which is out of the scope of this work.

3.1 Introduction

Photovoltaic (PV) modules show variable peak power under different solar irradiance and environmental temperature. Also module degradation and partial shading have dramatic effect on the generated power by a specific PV module. Furthermore, Manufacturers install bypass diodes to protect PV modules from over current conditions which create multiple maxima for the power curve of a PV module. While several papers have discussed PV models, for example, [18, 62, 68, 74], we believe the modeling results that we present (a) are comprehensive in that they present all the information required to build and simulate PV modules based on manufacturer datasheet information, and (b) allow for simulation of non-unimodal power characteristics, i.e., multiple local maxima in the power-voltage curve as a result of partial shading.

In the literature different topologies of DC/DC converters and DC/AC inverters have been employed to harvest power from PV modules for various target applications. We assume that we have access to a DC bus with controlled voltage with an acceptable percentage ripple which allows us to select DC/DC converter as our main power stage instrument to extract power form PV modules. In this Chapter we provide guidelines for the selection of the power electronics components (in our review of the literature, we found that this was not done at all, or at best glossed over, with the reader referred to textbooks such as [24, 38], and/or technical reports such as [64, 65]).

While power electronics models have normally been simulated using SPICE, since we are planning to develop our control and optimization algorithms using MATLAB, we use SimPowerSystems™ as the development platform, which is an add-on that extends MATLAB and Simulink® with tools for modeling and simulating power electronics/systems, and is hence ideally suited to seamlessly modeling and simulating control and power electronics interaction and performance.

The rest of this chapter is organized as follows: first we present equivalent electrical circuit of a PV module and its relevant mathematical equations in Section 3.2, then PV module modeling, along with the estimation of module parameters based on technical data presented in datasheet information, is discussed in detail in Section 3.3. in Section 3.4, we present detailed guidelines for the selection of the power-MOSFET and the other DC/DC converter parameters. This is done for the both buck as well as boost converters, with a tabulation of all the associated losses. Our results can be extended to other DC/DC stages such as the Ćuk and SEPIC converters. The concluding remarks is presented in Section3.5.

3.2 PV Module Equivalent Circuit

Our design and analysis are based on the standard PV module model described for example in [74], and shown schematically in Fig. 3.1. Each PV cell is modeled as an ideal current source of value I_{ph} in parallel with an ideal diode

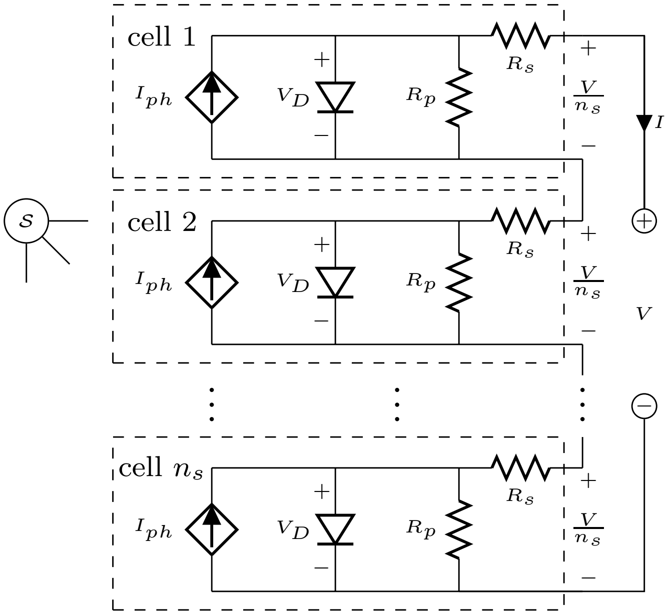

Figure 3.1: Equivalent circuit of a PV module.

with voltage V_D. Electrical losses and contactor resistance are accounted for by the inclusion of the parallel and series resistances R_s and R_p respectively. The amount of generated current I_{ph} is dependent on the solar irradiance $\mathcal{S}$ and the temperature $\mathcal{T}$ through the following equation

$$I_{ph} = \left(I_{ph}^r + k_i(\mathcal{T} - \mathcal{T}_r)\right)\left(\frac{\mathcal{S}}{1000}\right), \tag{3.1}$$

where I_{ph}^r is a reference short-circuit current, $\mathcal{T}_r$ a reference temperature, and k_i the short-circuit temperature coefficient. The diode models the effect of the semiconductor material and its I-V characteristics are given by

$$I_D = I_0\left(\exp\left(\frac{V_D}{\mathcal{N}V_t}\right) - 1\right), \tag{3.2}$$

$$I_0 = I_0^r\left(\frac{\mathcal{T}}{\mathcal{T}_r}\right)^3 \exp\left[\frac{E_g}{\mathcal{N}V_t}\left(\frac{\mathcal{T}}{\mathcal{T}_r} - 1\right)\right], V_t = \left(\frac{k\mathcal{T}}{q}\right) \tag{3.3}$$

where n_s, I_0^r, E_g and $\mathcal{N}$ are respectively the number of series PV cells in the module, the diode reference reverse saturation current, the semiconductor bandgap voltage (barrier height), and the emission coefficient, all three being cell material/construction dependent, V_t is the thermal cell voltage, and $k = 1.38 \times 10^{-23}$ J/K and $q = 1.6 \times 10^{-19}$ C are Boltzman's constant and the charge on an

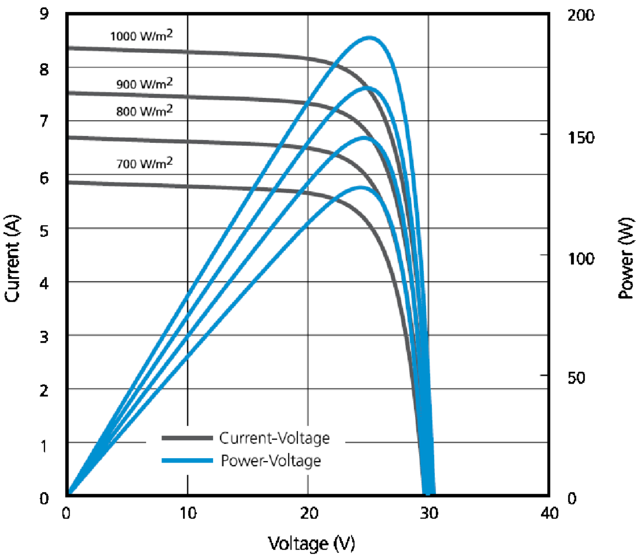

Figure 3.2: Current (black) and power (blue) characteristics for PV module UD6 from Mitsubishi Electric.

electron respectively. The PV model described by the above equations along with KCL/KVL: $I = I_{ph} - I_D - V_D/R_p$, $V_D = V/n_s + R_s I$, represent a PV module by considering n_s cells in series (each having thermal voltage V_t), so that the terminal I-V relationship for the PV module is given by

$$I = I_{ph} – I_0 \left[\exp\left(\frac{\frac{V}{n_s} + R_s I}{\mathcal{N} V_t} \right) - 1 \right] – \left[\frac{(\frac{V}{n_s} + R_s I)}{R_p} \right]. \tag{3.4}$$

3.3 PV Model Based on Manufacturer Data

Sample P-V and I-V characteristics for PV module model UD6 from Mitsubishi Electric with maximum power 190 W are shown in Fig. 3.2. Simulation of a PV cell/module requires numerical values for I_0^r, I_{ph}^r, $\mathcal{N}$, E_g, R_s, and R_p. PV manufacturers do not provide these parameters, instead they provide other technical data measured under “Standard Test Conditions” (STC), namely $\mathcal{S} = 1000 W/m^2$, $\mathcal{T} = 25°\text{C}$, that includes Maximum Power Point (MPP) voltage V^*, MPP current I^*, open circuit voltage V_{oc}, short circuit current I_{sc}, temperature coefficient for MPP k_p, temperature coefficient for open circuit voltage k_v, temperature coefficient for short circuit current k_i, number of PV cells n_s. The relationship between a PV cell and PV module current and voltage is simply $I_c = I$, and $V_c = V/n_s$ where subscript c shows the PV cell parameter.

We briefly describe how to obtain the required numerical values for simulation from manufacturer provided data. Short-circuit quantities I_{sc} and $V_{sc} = 0$, and open-circuit quantities $I_{oc} = 0$ and V_{oc} are related as

$$\begin{aligned} I_{ph} &= \frac{RI_{sc}}{R_p} \qquad (3.5) \\ I_0 &= \left(\frac{RI_{sc} - \frac{V_{oc}}{n_s}}{R_p}\right) \exp\left(-\frac{V_{oc}}{n_s \mathcal{N} V_t^r}\right), \qquad (3.6) \end{aligned}$$

where $R := R_p + R_s$, $V_t^r := k\mathcal{T}_r/q$, and $\mathcal{T}_r = 298.15$ K is the module junction temperature under STC. Replacing I^* and V^* in (3.4), and using (3.5) and (3.6) results in

$$(RI_{sc} - \frac{V_{oc}}{n_s})\exp\left(\frac{\frac{V^*}{n_s} - \frac{V_{oc}}{n_s} + R_s I^*}{\mathcal{N} V_t^r}\right) + R(I^* - I_{sc}) + \frac{V^*}{n_s} = 0. \qquad (3.7)$$

Making use of the fact that a PV module has a unique maximum point (V^*, P^*) for its P-V characteristic, at which

$$\left.\frac{\mathrm{d}P}{\mathrm{d}V}\right|_{\substack{V=V^* \\ I=I^*}} = I^* + \left.\frac{\mathrm{d}I}{\mathrm{d}V}\right|_{\substack{V=V^* \\ I=I^*}} V^* = 0, \qquad (3.8)$$

along with $I = \mathcal{F}(I, V)$ so that

$$\mathrm{d}\mathcal{F}(I, V) = \frac{\partial \mathcal{F}(I, V)}{\partial I}\mathrm{d}I + \frac{\partial \mathcal{F}(I, V)}{\partial V}\mathrm{d}V, \qquad (3.9)$$

and substituting in (3.8) and simplifying, leads to

$$(R_s I^* - \frac{V^*}{n_s})(RI_{sc} - \frac{V_{oc}}{n_s})\exp\Big(\frac{V^* - V_{oc} R_s I^*}{n_s \mathcal{N} V_t^r}\Big) + (RI^* - \frac{V^*}{ns})\mathcal{N} V_t^r = 0. \qquad (3.10)$$

The short-circuit I-V relationship can be shown (see [18] for example) to be

$$\left.\frac{\mathrm{d}I}{\mathrm{d}V}\right|_{\substack{V=0 \\ I=I_{sc}}} = -\frac{1}{n_s R_p}. \qquad (3.11)$$

Using this, along with (3.9), and more steps of simplification results in

$$\mathcal{N} V_t^r R_s + (R_s - R_p)(RI_{sc} - \frac{V_{oc}}{n_s})\exp\Big(\frac{R_s I_{sc} - \frac{V_{oc}}{n_s}}{\mathcal{N} V_t^r}\Big) = 0. \qquad (3.12)$$

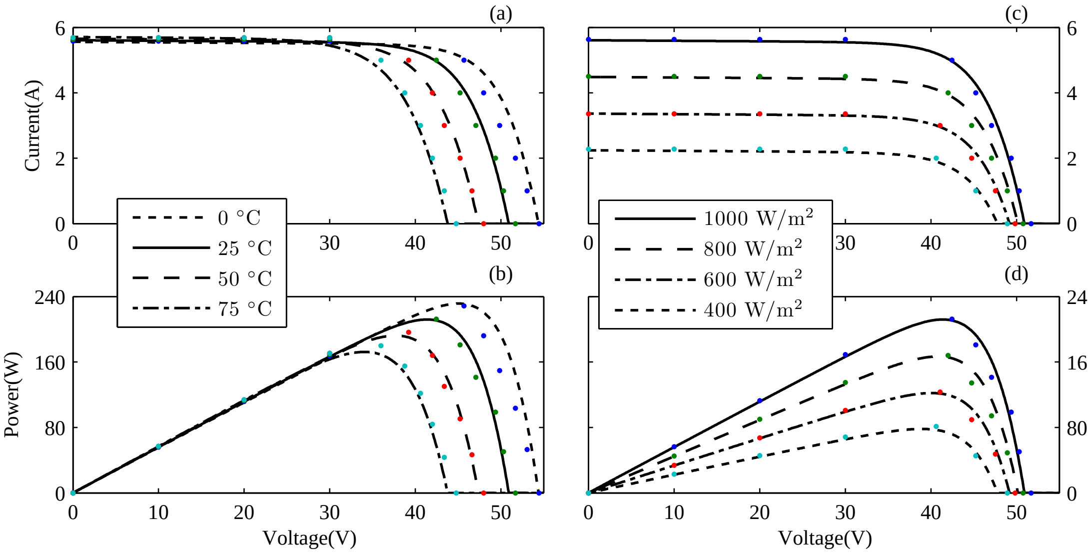

Figure 3.3: Sanyo PV module 215N model verification.

It is possible to solve (3.7), (3.10), and (3.12) using a numerical approach like Newton-Raphson to obtain the values of R_s, R_p, and $\mathcal{N}$. The procedure is described in other references (see, for example, [14]), and we use the same method here.

It is well known that the variation of short-circuit current with respect to temperature and irradiance follows

$$I_{sc}(\mathcal{T},\mathcal{S}) = (I^r_{sc} + k_i(\mathcal{T}-\mathcal{T}_r))\,\frac{\mathcal{S}}{\mathcal{S}_r}, \tag{3.13}$$

while the variation of the open-circuit voltage with respect to irradiance can be neglected, and its temperature dependence given by

$$V_{oc}(\mathcal{T}) = V_{oc} + k_v(\mathcal{T}-\mathcal{T}_r). \tag{3.14}$$

Using (3.5), (3.6), (3.13), and (3.14), we get

$$I_{ph}(\mathcal{T},\mathcal{S}) = \frac{R}{R_p} I_{sc}(\mathcal{T},\mathcal{S}) \tag{3.15}$$

$$I_0(\mathcal{T},\mathcal{S}) = \Big(I_{ph}(\mathcal{T},\mathcal{S}) - \frac{V_{oc}(\mathcal{T})}{n_s R_p}\Big)\exp\Big(-\frac{V_{oc}(\mathcal{T})}{n_s \mathcal{N} V^r_t}\Big) \tag{3.16}$$

which along with (3.3) can be used to compute E_g.

The modeling for a PV module can be extended to PV strings, where a cascade collection of cells within the module are supported by a bypass diode. Assume each PV string has n_a cells, then (3.4) with $n_s = n_a$ describes the relationship between voltage and current for each string.

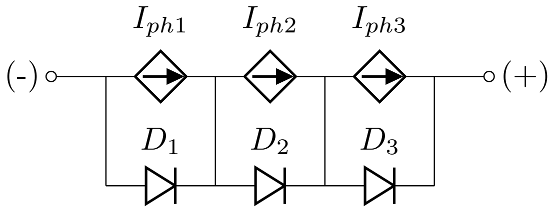

Figure 3.4: Equivalent circuit for PV module 215N from Sanyo including three strings and bypass diodes.

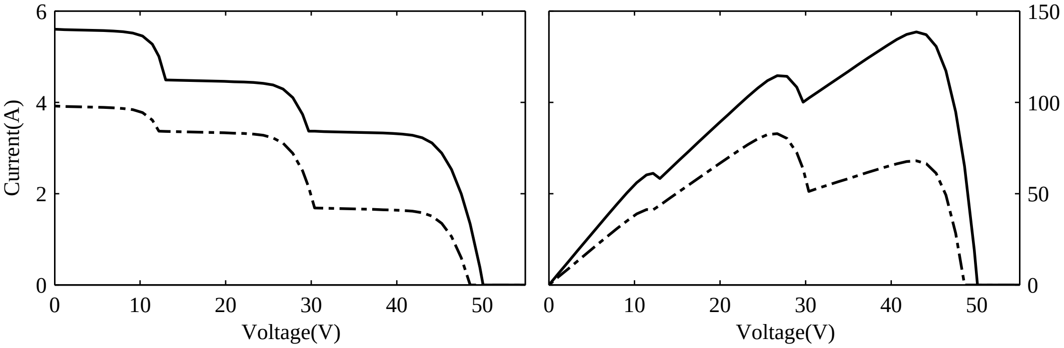

Figure 3.5: Non-unimodal P-V due to partial shading.

For the numerical PV model, we present our validation results for the PV module model 215N from Sanyo with $P^* = 215$ W, $V^* = 42$ V, $I^* = 5.13$ A, $V_{oc} = 51.6$ V,$I_{sc} = 5.61$ A, $k_v = -0.143$ V/°C, $k_i = 1.96$ mA/°C, $n_s = 72$, and $n_a = 24$ under STC. The estimates of the unknown parameters using the procedure described above are: $R_s = 2.46$ mΩ, $R_p = 8.7\ \Omega$, $\mathcal{N} = 1.81$, $I_0^r = 1.13 \times 10^{-6}$ A, and $E_g = 1.16$ eV. The result of the model verification is shown in Fig. 3.3. The derived model fits the actual data almost everywhere. The largest error happens when temperature is 0 °C.

As previously mentioned, an important feature of this model is its ability to simulate the effects of partial shading. The schematic for this module is shown in Fig. 3.4, i.e., the module has 3 strings, with 24 cells in each string. A plot of the variation of current and power of the PV module under two different partial shading conditions is shown in Fig. 3.5. Since the selected module has three bypass diodes, the power curve shows three distinct local maxima.

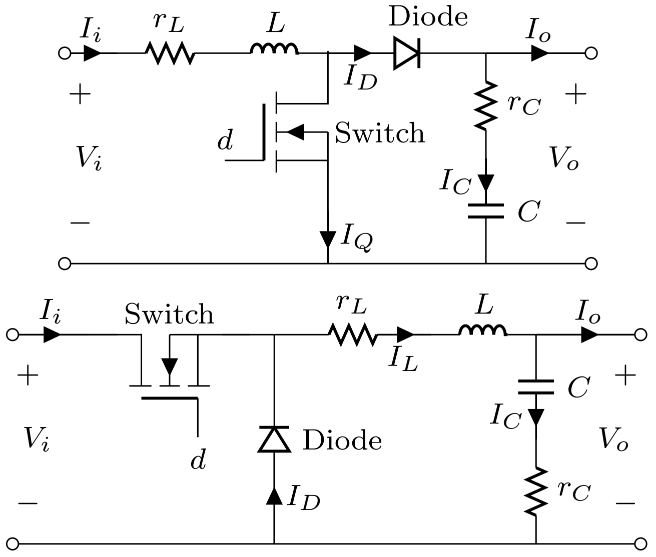

Figure 3.6: (above) Boost and (below) buck DC/DC converters.

3.4 DC/DC Converter Design and Parameter Selection

PV modules are often grid-connected through a DC/DC stage followed by an inverter, with the DC/DC converter performing the Maximum Power Point Tracking (MPPT) algorithm. The two most basic DC/DC converters are the buck and boost power stages shown in Fig. 3.6. We provide design guidelines for choosing the parameters of these two converters to fit our MPPT algorithm assuming that the DC bus has a constant voltage. Our method is based primarily on references [38, 64, 65].

3.4.1 DC/DC Buck Converter

Fig. 3.6(below) shows a simplified schematic of the buck power stage [38]. The power switch is an n-channel MOSFET. The diode is usually called the catch diode, or freewheeling diode. The inductor, L, and capacitor, C, make up the output filter. The Equivalent Series Resistance (ESR) of the capacitor, r_C, and the inductor DC resistance, r_L, are included in the analysis. The output of the converter is connected to a DC bus with constant voltage. The control signal d is the duty ratio, applied to the gate of the switch and controlled using Pulse-Width Modulation (PWM). We design the parameters so that the converter works in Continuous Conduction Mode (CCM). Assume the converter efficiency is $\bar{\eta}$, the input and output currents and voltages are related by

$$A_i = \frac{I_o}{I_i} = \frac{1}{d}, \qquad A_v = \frac{V_o}{V_i} = \bar{\eta} d, \tag{3.17}$$

where $0 \leq d \leq 1$. Since the output voltage V_o is held constant, the input voltage V_i is governed by (3.17). Let P^* and V_{oc} denote respectively the MPP and open circuit voltage of the PV module under the STC. In order to design the controller parameters, we assume that the power and voltage of PV module are bounded as assumed below

$$0.2P^* \leq \quad P_i \quad \leq 1.2P^* \tag{3.18}$$

$$0.5V_{oc} \leq \quad V_i \quad \leq 1.1V_{oc}. \tag{3.19}$$

The pulse duration and current supplied to the DC bus are then bounded as follows

$$\frac{V_o}{1.1\bar{\eta}V_{oc}} \leq \quad d \quad \leq \frac{V_o}{0.5\bar{\eta}V_{oc}} \tag{3.20}$$

$$\frac{0.2\bar{\eta}P^*}{V_o} \leq \quad I_o \quad \leq \frac{1.2\bar{\eta}P^*}{V_o}. \tag{3.21}$$

Assuming the switching frequency is f_s, the minimum inductance that is required to maintain the converter in CCM is

$$L \geq \max\left\{\frac{(1-d)R_o}{2f_s}\right\}, \tag{3.22}$$

where $R_o = V_o/I_o$. The maximum inductor ripple current is

$$\Delta I_L \leq \max\left\{\frac{(1-d)V_o}{f_s L}\right\}. \tag{3.23}$$

The ripple voltage V_r, if the filter capacitance is large enough, is $V_r = \max\{r_C \Delta I_L\}$, and the maximum ESR of C is

$$r_C \leq \min\left\{\frac{V_r}{\Delta I_L}\right\}. \tag{3.24}$$

The minimum value of the C at which the ripple voltage is determined by the ripple voltage across the ESR is

$$C \geq \max\left\{\frac{d}{2f_s r_C}, \frac{1-d}{2f_s r_C}\right\}. \tag{3.25}$$

The switch and diode voltage stress is equal to $1.1V_{oc}$. The current stress of diode and switch is $\max\{I_o + \Delta I_L/2\}$. The selected MOSFET should also have an I_D rating of at least two times the maximum power stage output current. The upper limit of RMS values of the currents are

$$\begin{aligned}
I_L^{rms} &\leq \max\{I_o\} && (3.26)\\
I_Q^{rms} &\leq \max\{I_o\sqrt{d}\} && (3.27)\\
I_D^{rms} &\leq \max\{I_o\sqrt{1-d}\} && (3.28)\\
I_C^{rms} &\leq \max\left\{\frac{\Delta I_L}{\sqrt{12}}\right\}. && (3.29)
\end{aligned}$$

The catch rectifier conducts when the power switch turns off and provides a path for the inductor current. Important criteria for selecting the rectifier include: fast switching, breakdown voltage, current rating, low-forward voltage drop to minimize power dissipation, and appropriate packaging. Unless the application justifies the expense and complexity of a synchronous rectifier, the best solution for low-voltage outputs is usually a Schottky rectifier. The breakdown voltage must be greater than the maximum input voltage, and some margin should be added for transients and spikes. The current rating should be at least two times the maximum power stage output current (normally the current rating will be much higher than the output current because power and junction temperature limitations dominate the device selection).

3.4.2 DC/DC Boost Converter

The boost power stage is depicted in Fig. 3.6(above). The input-output relations corresponding to (3.17) now are

$$A_i = \frac{I_o}{I_i} = 1 - d, \qquad A_v = \frac{V_o}{V_i} = \frac{\bar{\eta}}{1-d}. \tag{3.30}$$

Assuming the bounds in (3.18) and (3.19) for the voltage and power variation to still hold, the pulse duration and output (DC bus) current are then bounded as

$$\begin{aligned} 1-\frac{1.1\bar{\eta}V_{oc}}{V_o} \leq \quad & d \quad \leq 1-\frac{0.5\bar{\eta}V_{oc}}{V_o} && (3.31) \\ \frac{0.2\bar{\eta}P^*}{V_o} \leq \quad & I_o \quad \leq \frac{1.2\bar{\eta}P^*}{V_o}. && (3.32) \end{aligned}$$

The minimum inductance that ensures CCM operation at any duty cycle d then is

$$L \geq \frac{\max\{R_o\}}{13.5 f_s}, \tag{3.33}$$

where $R_o = V_o/I_o$. The maximum inductor peak-to-peak current of the AC component is

$$\Delta I_L \leq \max\left\{\frac{(1-d)dV_o}{f_s L}\right\}. \tag{3.34}$$

The current and voltage stresses of the MOSFET and the diode are $\max\{I_o/(1-d) + d(1-d)V_o/(2f_sL)\}$ and V_o, respectively. The selected MOSFET should also have a maximum drain current rating I_D of at least two times the maximum power stage output current so as diode. Let us assume that the ripple voltage, V_r, is equally divided between the capacitance and the ESR. Hence, the maximum ESR and the minimum filter capacitance are respectively shown by

$$\begin{aligned} r_C \quad & \leq \quad 0.5\frac{V_r}{\max\{I_D\}} && (3.35) \\ C \quad & \geq \quad \max\left\{\frac{2dV_o}{f_s R_o V_r}\right\}. && (3.36) \end{aligned}$$

The upper limit of RMS values of the currents are

$$\begin{aligned} I_L^{rms} \quad & \leq \quad \max\left\{\frac{I_o}{1-d}\right\} && (3.37) \\ I_Q^{rms} \quad & \leq \quad \max\left\{\frac{I_o\sqrt{d}}{1-d}\right\} && (3.38) \\ I_D^{rms} \quad & \leq \quad \max\left\{\frac{I_o}{\sqrt{1-d}}\right\} && (3.39) \\ I_C^{rms} \quad & \leq \quad \max\left\{I_o\sqrt{\frac{d}{1-d}}\right\}. && (3.40) \end{aligned}$$

The power loss contributions from the different components for both converters are tabulated in Table 3.1.

Table 3.1: Power losses in buck and boost converters.

Power loss	Buck	Boost
Q-conduction	$R_{DS}\max\{I_Q^{rms}\}^2$	$R_{DS}\max\{I_Q^{rms}\}^2$
Q-switching	$0.5 f_s C \max\{V_i\}^2$	$0.5 f_s C V_o^2$
D-V_f	$V_f \max\{(1-d)I_o\}$	$V_f \max\{I_o\}$
D-conduction	$R_f \max\{I_D^{rms}\}^2$	$R_f \max\{I_D^{rms}\}^2$
C-ESR	$r_C \max\{I_C^{rms}\}^2$	$r_C \max\{I_C^{rms}\}^2$
L-ESR	$r_L \max\{I_o\}^2$	$r_L \max\{I_L^{rms}\}^2$

Table 3.2: Design details for buck and boost converters.

Element	Buck	Boost	Unit
Switch	IRFU3607	IRFI540N	–
Diode	DSSS 35-008AR	DSS 16-01A	–
L	15	150	μH
r_L	6	25	mΩ
C	270	680	μF
r_C	11	28	mΩ
DC bus voltage	24	84	V
$\bar{\eta}$	93	94	%

The parameter selection is based in part on the PV module, which in our case is the 215N from Sanyo. According to the design criteria described for a targeted efficiency of $\bar{\eta} = 95\%$ for both the boost as well as the buck configuration, we select the components of the buck and boost converters as shown in Table 3.2. Clearly the actual design efficiency is very close to what was designed for.

3.5 Conclusions

In conclusion we have presented high-fidelity PV and Power Electronic (PE) models to start with the MPPT, and provide numerically accurate estimates of power losses and efficiencies in actual hardware implementations. The numerical models we develop are versatile, i.e, can be tuned for a variety of PV modules and converters, and have been successfully validated against manufacturer data. The modeling effort is also valuable in its own right in that it presents a designer with high-fidelity PV/PE models for SimPowerSystems$^{\text{TM}}$, traditionally developed using SPICE, with the advantage that they can be convenient integrated with control design for such systems.

This chapter contains material from A. Ghaffari, S. Seshagiri, and M. Krstić, “High-fidelity PV module modeling for advanced MPPT design,” in *Proc. of IEEE*

Canadian Conference on Electrical and Computer Engineering, 2012 and A. Ghaffari, S. Seshagiri, and M. Krstić, "High-fidelity DC-DC converter modeling for advanced MPPT design," in *Proc. of IEEE Canadian Conference on Electrical and Computer Engineering*, 2012. Of which the dissertation author was the primary author.

Chapter 4

Maximum Power Point Tracking in Photovoltaic Systems

In Chapter 2 we developed the Newton-based ES algorithm for peak seeking of a multivariable cost function joint with a dynamic system for which we do not have the system dynamics and cost function model. But the cost function is measurable and we can reach its peak point by manipulating the input vector, appropriately. We apply the Newton-based ES algorithm to maximize the generated power by a PV system. In Chapter 3 we presented high-fidelity models for PV modules and DC/DC power stages. Also, we provided detailed guide lines to design a DC/DC power stage in CCM for an arbitrary PV module. In this chapter we combine the results of Chapter 2 and 3 for power optimization of a PV system.

4.1 Introduction

Maximum Power Point Tracking (MPPT) algorithms for extracting the maximum achievable power from a Photovoltaic (PV) system have been studied by several researchers [23, 53, 58, 61, 63], with detailed comparisons presented in [25, 32, 35]. Several recent works [12, 15, 47, 55] have focused on the application of gradient-based Extremum Seeking (ES) [6] to MPPT design.

To the best of our knowledge, there are a limited number of multivariable MPPT schemes described in the literature, among which we refer the reader to [53, 61, 63]. The last of these references [63] uses a multivariable version of the popular Perturb and Observe (P&O) algorithm. Unlike scalar designs which require one current sensor for each module, the algorithm only requires a single current sensor on the DC bus. The operating point of the DC/DC converters are perturbed asynchronously, to minimize the possibility of converter interaction having a detrimental effect on the other modules. Closely related to [63] is the work in [61], where "extra variables" are employed in the classical P&O algorithm to overcome the limitation of scalar designs, which the authors say fail when the feasibility region is nonconvex. It is unclear how [61] compares with distributed architectures, with respect to power loss recovery in the case of module mismatch. Reference [53] uses Particle Swarm Optimization (PSO), which is an algorithm that employs multiple agents to "search" for the peak power. The paper does not describe the specific criteria used to select the number of agents and parameters of the PSO, nor the conditions on the voltage and power boundary limits to stop the algorithm at Maximum Power Point (MPP). Also, in a PV system with a higher number of PV modules, the process of reinitialization and the tracking performance depend strongly on variable conditions like environmental factors, the nature of the PV modules, and the shading area. The authors claim that the required number of sensors are reduced to two, but to compute the pulse duration, the output voltage of each boost converter needs to be monitored by a separate sensor.

Expansion of the conventional P&O MPPT methods to the case of cascade PV modules with micro-converters (one DC-DC converter for each module) as presented in [63] requires a step-by-step perturb and observe, namely the core part of the algorithm is a scalar P&O which finds the MPP of each PV module at a time. This results in a longer conversion time. Furthermore, non-unimodal power characteristics which mainly arise from partial shading and model mismatch cannot be treated which cause non-uniform transient responses under different environmental conditions. This problems holds in the PSO method of [53]. Multivariable ES, unlike the other MPPT approaches, treats the entire cascade PV system as a whole and it simply fits every PV system architecture without any need to redesign the control loop.

In [29], we presented a multivariable gradient-based ES MPPT design for the micro-converter architecture, where each PV module is coupled with its own DC-DC converter. The design reduced the balance-of-system cost by reducing the number of required sensors (hardware reduction), and was shown to result in more uniform transients under sudden changes in solar irradiance and environmental temperature in comparison to a scalar gradient-based ES for each PV module. However, the convergence to the MPP is dependent on the unknown Hessian, which varies with irradiance, temperature, and module degradation and mismatch.

In order to alleviate the issue of unknown Hessian dependent convergence of a gradient-based ES algorithm, we presented a multivariable Newton-based ES design for general nonlinear system in [28]. In comparison with the standard gradient-based multivariable ES, the algorithm in [28] removes the dependence of the convergence rate on the unknown Hessian and makes the convergence rate of the parameter estimates user-assignable. In particular, all the parameters can be designed to converge with the same speed, yielding straight trajectories to the extremum even with maps that have highly elongated level sets. When applied to the MPPT problem in PV systems, the method offers the benefit of uniform convergence behavior under a wide range of working conditions, that includes temperature and irradiance variations, and the non-symmetric power generation of the neighboring PV modules as a result of module degradation or mismatch.

We present a multivariable Newton-based ES scheme with the following features: (1) It is applied to micro-converter systems, and hence deals with the case of non-unimodal power characteristics, and deals specifically with the issue of module mismatch (for example, possibly different irradiance levels as a result of partially shaded conditions). (2) The use of the non-model-based ES technique makes the design robust to partial knowledge of the system parameters and operating conditions. (3) As opposed to gradient-based designs, our proposed Newton-based design removes the dependence of the transient on the working condition and potential mismatch in PV modules. (4) Lastly, the multivariable design requires fewer sensors, which reduces the hardware cost compared to scalar designs.

Section 4.2 presents an MPPT algorithm based on extremum seeking for a

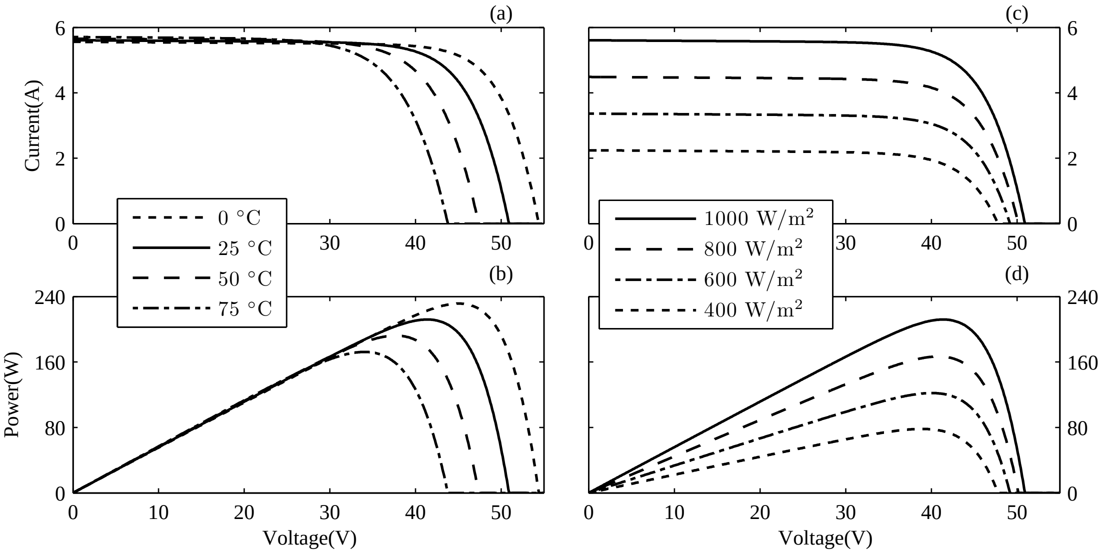

Figure 4.1: Characteristic (a) I-V and (b) P-V for varying temperature, $\mathcal{S}$=1000W/m^2. Characteristic (c) I-V and (d) P-V for varying irradiance, $\mathcal{T}$=25°C, PV module 215N from Sanyo.

single PV module. In Section 4.3 we present the idea of micro-converter architecture. Section 4.4 summarizes the multivariable gradient-based ES scheme in [29], and allows us to present key distinctions with the proposed design. Our proposed multivariable Newton-based ES is presented and discussed in Section 4.5. Some simulation results are presented in Section 4.6. The experimental verification of the proposed algorithms are presented in Section 4.7 and our work is summarized and some concluding remarks made in Section 4.8.

4.2 Power Optimization of a Single Photovoltaic Module

As is clear from Fig. 4.1(b,d), the power-voltage (P-V) characteristic has a unique but $(\mathcal{T}, \mathcal{S})$ dependent peak (V^*, P^*). It is the job of the MPPT algorithm to automatically track this peak. In many grid-tied PV systems (including our current work), this is done by means of a separate DC/DC power electronics stage that serves two functions: (i) regulating the output DC voltage at a (near) constant

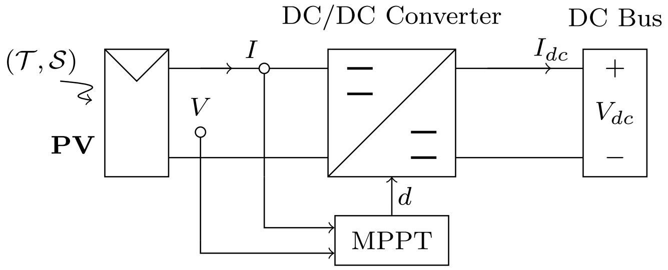

Figure 4.2: DC/DC converter for PV module supplying power to DC bus.

value, and (ii) extracting maximum power by forcing the PV module output V to equal V^*. Fig. 4.2 shows this setup for a DC/DC boost converter stage, whose output voltage is maintained constant as V_{dc}. The ratio between the input voltage V and output voltage V_{dc} can be controlled by changing the duty cycle of the transistor switch, which serves as the control input d. Under the assumption that the boost converter is working in Continuous Current Mode (CCM), and that the switching Pulse Width Modulation (PWM) frequency f_s is significantly higher than the bandwidth of the control loop, the boost converter input-output voltage relationship is given by the following (averaged) relations:

$$V = (1-d)\bar{\eta}V_{dc} \tag{4.1}$$

$$I_{dc} = (1-d)I, \tag{4.2}$$

where $\bar{\eta}$ is the power efficiency of the boost converter.

From (3.4), (4.1) and Fig. 4.1(b,d), it follows that at the MPP (V^*,P^*), the power $P = IV = F(V)V \overset{\text{def}}{=} J(V)$, satisfies

$$g = \frac{\partial J}{\partial V}(V^*) = 0 \tag{4.3}$$

$$h = \frac{\partial^2 J}{\partial V^2}(V^*) < 0. \tag{4.4}$$

Also we have $\partial V/\partial d = -\bar{\eta}V_{dc}$ then

$$\bar{g} = \frac{\partial J}{\partial d}(d^*) = -g\bar{\eta}V_{dc} = 0 \tag{4.5}$$

$$\bar{h} = \frac{\partial^2 J}{\partial d^2}(d^*) = h\bar{\eta}^2V_{dc}^2 < 0. \tag{4.6}$$

Many MPPT techniques, including the P&O class of methods, and the ES techniques, are based on detecting the sign of the power gradient.

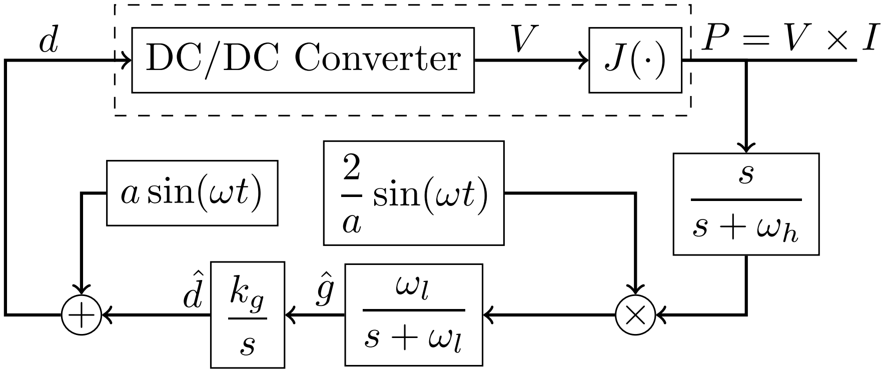

Figure 4.3: Scalar ES for MPPT of a PV module.

Several authors have considered to use scalar gradient-based ES for the MPPT problem [12, 15, 47, 48, 55]. Fig. 4.3 shows the basic setup of the scheme for the case of a single PV module, and its principal features have been explained fairly clearly in the aforementioned references, but we reproduce them here for the sake of completeness/clarity.

The injection of the small periodic perturbation $a\sin(\omega t)$ to the estimate $\hat{d}$ of the optimal pulse duration d^* results in a periodic power output P, whose DC component is removed by the wash-out filter $s/(s+\omega_h)$, with the resultant signal being in phase or out of phase with the perturbation according to whether $\hat{d}$ is greater than or less than d^* respectively. Multiplication of this signal by $2\sin(\omega t)/a$ and extracting the DC component of the product using the lowpass filter $\omega_l/(s+\omega_l)$ results in an estimate of the gradient of the cost function. Defining $\tilde{d} = \hat{d} - d^*$, and expanding P about its optimal value and using (4.3), (4.4), we see that the ES design of Fig. 4.3 implements the gradient update law

$$\dot{\tilde{d}} = k_g \bar{h} \tilde{d} = k_g \bar{\eta}^2 V_{dc}^2 h \tilde{d}, \tag{4.7}$$

where h is the Hessian. Design guidelines for selecting the parameters a, ω, ω_h, ω_l, and k_g can be found in [45], but are mentioned here for sake of completeness. The frequency ω must be chosen small enough to ensure that the plant dynamics appear as a static nonlinearity from the viewpoint of the ES loop, and the filter frequencies chosen such that $\omega_h \leq \omega_l \ll \omega$, so that the low pass filter attenuates the perturbation frequency, whereas the highpass filter does not. The adaptation

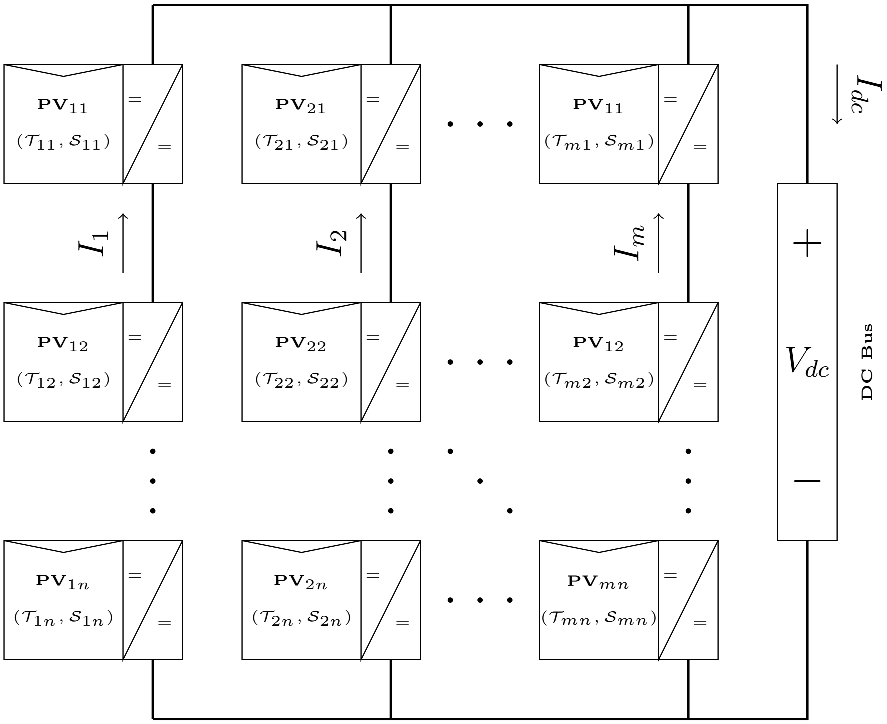

Figure 4.4: Microconverter architecture. PV system including m parallel strings. Each string has n PV modules in cascade.

gain k_g and the amplitude a of the probing signal need to be "sufficiently small". Define

$$\omega_l = \epsilon\delta\omega_l' \tag{4.8}$$

$$\omega_h = \epsilon\delta\omega_h' \tag{4.9}$$

$$k_g = \epsilon\delta k_g', \tag{4.10}$$

where ϵ and δ are small positive real numbers, and ω_h', ω_l' and k_g' are $O(1)$ positive real parameters. The analysis of [45] shows that for sufficiently small ϵ, a, and δ, the output P converges to an $O(\epsilon + \delta + a)$-neighborhood of the MPP P^*.

4.3 Micro-Converter Architecture

The above design for a single module can be extended to the PV system shown in Fig. 4.4, that has m parallel strings, with each string having n modules in cascade (series). Since irradiance (and temperature to a lower extent) may vary between the modules, the peak power is not necessarily the same for all of them. This “module mismatch” therefore results in maximum powers for string architectures that are lower than the sum of the individual maximum powers of the modules, which in turn has led to the use of micro-converters, where each module is coupled with its own DC/DC converter. Micro-converter architectures can recover between 10%-30% of annual performance loss caused due to module mismatch. The conventional way to implement the MPPT algorithm in micro-converters is to simply extend the preceding (scalar) MPPT design to each PV module, as shown in Fig. 4.5 for one string. We therefore have n separate control loops, with no consideration to the interaction between the series modules. We also still have two sensors per module, that measure the module voltage and current. The multivariable control algorithm that we present in the next section alleviates both these issues; on the one hand, it considers the interaction between modules, resulting in better performance, and in addition, uses just two sensors for the overall system. The details of the actual design are presented in the next section.

A DC/DC boost converter is assigned to each PV module to extract maximum power from the PV system. The output side of the converters are connected in series. The PV system is connected to the power grid through a DC/AC inverter which has its separate controller. A popular scheme to control the voltage of DC bus and the power factor at the connection of the grid is shown in Fig. 4.6. This scheme uses the famous Park’s transformation to convert the three-phase parameters to two dimensional synchronous reference frame. In this reference frame q-axis affects the reactive power and the $d-$axis deals with the variation of the DC bus voltage [19].

It is assumed that the DC voltage at the input side of the inverter is held constant at V_{dc}. Assume that the voltage and current ripple at the output side of converters are negligible. Applying electrical rules on the input side of the inverter

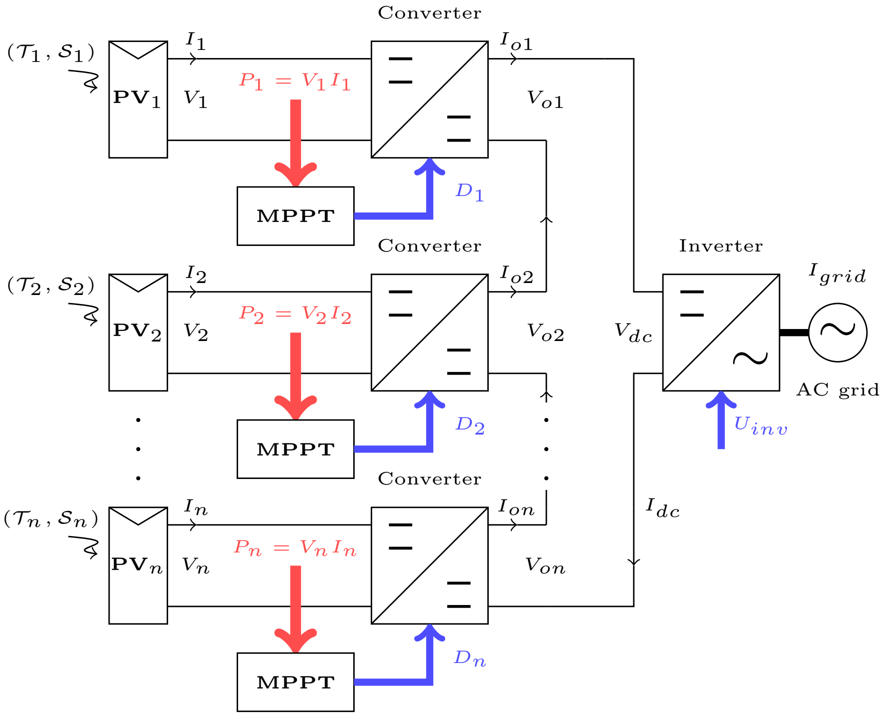

Figure 4.5: Distributed MPPT for one string. One scalar ES loop is used for each PV module.

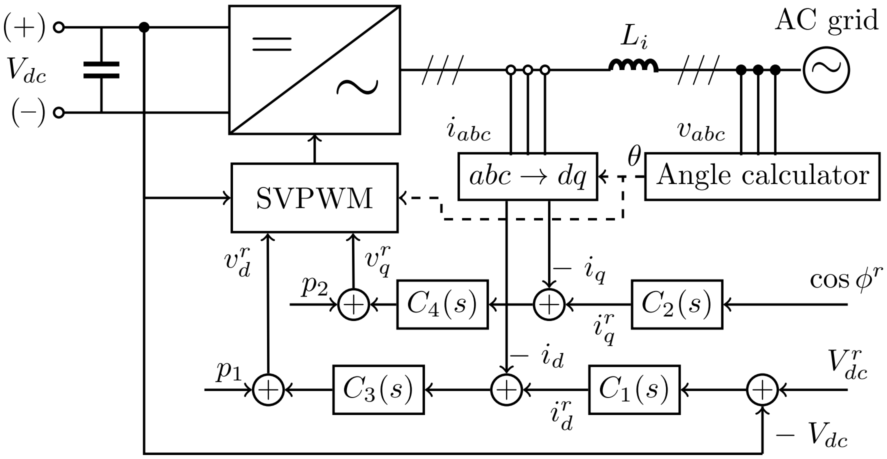

Figure 4.6: DC bus voltage and inverter control scheme for a distributed generator as presented in [19].

gives

$$\begin{aligned}\sum_{i=1}^{n} V_{oi} &= V_{dc} &(4.11)\\ I_{oi} &= I_{dc}, \quad \forall i \in \{1, 2, \cdots, n\}. &(4.12)\end{aligned}$$

From (4.1), (4.2), and the I-V functional dependence $I_i = F_i(V_i)$, the relation between the voltage $V = [V_1\ V_2\ \cdots\ V_n]^T$ of PV modules and the pulse duration $D = [D_1\ D_2\ \cdots\ D_n]^T$ is defined by n independent equations

$$\begin{aligned}\sum_{i=1}^{n} \frac{V_i}{1 - D_i} &= V_{dc} &(4.13)\\ (1 - D_i)F_i(V_i) &= I_{dc}, \quad \forall j \in \{1, 2, \cdots, n\}. &(4.14)\end{aligned}$$

This means that for each set of pulse duration we have a unique set of voltages for PV modules. Assuming lossless converters results in $P_{oi} = V_{oi}I_{oi} = P_i$ for all $i \in \{1, 2, \cdots, n\}$. Using (4.12) we obtain

$$V_{oi} = \frac{P_i}{\sum_{j=1}^{n} P_j} V_{dc}, \tag{4.15}$$

which means that the share of the output voltage of each converter from DC bus voltage is defined by the generated power of its relevant PV module.

We want to maximize the power generated by all PV modules which is equal

$$P = \sum_{i=1}^{n} P_i = V_{dc} I_{dc}. \tag{4.16}$$

The following observation is valid about the power.

Remark 3 *From (4.13)-(4.16), it follows that there exists $D^* \in \mathbb{R}^n$ such that*

$$\begin{aligned}\frac{\partial P}{\partial D}(D^*) &= 0 &(4.17)\\ \frac{\partial^2 P}{\partial D^2}(D^*) &= H < 0, \qquad H = H^T. &(4.18)\end{aligned}$$

The next section discusses gradient-based ES for the micro-converter architecture in Fig. 4.4, and is extracted from [29].

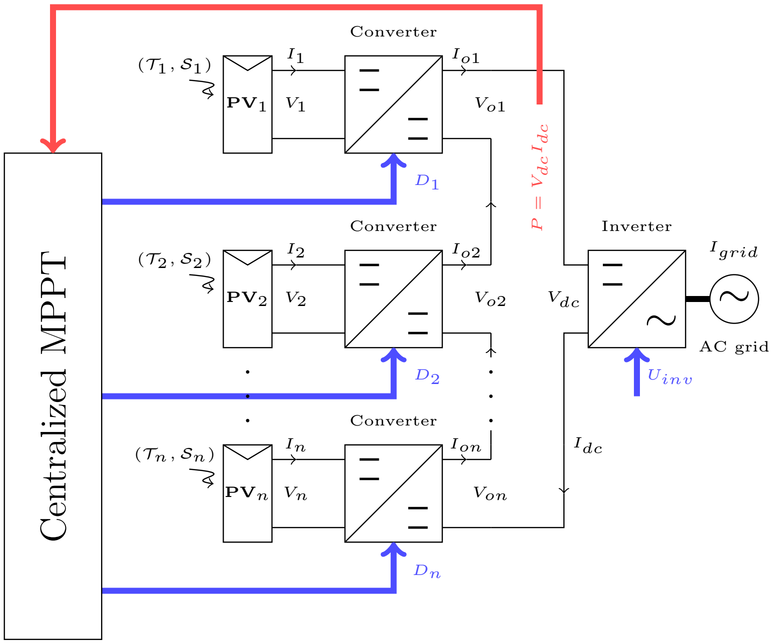

Figure 4.7: Our proposed centralized MPPT for PV system, just one multivariable ES loop is employed for all PV modules.

4.4 Multivariable Gradient-Based ES

A block schematic of our proposed multivariable gradient-based ES is shown in Fig. 4.7. As is clear from the schematic, the design employs just one ES loop with two sensors for the overall system, one each for the DC bus voltage V_{dc} and the overall current I_{dc}.

Fig. 4.8 shows the multivariable gradient-based ES design, where K_g is a positive diagonal matrix, and the perturbation signals are defined as

$$S(t) = a \left[\sin(\omega_1 t) \quad \cdots \quad \sin(\omega_n t) \right]^T \tag{4.19}$$

$$M(t) = \frac{2}{a} \left[\sin(\omega_1 t) \quad \cdots \quad \sin(\omega_n t) \right]^T, \tag{4.20}$$

where ω_i/ω_j are rational for all i and j, and a is a real number, with the frequencies chosen such that $\omega_i \neq \omega_j$ and $\omega_i + \omega_j \neq \omega_k$ for distinct j, k, and m.

In particular, the design derives an estimate $\hat{G}$ of the gradient vector by adding a probing signal to the estimate $\hat{D} = [\hat{D}_1 \; \hat{D}_2 \; \cdots \; \hat{D}_n]^T$ of the pulse duration vector (of all the DC/DC converters). With no additional information on the

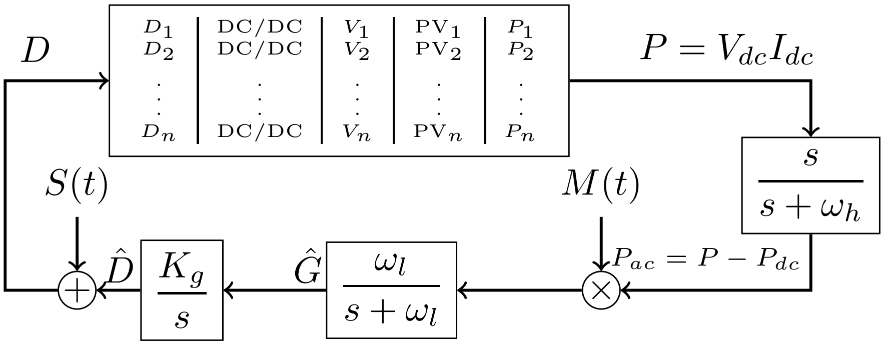

Figure 4.8: Multivariable gradient-based ES for MPPT of a PV system.

Hessian (and also for simplicity), we choose the amplitudes of the probing signals to all be the same value a. Smallness of the probing frequencies and the matrix gain K_g are ensured by selecting these as

$$\omega_i = \epsilon\omega_i', \quad i \in \{1, 2, \cdots, n\} \tag{4.21}$$

$$\omega_h = \epsilon\delta\omega_h' \tag{4.22}$$

$$\omega_l = \epsilon\delta\omega_l' \tag{4.23}$$

$$K_g = \epsilon\delta K_g' \tag{4.24}$$

where ϵ and δ are small positive constants, and ω_i', ω_h', ω_l' and elements of K_g' are $O(1)$ positive real parameters. It can be shown that for sufficiently small ϵ, δ, and a, and with $K_g > 0$, the estimate $\hat{D}$ of the pulse duration vector and the output P converge to $O(\omega + \delta + a)$-neighborhoods of the optimal pulse duration $D^* = [D_1^* \; D_2^* \; \cdots \; D_n^*]^T$ and the peak power $P(D^*)$ respectively.

Applying Taylor series expansion to $P(D, t)$ at its maximum point, and noting that $D = D^* + \tilde{D} + S(t)$, we have

$$P = P^* + \frac{1}{2}\left(\tilde{D} + S(t)\right)^T H \left(\tilde{D} + S(t)\right) + R(\tilde{D} + S(t)), \tag{4.25}$$

where $\partial P(D^*)/\partial D = 0$ and $R(\tilde{D} + S(t))$ stands for higher order terms in $\tilde{D} + S(t)$. We separate (4.25) to averaged, DC-part, and oscillatory, AC-part, as follows

$$P = P_{dc} + P_{ac}, \tag{4.26}$$

where

$$P_{dc}{=}P^* + \frac{1}{2}\tilde{D}^T H\tilde{D} + R_{dc}(\tilde{D}) \tag{4.27}$$

$$P_{ac}{=}S^T(t)H\tilde{D}{+}\frac{1}{2}S^T(t)HS(t){+}R_{ac}(\tilde{D}{+}S(t)), \tag{4.28}$$

where $R_{dc}(\tilde{D})$ and $R_{ac}(\tilde{D}+S(t))$ are higher order DC and AC terms, respectively. The highpass filter attenuates the DC-part of the power signal while keeps the high frequency part. Denoting

$$M(t)S^T(t) = I_{n\times n} + Z_{n\times n}, \tag{4.29}$$

where

$$Z_{ii}{=}-\cos(2\omega_i t) \tag{4.30}$$

$$Z_{ij}{=}\cos\Big((\omega_i-\omega_j)t\Big) - \cos\Big((\omega_i+\omega_j)t\Big),\ i\neq j, \tag{4.31}$$

we obtain

$$M(t)P_{ac} = H\tilde{D} + ZH\tilde{D} + O(a), \tag{4.32}$$

where $O(a)$ contains terms of the order of a. From (4.25) we know that the gradient vector of the cost function is $G = \partial P/\partial\tilde{D} = H\tilde{D}$. Hence, the DC-part of the multiplication of $M(t)$ and P_{ac} which equals to $H\tilde{D}$ is the estimate of the gradient vector of the cost function. An appropriate selection of the lowpass filter removes the oscillatory part of $M(t)P_{ac}$. Regardless of the vector length, n, the same lowpass filter on every channel of the gradient vector guarantees the averaging process and proper attenuation of the high frequency terms. Referring to (4.30), (4.31), and (4.32) it is clear that the main harmonics in the estimate of the gradient vector are $2\omega_i$, $\omega_i \pm \omega_j$ for all distinct i and j. Following condition is assumed for the lowpass filter to estimate the gradient vector enough precise

$$\omega_l \ll \{|\omega_i-\omega_j|\}, \qquad \forall i\neq j. \tag{4.33}$$

Our analytical results for MPPT of PV systems using the multivariable gradient-based ES are summarized in the theorem below, the proof of which follows from [45].

Theorem 3 *For the system in Fig. 4.8, with Remark 3, there exist* $\bar{\delta}, \bar{a} > 0$ *and for any* $|a| \in (0, \bar{a})$ *and* $\delta \in (0, \bar{\delta})$, *there exists* $\bar{\epsilon} > 0$ *such that for any given* a *and* δ *and any* $\epsilon \in (0, \bar{\epsilon})$ *there exists a neighborhood of the point* $(\hat{D}, \hat{G}, P_{dc}) = (D^*, 0, P(D^*))$ *such that any solution of the gradient-based ES from the neighborhood exponentially converges to an* $O(\epsilon + \delta + |a|)$*-neighborhood of that point. Furthermore,* $P(D, t)$ *converges to an* $O(\epsilon + \delta + |a|)$*-neighborhood of* $P(D^*)$.

The differences between the scalar and multivariable designs become clear when one considers the update equations for the estimation error $\tilde{D} = \hat{D} - D^*$. In the multivariable case, we have

$$\dot{\tilde{D}} = K_g H \tilde{D}, \quad H := \frac{\partial^2 P}{\partial D^2}(D^*) \tag{4.34}$$

where H is the (negative definite) Hessian and $P = V_{dc} I_{dc}$. In the scalar ES design of Fig. 4.5 however, the above equation is replaced by

$$\dot{\tilde{D}} = k_g \mathcal{H} \tilde{D} \tag{4.35}$$

$$\mathcal{H} := \begin{bmatrix} \bar{h}_{PV_1} & 0 & 0 & \cdots & 0 \\ 0 & \bar{h}_{PV_2} & 0 & \cdots & 0 \\ \vdots & \vdots & \vdots & \ddots & \vdots \\ 0 & 0 & 0 & \cdots & \bar{h}_{PV_n} \end{bmatrix}, \tag{4.36}$$

where $\bar{h}_{PV_i} = \partial^2 P_i / \partial d_i^2$ and $P_i = V_i I_i$ for all i (see Fig. 4.5), so that the equations are decoupled, and there is no way to affect the power extraction in one module by changing the pulse duration of the DC/DC converter of another module. In addition, the diagonal structure of $\mathcal{H}$ in the scalar case, coupled with the fact that this varies with irradiance, means that in the scalar design, the convergence rate of the parameters is very sensitive to partial shading, where the irradiance varies strongly from one module to another. The multivariable scheme, on the other hand, is less sensitive to the changes in the power-voltage characteristic of a specific module which results from variation of temperature or irradiance.

In order to alleviate the issue of unknown Hessian dependent convergence, we present in the next section a modified version of a multivariable Newton-based ES design that we developed in [28].

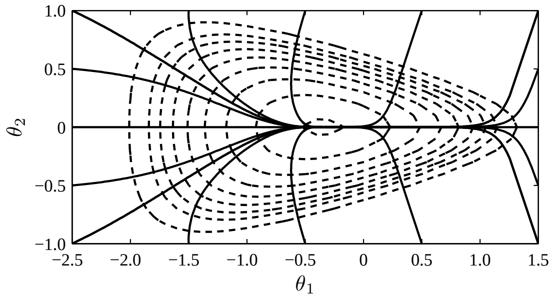

Figure 4.9: Cost function shape defines the convergence trajectory of the gradient-based ES scheme.

4.5 Multivariable Newton-Based ES

In comparison with the gradient-based multivariable ES presented in Section 4.4, the Newton-based algorithm makes the convergence rate of the parameter estimates user-assignable. In particular, all the parameters can be designed to converge with the same speed, yielding straight trajectories to the extremum even with maps that have highly elongated level sets. As shown in Fig. 4.9 the cost function shape defines the convergence trajectories of the gradient-based scheme. It is clear that the gradient method governs the system to its steepest-decent curve. The Newton scheme moves the system on a direct path to its peak point independent of the cost function shape which results in uniform transients for any initial conditions. When applied to the MPPT problem in PV systems, the method offers the benefit of uniform convergence behavior under a wide range of working conditions, that include temperature and irradiance variations, and the non-symmetric power generation of the neighboring PV modules as a result of module degradation or mismatch.

The multivariable Newton-based ES that we propose is shown schematically in Fig. 4.10. As is clear from the figure, the proposed scheme extends gradient-based ES with estimate of the Hessian. The perturbation matrix $N(t)$ is defined as follows

$$N_{ii} = \frac{16}{a^2}\left(\sin^2(\omega_j t) - \frac{1}{2}\right) \tag{4.37}$$

$$N_{ij} = \frac{4}{a^2}\sin(\omega_j t)\sin(\omega_k t), \quad i \neq j \tag{4.38}$$

where $i, j \in \{1, 2, \cdots, n\}$. The product of $N(t)$ and P_{ac} generates an initial estimate of the Hessian

$$N(t)P_{ac} = \frac{1}{2}NS^THS + NS^TH\tilde{D} + O(a). \tag{4.39}$$

While the elements of $NS^TH\tilde{D}$ are of the order of $O(1/a)$ and have the harmonics of ω_i, $\omega_i \pm \omega_j \pm \omega_k$, and $2\omega_i \pm \omega_j$ for all distinct values of i, j, and k, the first term, $NS^THS/2$, is of the order of $O(1)$ and generates a DC value equal to the Hessian, H. The reminders are oscillatory parts of the order of $O(a)$ which can be neglected in comparison to the other two parts. Since a is a small value, then it is critical to remove $O(1/a)$ terms from the initial estimate of the Hessian, $N(t)P_{ac}$, to achieve a reliable estimate of the Hessian. For this purpose, we design the lowpass filter with respect to the lowest harmonic of ω_i, $\omega_i - \omega_j - \omega_k$, and $2\omega_i - \omega_j$ for all distinct i, j, and k. Also we remind the reader that lowpass filter which estimates the gradient vector needs to alleviate the harmonics at $2\omega_j$ and $\omega_i - \omega_j$ for all distinct i and j. High band-width lowpass filters do not attenuate the AC-part of $N(t)P_{ac}$ with enough precision, then the estimate of the Hessian may be an indefinite matrix which results in the failure of the Newton algorithm. For this reason we suggest to design the lowpass filters based on the following criteria

$$\omega_l \ll \min\{\omega_i, |\omega_i - \omega_j|, |\omega_i - \omega_j - \omega_k|, |2\omega_i - \omega_j|\} \tag{4.40}$$

for all distinct i, j, and k. The corner frequency of the lowpass filter which is designed with respect to the probing frequencies and their least difference affects the convergence rate of the ES algorithm. We advise the same adaptation rate for the estimate of the gradient vector and the Hessian matrix.

The inverse of the Hessian that is needed to implement the Newton algorithm, is estimated by a dynamic filter that has the form of a Riccati equation, and avoids the possible problem in inverting the Hessian if the estimate $\hat{H}$ is close

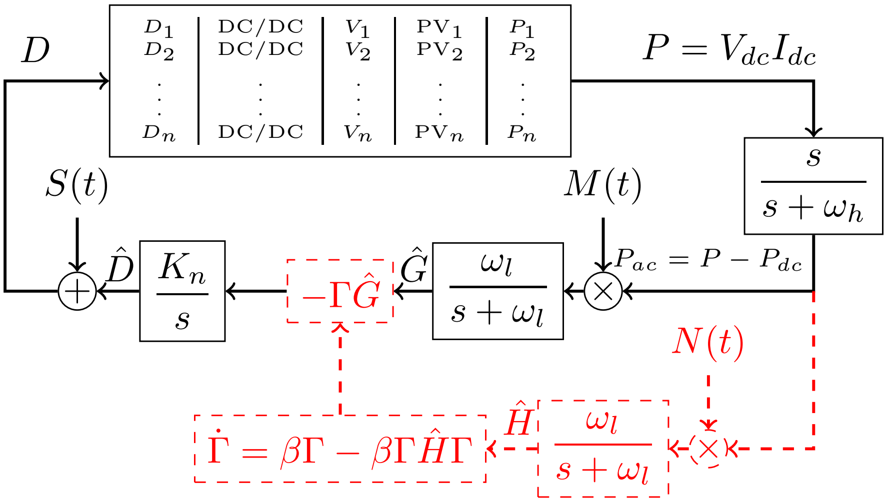

Figure 4.10: Multivariable Newton-based ES for MPPT of a PV system. The red dashed part is added to the gradient-based ES to estimate the Hessian.

to singularity. Calculating Γ, the estimate of the inverse of the Hessian, in an algebraic fashion creates difficulties when the matrix $\hat{H}$ is close to singularity, or it is indefinite. To deal with this problem, a dynamic estimator is employed to calculate the inverse of $\hat{H}$ using a Riccati equation. Consider the following filter

$$\dot{\mathcal{H}} = -\beta\mathcal{H} + \beta\hat{H}, \quad \beta = \epsilon\delta\beta', \tag{4.41}$$

where β' is of the order of $O(1)$.

Note that the state of this filter converges to $\hat{H}$, an estimate of H. Denote Γ=$\mathcal{H}^{-1}$. Since $\dot{\Gamma} = -\Gamma\dot{\mathcal{H}}\Gamma$, then equation (4.41) is transformed to the differential Riccati equation

$$\dot{\Gamma} = \beta\Gamma - \beta\Gamma\hat{H}\Gamma. \tag{4.42}$$

The equilibria of the Riccati equation (4.42) are $\Gamma^* = 0_{n\times n}$ and $\Gamma^* = \hat{H}^{-1}$, provided $\hat{H}$ settles to a constant. Since $\beta > 0$, the equilibrium $\Gamma^* = 0$ is unstable, whereas the linearization of (4.42) around $\Gamma^* = \hat{H}^{-1}$ has the Jacobian $-\beta I_{n\times n}$, so the equilibrium at $\Gamma^* = \hat{H}^{-1}$ is locally exponentially stable. This shows that, after a transient, the Riccati equation converges to the actual value of the inverse of Hessian matrix if $\hat{H}$ is a good estimate of H.

Since we are integrating over a finite time period, and we set the phase delays of the periodic perturbation signals equal to zero, it is possible to exclude the condition $\omega_i \neq \omega_j + \omega_k$ for all distinct $i,\ j$, and k. The probing frequencies need to satisfy (see [28] for more details)

$$\omega_i \notin \left\{\omega_j, \frac{1}{2}(\omega_j + \omega_k), \omega_j + 2\omega_k, \omega_j + \omega_k \pm \omega'_m\right\}, \tag{4.43}$$

for all distinct $i,\ j,\ k$, and m.

Linearization of the update law for the error variable $\tilde{D} = \hat{D} - D^*$ results in

$$\dot{\tilde{D}} = -K_n\tilde{D}, \qquad K_n = \epsilon\delta K'_n > 0, \tag{4.44}$$

where elements of K'_n are $O(1)$ positive real numbers. According to (4.44) the convergence rate of the parameter is independent of the shape of the cost function, and consequently, after transient, when the Hessian is close enough to its actual value, the output power converges to the MPP with the same performance regardless of environmental or mismatch conditions. The analytical results for MPPT of PV systems using multivariable Newton-based ES are summarized in the theorem below, the proof of which follows from Chapter 2.

Theorem 4 *For the system in Fig. 4.10, with Remark 3, there exist* $\bar{\delta}, \bar{a} > 0$ *and for any* $|a| \in (0, \bar{a})$ *and* $\delta \in (0, \bar{\delta})$*, there exists* $\bar{\epsilon} > 0$ *such that for any given* a *and* δ *and any* $\epsilon \in (0, \bar{\epsilon})$ *there exists a neighborhood of the point* $(\hat{D}, \hat{G}, \Gamma, \hat{H}, P_{dc}) = (D^*, 0, H^{-1}, H, P(D^*))$ *such that any solution of the Newton-based ES from the neighborhood exponentially converges to an* $O(\epsilon + \delta + |a|)$*-neighborhood of that point. Furthermore,* $P(D, t)$ *converges to an* $O(\epsilon + \delta + |a|)$*-neighborhood of* $P(D^*)$*.*

4.6 Simulation Results

We present our simulation results in 2 parts. First, we show the validity of the theoretical analysis behind the multivariable gradient-based ES and its improvement over the scalar gradient-based ES for MPPT of a PV system including 2 strings of 3 cascade PV modules. Second, we show that the multivariable Newton-based ES successfully removes dependence of the adaptation process on the cost function shape which raises from the variation of solar irradiance and environmental temperature in PV systems.

Table 4.1: Parameters used in the simulations.

Parameter	Value	Unit	Parameter	Value	Unit
f_s	100	kHz	V_{dc}	300	V
C_i	3	μF	C_o	220	μF
L	220	μH	d_0	0.5	–
K_g	$0.01I_{6\times 6}$	–	k_g	0.01	–
ω	7000	rad/s	a	0.01	–
ω_l	50	rad/s	ω_h	45	rad/s
ω_1	4500	rad/s	ω_4	5500	rad/s
ω_2	6500	rad/s	ω_5	7500	rad/s
ω_3	8500	rad/s	ω_6	9500	rad/s
m	2	–	n	3	–

4.6.1 Multivariable Gradient-Based ES versus Distributed MPPT

To show the effectiveness of the proposed multivariable design in Fig. 4.7, and compare its performance with that of the scalar design in Fig. 4.5, we simulate a PV system with $m = 2$ parallel strings and $n = 3$ cascade modules in each string. The PV modules are model 215N from Sanyo, with datasheet parameters presented in Section 3.3.

Selecting all the frequencies in a narrow range creates large overshoots and steady state errors in parameter estimation. However, choosing the frequencies in a wide range causes very different convergence rates in each channel. Since we set the lowpass filter frequency equal for all the channels, the amplitude of the perturbation signal with the lowest frequency reduces less than that with the highest frequency, which in turn results in a higher feedback gain for the low frequency channel, which derives the parameter faster to the optimal value. It is possible to tune the matrix gain elements with respect to the selected frequencies. What this means is that in order to have the same convergence rate for a wide range of selected frequencies, we can choose a higher gain for higher frequencies to compensate the effect of lowpass filter. We prefer to select the frequencies in a reasonable range, between 50% up and down of the central frequency.The central frequency is small enough in comparison to the PWM frequency. We suggest that this be of the order of 1% of the PWM frequency, $\epsilon <\leq 0.01$. The transient for the estimate of the gradient vector contains frequencies that include harmonics of

$\omega_i - \omega_j$, for all distinct i and j. The bandwidth of the lowpass filter needs to be designed with respect to these values. We suggest selecting ω_l to be of the order of 5% of the least difference between the probing frequencies, $\delta \leq 0.05$. The final step is selecting the cut-off frequency of the highpass filter, which we simply choose to be smaller than or equal to ω_l. Based on the preceding remarks, the numerical values of the design parameters are as presented in Table 4.1.

The temperature $\mathcal{T}$ is assumed to be equal to 25 °C for all modules throughout. The irradiance $\mathcal{S}$ is assumed to be equal to 1000 $\mathrm{W/m^2}$ initially, with a step change to 500 $\mathrm{W/m^2}$ for modules PV_{12} and PV_{23} at $t = 0.5$ s and then back to 1000 $\mathrm{W/m^2}$ at 1 s, so as to simulate partial shading on some modules. The output power of the entire system is shown in Fig. 4.14, with the estimate of the pulse duration for each module shown in Fig. 2.6. It is clear from Fig. 4.14 that the multivariable algorithm performs a uniform and faster transient against step up or step down changes in the generated power.

At the beginning all PV modules and converters have the same settings, gains, and initial conditions. Also all modules are under the same irradiance and temperature. Hence, the transient of the scalar ES for all parameters is the same as shown in Fig. 4.12. On the other hand, multivariable ES shows different transient for each parameter which is happening because of different frequencies of the perturbation function in each channel. The lowest frequency shows the fastest response, along with a correspondingly larger overshoot. It is possible to tune matrix K_g such that all transients look the same.

When the modules in each string are partially shaded, the overall power level decreases. The multivariable ES design recovers from this power level change faster than the scalar version. As clear from Fig. 4.11, the power goes to the MPP in less than half the time needed for the scalar scheme.

The irradiance level of the partially shaded modules is returned to 1000 $\mathrm{W/m^2}$ at $t = 1$ s. At this point both schemes show a similar transient. It is concluded that the convergence rate of the multivariable scheme does not vary largely from step up to step down in power generation, which is not true for the scalar ES. It is clear that in the step down situation the scalar scheme shows a

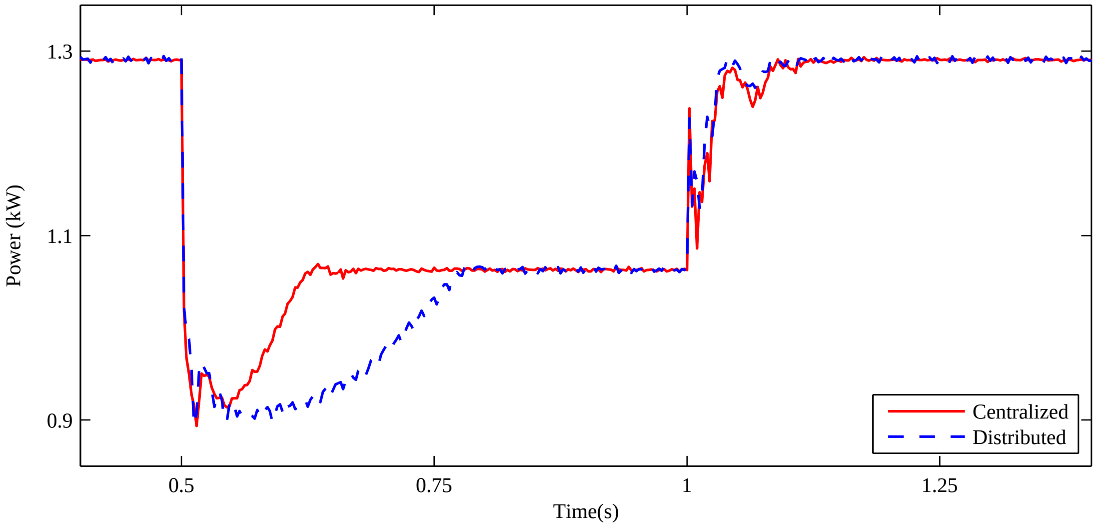

Figure 4.11: Generated power in a partial shading scenario. (solid red) Multivariable gradient-based ES and (dashed blue) distributed ES.

slower performance than the step up case.

4.6.2 Multivariable Newton-Based ES versus Multivariable Gradient-Based ES

To show the effectiveness of the proposed Newton-based design in Fig. 4.10, and compare its performance with that of the gradient-based design in Fig. 4.8, we simulate a PV system with $n = 2$ cascade modules. The PV modules are model 215N from Sanyo, with datasheet parameters presented in Section 3.3. The variation of the generated power of a PV system including two series module from Sanyo connected to a DC bus with $V_{DC} = 200$ V under standard test condition, $\mathcal{S}$=1000 W/m^2 and $\mathcal{T}$=25 °C, is shown in Fig. 4.13. The MPP happens at $D = [\%57\ \%57]^T$.

Parameter selection has an important rule in the performance of the multivariable ES. Selecting all the frequencies in a narrow range creates large overshoots and steady state errors in parameter estimation. However, choosing the frequencies in a wide range causes very different convergence rates in each channel of the gradient-based ES which is not the case in Newton-based method. Since we set

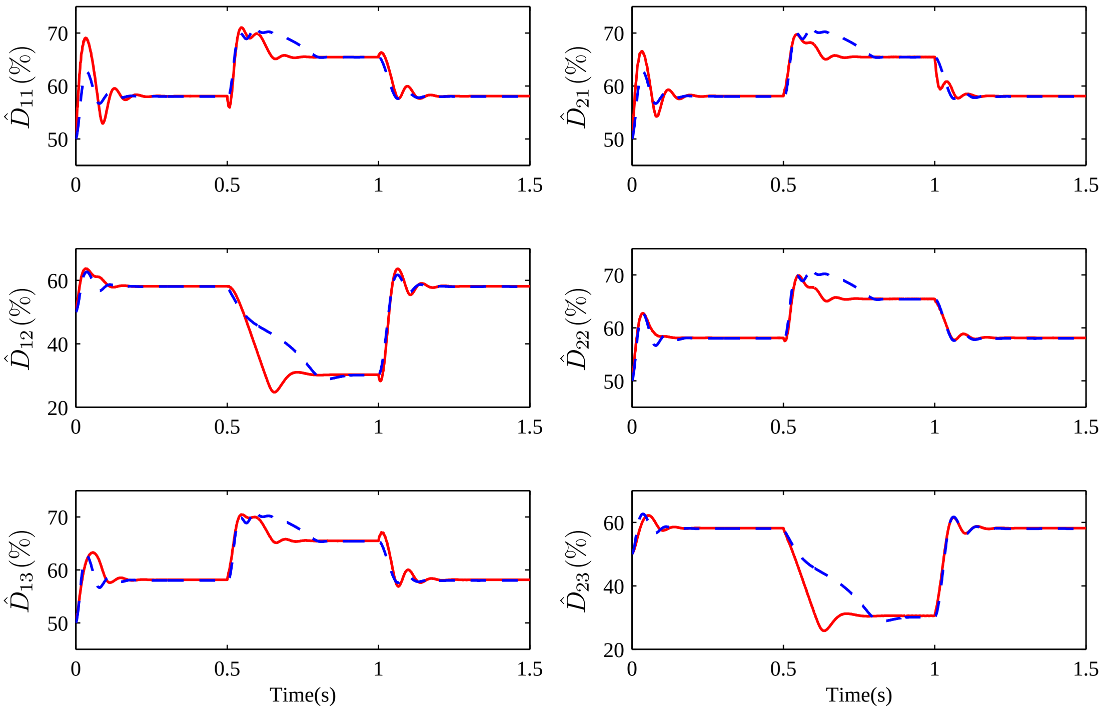

Figure 4.12: Adaptation of the pulse duration. (solid red) Multivariable gradient-based ES and (dashed blue) distributed ES.

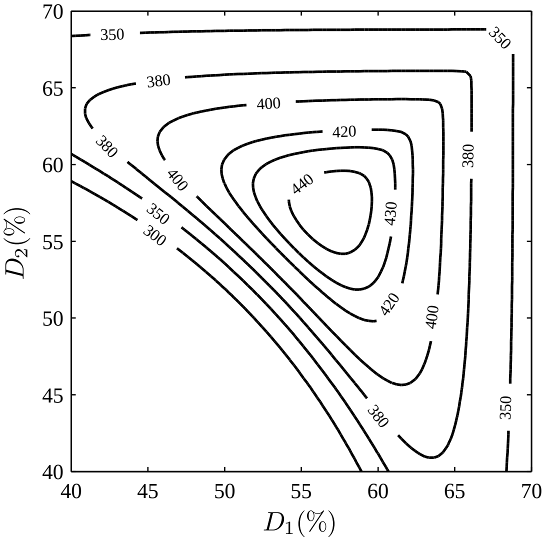

Figure 4.13: Variation of the power of a cascade PV system including two Sanyo PV modules versus pulse duration, $D = [D_1 \ D_2]^T$. Level sets show the power in Watt. $\mathcal{S}_1 = \mathcal{S}_2 = 1000$ W/m^2, $\mathcal{T}_1 = \mathcal{T}_2 = 25$°C, and $V_{dc} = 200$ V.

the lowpass filter frequency equal for all the channels, then in the gradient-based scheme the amplitude of the perturbation signal with the lowest frequency reduces less than that with the highest frequency, which in turn results in a higher feedback gain for the low frequency channel, which derives the parameter faster to the optimal value. It is possible to tune the matrix gain elements with respect to the selected frequencies. This means that in order to have the same convergence rate for a wide range of selected frequencies in gradient method, we can choose a higher gain for higher frequencies to compensate the effect of the lowpass filter.

The Newton-based ES removes the dependence of the convergence rate on the shape of the cost function and the selected frequencies for probing vector. This creates a uniform convergence rate in all channels of the Newton-based scheme. We select the probing frequencies small enough in comparison to the PWM frequency. We suggest that these be of the order of 1–2% of the PWM frequency ,$\epsilon \leq 0.01$). The transient for the estimate of the gradient vector contains frequencies that include harmonics of $\omega_i - \omega_j$, for all distinct i and j. The bandwidth of the lowpass filter needs to be designed with respect to these values. We concluded from (4.39) that the raw estimate of the Hessian, $N(t)P_{ac}$, has harmonics of the order of $1/a$ which should be alleviated dramatically with proper selection of ω_l which reduces the fluctuation in the estimate of the Hessian, $\hat{H}$. We suggest selecting ω_l to be of the order of 5% of the least difference of harmonics in (4.40), $\delta \leq 0.05$. The final step is selecting the cut-off frequency of the highpass filter, which we simply choose to be smaller than ω_l.

Based on the preceding remarks, the numerical values of the design parameters are: $\omega_1 = 5000$ rad/s, $\omega_2 = 6000$ rad/s, $a = 0.01$, $\omega_l = 10$ rad/s, $\omega_h = 7$ rad/s, $H_0 = -10^5 \text{diag}([1\ 1])$, $D_0 = [0.5\ 0.5]^T$, $\beta = 10$, and $K_n = \text{diag}([1\ 1])$. To make a fair comparison between gradient-based algorithm and Newton scheme K_g should be in order of $K_n\Gamma_0$, where $\Gamma_0 = H_0^{-1}$. However, we select $K_g = -30K_n\Gamma_0$ to make the comparison more strict for the Newton algorithm. The temperature T is assumed to be equal to 25 °C for all modules throughout. The irradiance S is assumed to be equal to 1000 W/m^2 initially, with a step change to 400 W/m^2 for modules PV$_2$ at $t = 10$ s and then back to 1000 W/m^2 at 20 s, so as to simulate

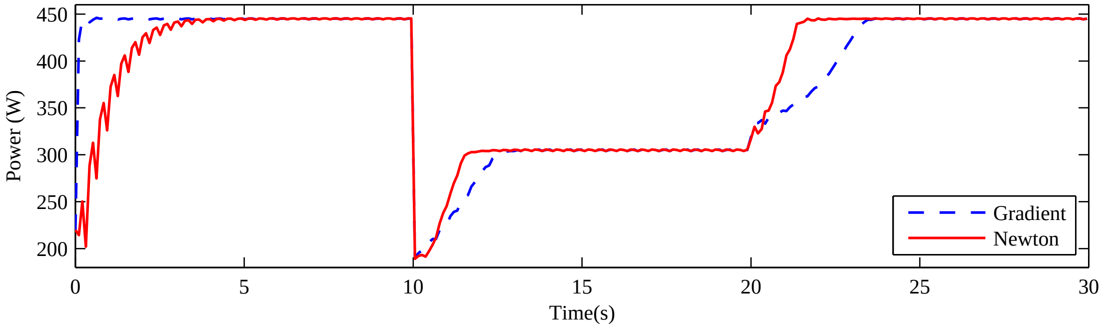

Figure 4.14: Generated power in a partial shading scenario. Newton-based ES governs the system to its MPP with a uniform transient less than 5 s.

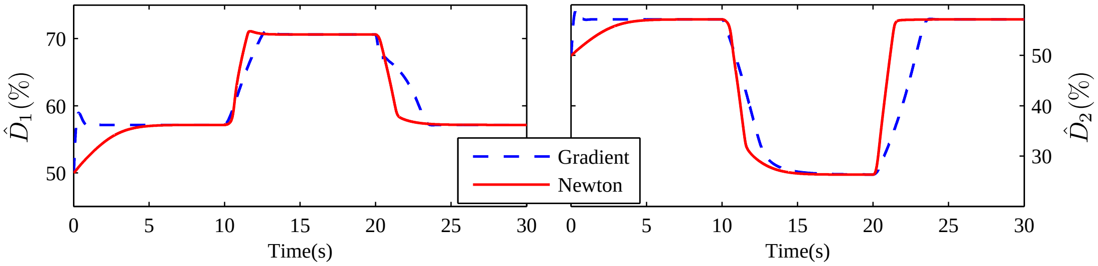

Figure 4.15: Adaptation of the pulse duration. Newton-based ES shows a similar convergence rate for all parameters. The convergence rate of the gradient-based ES varies with power level and direction of its variation.

partial shading. Modulation frequency of PWM is $f_s = 100$ kHz.

Fig. 4.14 shows the output power of the entire system, and the estimates of the pulse duration and Hessian are shown in Fig. 4.15 and Fig. 4.16, respectively. It is clear from Fig. 4.14 that after the initial transient (roughly the first 5 s), the Newton-based algorithm performs a uniform and faster transient against step down (at 10 s) or step up (at 20 s) changes in the generated power. The transient of the gradient ES for all parameters is slightly faster than the Newton at the beginning as shown in Fig. 4.15, resulting in the faster transient performance initially[1]. However, the transient behavior of the Newton-based ES is more uniform in response to sudden changes in power level, while the gradient-based ES has

---

[1] We remind the reader that at the beginning of the adaptation process, the estimate of Γ^{-1} is far from its actual value, which affects the transient convergence rate.

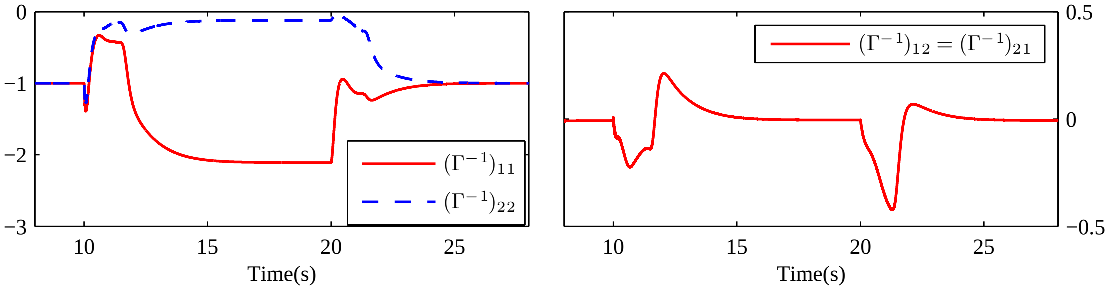

Figure 4.16: Hessian matrix converges to its actual value. The arrays are normalized with respect to $(\Gamma^{-1})_{11}$ at t=9 s.

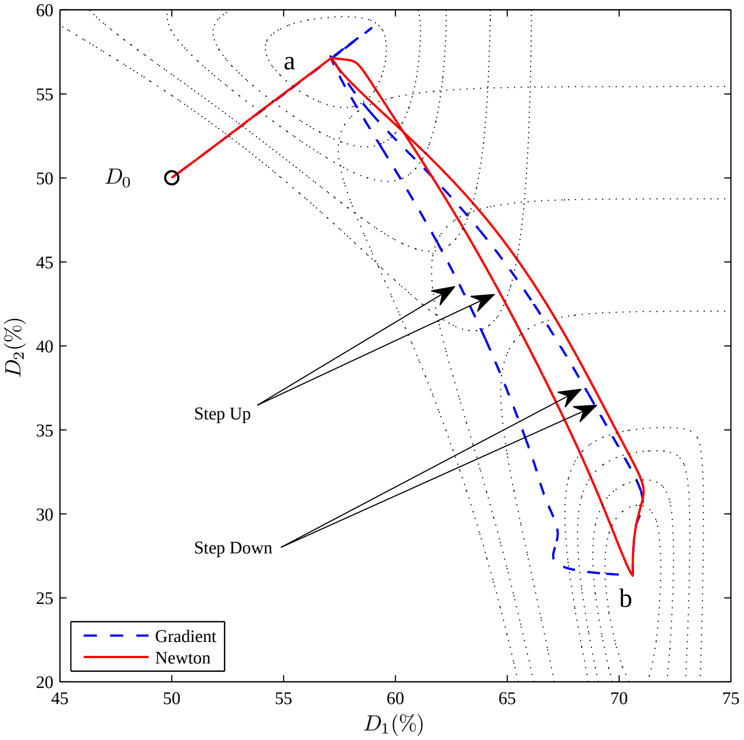

Figure 4.17: Phase-portrait of the adaptation process. (a) MPP before and (b) MPP after changing irradiance. D_0 indicates the initial condition.

different convergence rates for every parameter which varies with the power level. Lastly, as mentioned in Section 4.5, the Newton-based design moves the system in almost a straight line between extrema, in contrast to curved steepest descent trajectories of the gradient algorithm. This observation is demonstrated clearly in Fig. 4.17.

4.7 Experimental results

Our hardware setup consists of 2 cascade PV modules connected to an active load which plays the role of the DC bus with $V_{\mathrm{dc}} = 5\mathrm{V}$, as shown in Fig 4.21. The PV modules are custom-made including 12 PV cells shown in Fig. 4.18, with P-V and I-V characteristics shown in Fig. 4.19. We use dSPACE Control Desk Next Generation software and the DS1104 R&D Controller Board to implement our MPPT algorithms inside Simulink and interact with the DC/DC converters through Connector Panel CP1104. Also we use the "Power-Pole Boards" developed by the University of Minnesota for educational purposes shown in Fig. 4.20, that are general purpose DC/DC converter boards, configured as a DC/DC buck converter, with external PWM signals generated by the DS1104. Each Power-pole board has a current sensor LA 25-NP to measure the inductor current which we use along with the capacitor ripple current measurement to calculate the DC bus current. We employ the DC bus current and DC bus voltage to measure the power supplied to the DC bus. The hardware setup is shown in Fig. 4.22. The numerical values of the parameters are as follows: $\omega = 100\pi$ rad/s, $\omega_1 = 0.9\omega,\ \omega_2 = \omega, \omega_l = \omega_h = \omega/20, k_g = 2.5 \times 10^{-3}, K_g = k_g I_{2\times 2}, K_n = 0.08 I_{2\times 2}, H_0 = -400 I_{2\times 2}, a = 0.05$, and $D_0 = [\%70 \ \ \%70]^T$. Also we use high order Bessel filters instead of the first order lowpass and highpass filters to separate the AC and DC parts of the power signals and to create a smooth estimate of the gradient vector and the Hessain matrix. The PWM frequency is 100 kHz and the sampling time of the MPPT algorithm is 0.3 ms. The temperature of PV modules is 25°C and the modules are fully exposed to the sun from time 0–60 s and from 120–180 s. To simulate the effect of partial shading, PV_1 is covered with a plastic mat from time 60–120 s.

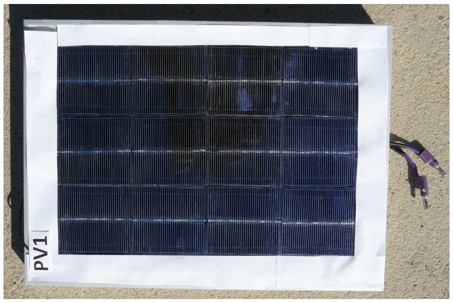

Figure 4.18: Custom-made PV module.

When one module is partially shaded, the overall power level decreases. As clear from Fig. 4.23, the Newton algorithm recovers from this power level change faster than the other 2 algorithms. While the Newton method has the least steady-state error and uniform response under step down and step up power scenarios, the distributed method has the highest steady-state error and large response time in face of power decrease. The multivariable gradient-based ES performs better than the distributed MPPT under partial shading conditions. Furthermore, Fig. 4.24 shows that the adaptation process of the pulse duration in the Newton method is uniform and faster than the 2 other designs.

The irradiance level of the partially shaded module is returned to normal level at $t = 120$ s. At this point the Newton scheme show faster transient in comparison to the similar transient of the multivariable gradient-based ES and the distributed ES. It is concluded that the convergence rate of the Newton scheme does not vary largely from step up to step down in power generation, which is not true for the gradient-based and distributed MPPT schemes. It is clear that in the step down situation the distributed scheme shows a slower performance than the step up case. As expected, the experimental results are in keeping with the analytical and simulation results. The estimate of the Hessian is shown in Fig. 4.26. The MPPT process is depicted in Fig. 4.25 which shows a large steady-state error for the distributed scheme.

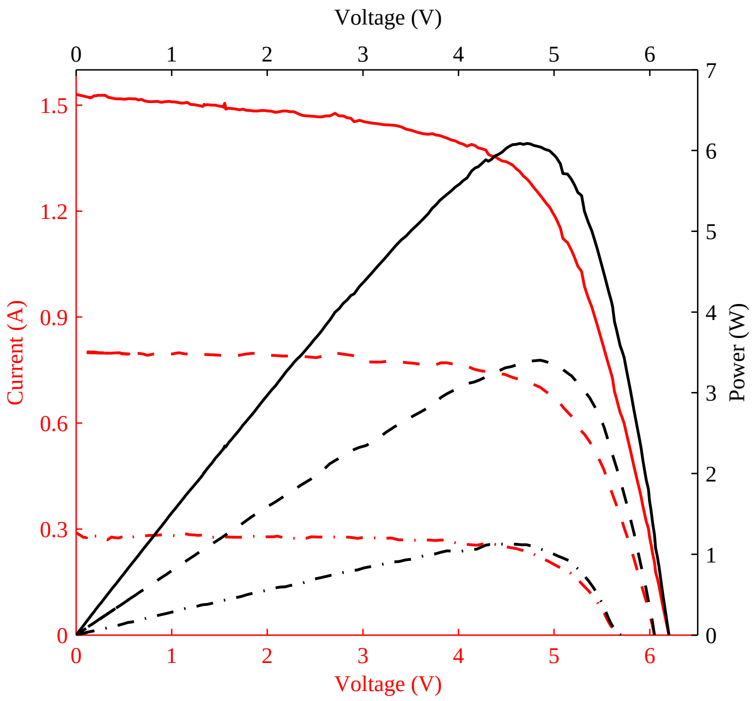

Figure 4.19: Power and current maps of the custom-made PV modules used in the experiments for $\mathcal{T} = 25°$ C. (solid line) $\mathcal{S} = 1000$ W/m^2, (dashed) $\mathcal{S} = 520$ W/m^2, and (dash-dot) $\mathcal{S} = 190$ W/m^2.

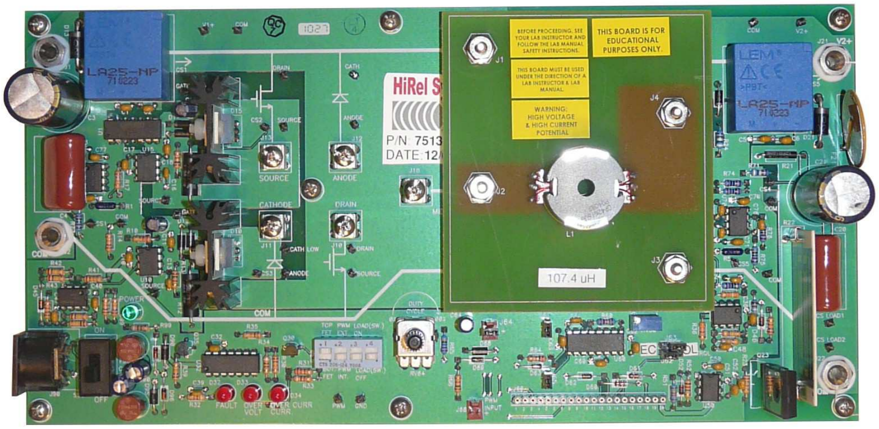

Figure 4.20: "Power-Pole Board" developed by the University of Minnesota for educational purposes. We configure it as a DC/DC buck converter in our experiments.

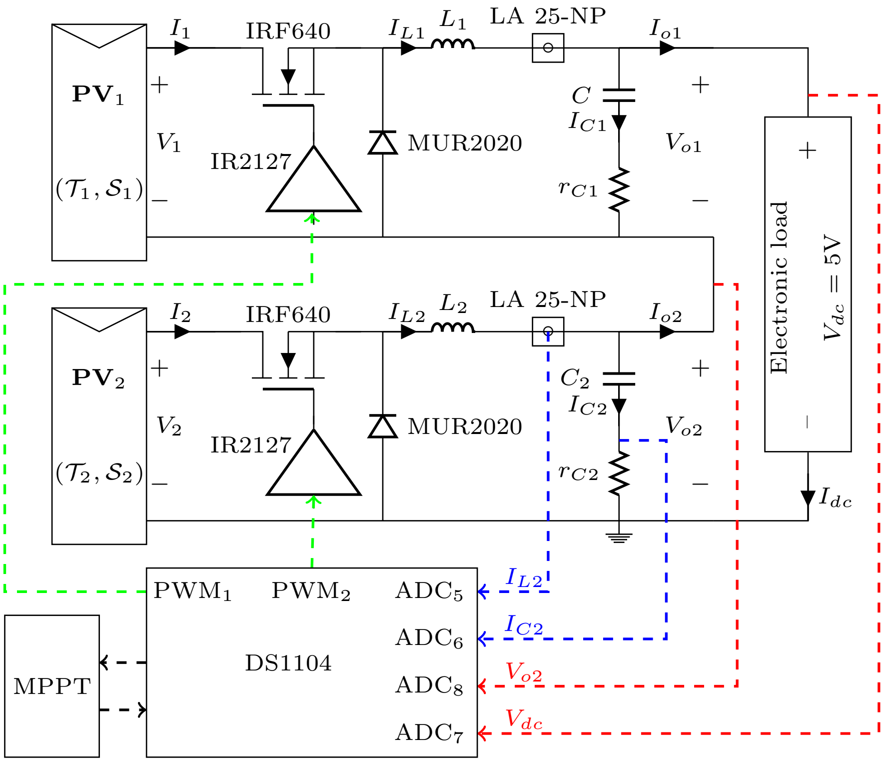

Figure 4.21: Schematic of the hardware setup.

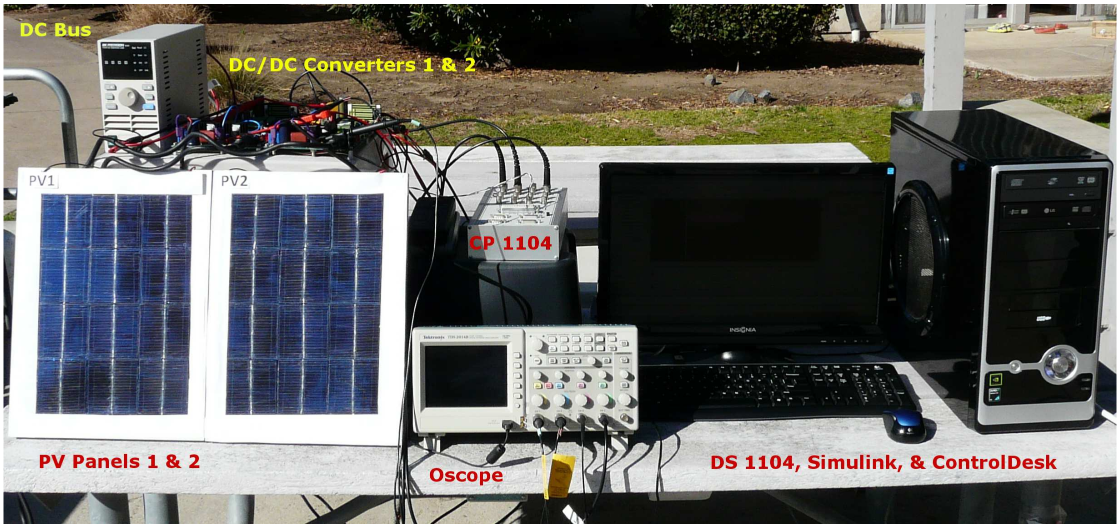

Figure 4.22: Experimental setup

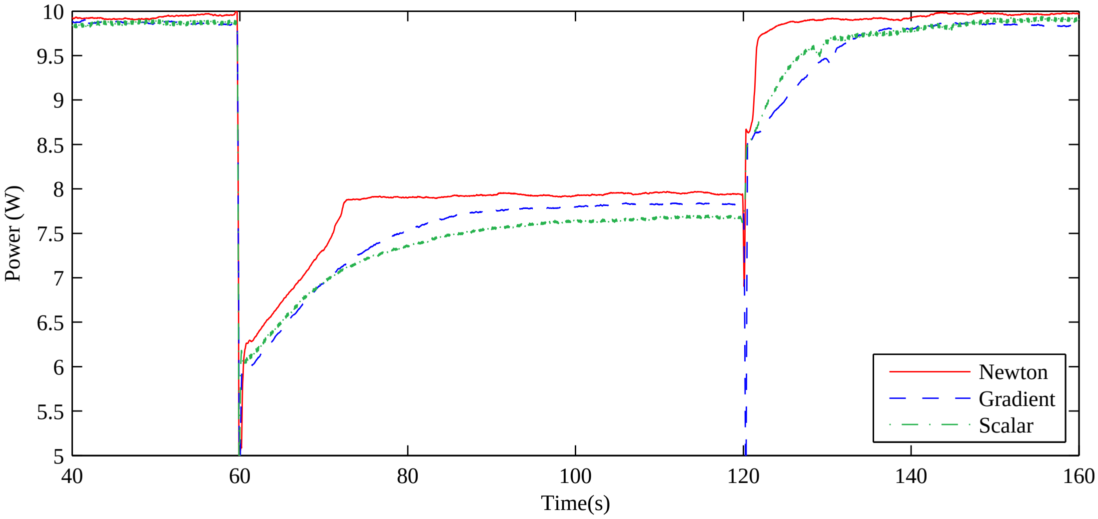

Figure 4.23: Variation of power versus time. The Newton algorithm shows uniform and fast transient with low steady-state error.

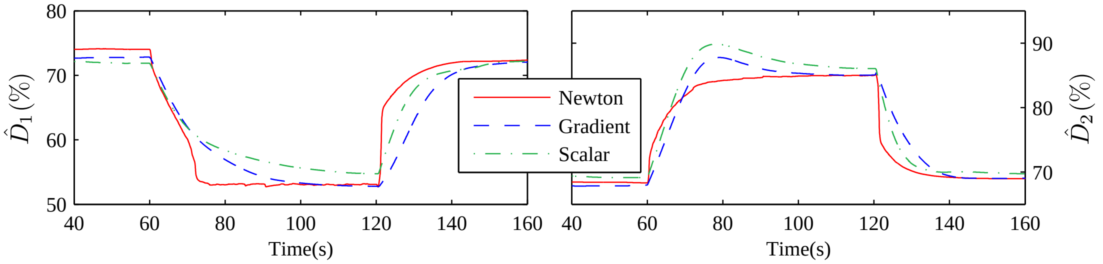

Figure 4.24: Variation of duty cycle versus time. The distributed MPPT shows the slowest transient.

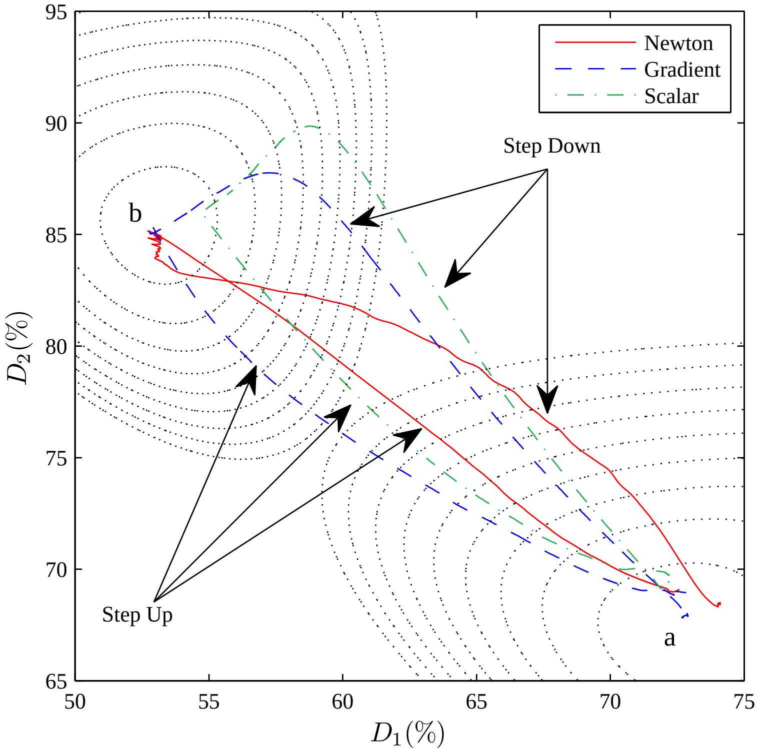

Figure 4.25: Phase portrait of the MPPT for Newton, gradient, and distributed algorithms. Region (a) shows MPP area for full exposure to the sun and region (b) shows the MPP area when PV_1 is partially shaded.

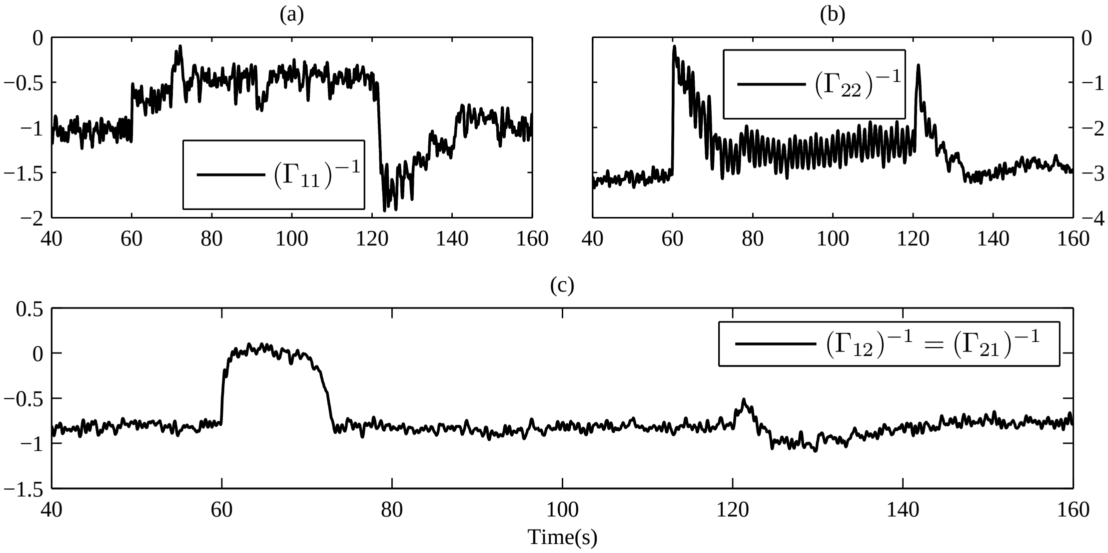

Figure 4.26: The estimate of the Hessian for Newton-based ES. The arrays are normalized with respect to $(\Gamma^{-1})_{11}$ at t=40 s.

4.8 Conclusions

Using extremum seeking in a micro-converter configuration is a promising way to extract maximum power from a PV system. Conventionally used scalar gradient-based designs do so based on the generated power of each module. On the one hand, this requires two sensors per module, and on the other, the dependence on the level and direction of changes of the individual powers causes different transients in the parameter updates, particularly in response to sudden irradiance changes caused by partial shading. The multivariable gradient-based ES design removes some of these drawbacks. However, it still depends on the shape and curvature of the cost function. Since the Hessian of the entire system (and not individual modules) defines the performance of the parameter update, we can use the estimate of the Hessian to eliminate the dependence of the ES algorithm on environmental conditions that the Hessian depends upon. The Newton-based algorithm that we have presented does so, resulting in more uniform transients in response to irradiance and temperature changes, and improved overall performance. The scheme also only uses two sensors for the overall system, resulting in lower hardware cost. The dual advantages contribute towards reduced average cost/watt, enhancing the economic viability of solar.

This chapter contains material from A. Ghaffari, M. Krstić, and S. Seshagiri, “Power Optimization for Photovoltaic Micro-Converters using Multivariable Newton-Based Extremum-Seeking,” in *Proc. of IEEE Conference on Decision and Control*, 2012 and A. Ghaffari, S. Seshagiri, and M. Krstić, “Power Optimization for Photovoltaic Micro-Converters using Multivariable Gradient-Based Extremum-Seeking,” Submitted to the *IEEE Transactions on Industrial Electronics.* Of which the dissertation author was the primary author.

Chapter 5

Power Optimization and Control in Wind Energy Conversion Systems using Extremum Seeking

Wind turbines (WTs) are a promising source of sustainable power which bring different technologies together to harness the vast wind energy resources close to the ground. The generated power by a WT is a function of the rotor shaft speed and the blade pitch angle. During the low to medium wind speeds, below the rated speed, the blade pitch angle is set to zero and the rotor shaft speed is manipulated to achieve the peak power. When wind speed increases beyond the rated wind speed the variable speed control algorithm is replaced by a variable pitch control algorithm—the rotor shaft speed is fixed and the blade pitch angle is controlled to limit the WT power to its rated level. In this chapter we focus on the sub-rated region and we develop a variable speed control technique using the ES for MPPT of the WT. Also, we present a nonlinear control based on the idea of Field-Oriented Control (FOC) to achieve desired transient and to prevent magnetic saturation of the Induction Generator (IG) stator.

5.1 Introduction

A variable speed wind turbine generates power in two different regions, sub-rated power region and rated power region. In the sub-rated power region, the maximum achievable mechanical power of a WT is a function of its shaft speed at any given wind velocity. To achieve Maximum Power Point Tracking (MPPT), i.e., extract maximum power, an optimization algorithm is needed [9, 13, 36, 39, 43, 46, 59, 60, 67], and is often used in conjunction with a controller that guarantees other closed-loop desired performance specifications. In our current work, we focus on the optimization and control of a Wind Energy Conversion System (WECS) composed of a WT, a squirrel-cage induction generator, and a Matrix Converter (MC). The matrix converter, which is a replacement for the conventional rectifier-inverter combination (AC-DC-AC), features no energy storage components, has bidirectional power flow capability and controllable input power factor [82]. It connects the IG to the power grid, and along with the presented control/optimization design, steers the WT to its Maximum Power Point (MPP) by controlling the electrical frequency and voltage amplitude of the stator of IG, which in turn leads to a speed variation in the turbine shaft. It also assists in voltage regulation or power factor correction by controlling the reactive power transfer to the grid.

A design for a system similar to the one we consider here has been presented in [9], and is based on a standard Perturb and Observe (P&O) algorithm. The P&O algorithm uses look-up table values that are dependent on the system model and parameter values. Furthermore, the control design employs Jacobian linearization, and uncertainty in the system dynamics and/or variations in the working conditions cause the system to move away from its MPP. Another method based on fuzzy logic principles and four-leg-improved MC model, used for performance enhancement and efficiency optimization, is presented in [46], and is also highly model-dependent. Model-dependent designs have the drawback that the optimization algorithm and controller need to be redesigned carefully for each WECS. To overcome these difficulties we present an extremum seeking (ES) algorithm, which is (i) non-model-based, and (ii) is easily tunable [6, 7, 45, 70–73]. Furthermore, ES shows promising results for a wide variety of applications [10, 17, 31, 42, 51, 77]. ES designs for MPPT of WECS are also presented in [13, 43, 59], but differ from the design in this paper in several respects, including assumptions on the system model, transient performance, and performance robustness.

With the exception of [9], none of the previous works on the power extraction have focused on the transient performance, and the model in [9], unlike ours, is based on linearization and is highly model dependent and non-robust to modeling errors. While the ES design we present alleviates this problem, a requirement for the design is that its dynamics be slower than that of the WECS. While the WECS system is stable by itself, its linearization has "slow poles", which consequently limits the convergence rate for the ES algorithm. To improve the transient response, we propose an inner-loop inductor generator control based on FOC, the elements of which can be found in [49] and [52]. The inner-loop control we present is robust to machine parameters; and while based on feedback linearization, can easily be modified to robustify performance to machine parameter variations. Its role in this work is limited to emphasizing the effect on the convergence of the ES, and is not the particular focus of this paper. For the ES design, the shaft speed of the WT is considered as the variable parameter to tune MPP. The generated mechanical power is the cost function for the ES algorithm, and electrical frequency and voltage amplitude of the stator of IG are controlled through the MC to reach desired closed-loop performance. As a result of including the inner-loop, overall design has faster response time, with other benefits such as avoidance of magnetic saturation. In comparison to model-based designs, ES better handles model uncertainty in the turbine power map, resulting in improved power extraction. To the best of our knowledge, this is the first work in the literature that combines the MPPT with nonlinear control design that has good performance robustness to uncertainty, and faster transient performance, allowing for power tracking under rapidly varying wind conditions.

The rest of this chapter is organized as follows: An introduction to modeling of the WECS with concentration on the squirrel-cage IG dynamics in stationary reference frame and the MC is discussed in Section 5.2. We explain the conven-

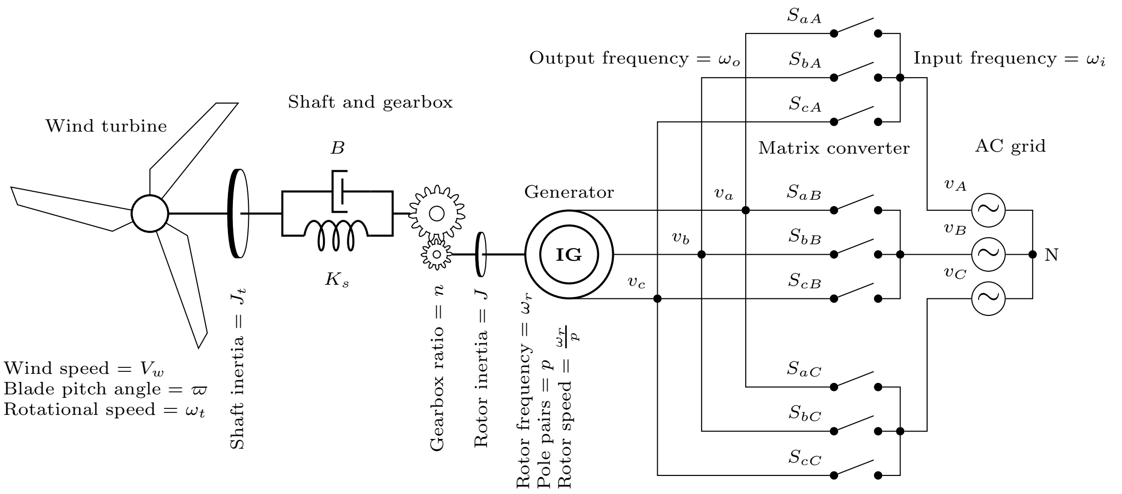

Figure 5.1: WECS including WT, gear box, IG, and MC.

tional direct FOC in Section 5.3. Our nonlinear controller design is discussed in Section 5.4, and the ES algorithm in Section 5.5. Simulation results to verify the effectiveness of the proposed scheme are presented in Section 5.6, and our conclusions are presented in Section 5.7.

5.2 Wind Energy Conversion System

A schematic of a WECS including WT, IG, and MC is shown in Fig. 5.1. Wind turbines work in four different regions as depicted in Fig. 5.2. In Region I, the wind speed is too low for the turbine to generate power. Region II, also called the sub-rated power region, lies between the cut-in speed and rated speed. Here the generator operates at below rated power. The theoretical shape of this curve reflects the basic law of power production, where power is proportional to the cube of the wind speed. In Region III, the power output is limited by the turbine; this occurs when the wind is sufficient for the turbine to reach its rated output power. Region IV is the period of stronger winds, where the power in the wind is so great that it could be detrimental to the turbine, so the turbine shuts down [37].

The wind power available on the blade impact area is defined as

$$P_w = \frac{1}{2}\rho A V_w^3, \quad A = \pi R^2, \tag{5.1}$$

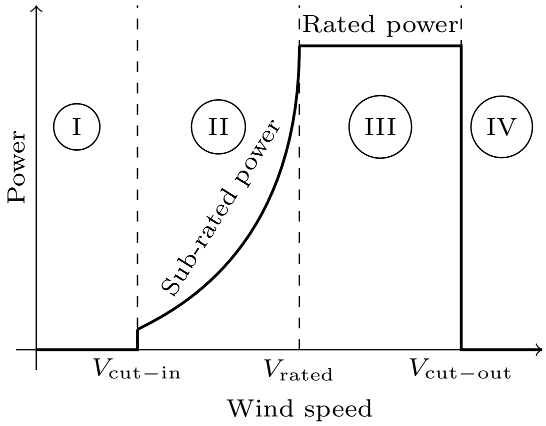

Figure 5.2: Typical power curve of WT including four operating regions.

where R is the blade length and V_w is wind speed. The mechanical power generated by the WT is expressed as

$$P_t = \omega_t T_t = C_p(V_w, \varpi, \omega_t)P_w, \tag{5.2}$$

where T_t is the rotor torque, ω_t is the shaft speed of the WT, and C_p is the non-dimensional power coefficient, which is a measure of the ratio of the rotor power to the wind power. The power coefficient is a function of wind speed, WT shaft speed, and the blade pitch angle, ϖ. The theoretical limit for C_p is 0.59 according to Betz's law, but its practical range of variation is 0.2–0.4 [46]. The power coefficient has been approximated numerically in several references, e.g., [4] and [69]. One of the most common equations used for power coefficient is

$$C_p(V_w, \varpi, \omega_t) = \frac{0.73}{e^{18.4\varsigma}}\left(151\varsigma - \frac{29\varpi}{50} - \frac{\varpi^{2.14}}{500} - 13.2\right), \tag{5.3}$$

where $\varsigma = 1/(\varrho - 0.02\varpi) - 0.003/(\varpi^3 + 1)$ and

$$\varrho = \frac{\omega_t R}{V_w} \tag{5.4}$$

is tip-speed-ratio. Variable pitch control algorithms govern the blade pitch angle in the Region III to maintain the generated power at the rated level when wind speed is higher than rated speed and less than cut-out speed as shown in Fig. 5.2. Since a non-zero blade pitch angle reduces the peak power of the WT, and MPPT

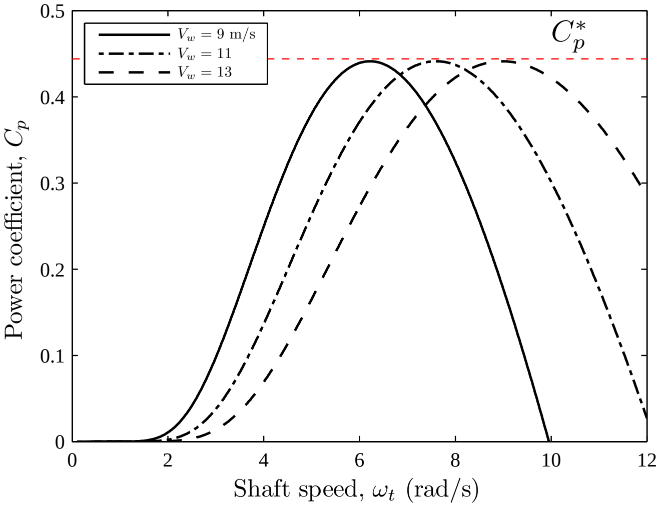

Figure 5.3: Variation of power coefficient versus turbine shaft speed for different wind speeds where $\varpi = 0$. The maximum value of the power coefficient is C_p^*.

in Region II is our main control objective, then in this study we assume $\varpi = 0$ which results in

$$C_p(V_w, \omega_t) = 0.73 \frac{151 \frac{V_w}{R\omega_t} - 13.635}{\exp\left(\frac{V_w}{R\omega_t} - 0.003\right)}. \tag{5.5}$$

Power coefficient (5.5) depends on the WT shaft speed which can be used for power control and optimization. Wind speed plays the role of a disturbance input and affects the generated power by the WT. The MPPT algorithm in sub-rated power region should be able to govern the WT to its peak power regardless of the variations of the wind speed. As shown in Fig. 5.3 the maximum value of the power coefficient happens at different shaft speeds when wind speed is varying, but the maximum value stays at the same level of C_p^*. For future analysis we assume that the power coefficient and wind speed function satisfy following assumption.

Assumption 4 *The power coefficient $C_p(\omega_t, V_w)$ and wind speed function $V_w(t)$ are bounded C^3 functions with bounded derivatives.*

From (5.2) and (5.5), and considering the fact that the blade pitch angle is

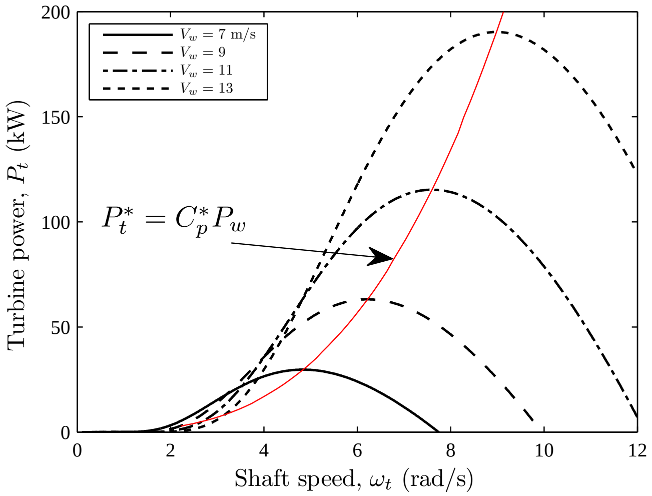

Figure 5.4: Variation of mechanical power captured by WT versus turbine shaft speed for different wind speeds where $\varpi = 0$. The MPP moves on $C_p^* P_w$ curve which shows the characteristic of the sub-rated region of WECS.

zero, we have

$$P_t(V_w, \omega_t) = 55.115\rho A \frac{\frac{V_w}{R\omega_t} - 0.09}{\exp\left(\frac{V_w}{R\omega_t} - 0.003\right)} V_w^3, \tag{5.6}$$

which shows that the power captured by the WT is defined by the wind speed, V_w, and the shaft speed of the WT. However, the wind speed is a disturbance input and we can manipulate the shaft speed to govern the mechanical power to its maximum value in sub-rated region. The variation of mechanical power versus turbine shaft speed is shown in Fig. 5.4 for different wind speeds. It is clear that under a constant wind speed the relevant power curve has a unique maximum which is defined by a specific shaft speed. Also the maximum point moves on a third order curve which defines the maximum mechanical power captured by the WT.

Assumption 5 *The following holds for the WT mechanical power around its peak* *point for every wind speed (see Fig. 5.4)*

$$\frac{\partial P_t(V_w,\omega_t)}{\partial \omega_t}(\omega_t^*) \;=\; 0 \tag{5.7}$$

$$\frac{\partial^2 P_t(V_w,\omega_t)}{\partial \omega_t^2}(\omega_t^*) \;<\; 0. \tag{5.8}$$

As shown in Fig. 5.1 the WT shaft is modeled as a spring-damper. The dynamic equations of the turbine, the shaft, and the gearbox are

$$\frac{\mathrm{d}}{\mathrm{d}t}\tilde{\theta} \;=\; \omega_t - \frac{\omega_r}{pn}, \qquad \tilde{\theta} = \theta_t - \frac{\theta_r}{pn} \tag{5.9}$$

$$\frac{\mathrm{d}}{\mathrm{d}t}\omega_t \;=\; \frac{1}{J_t}\left(-T_t - T_L\right), \quad T_t = \frac{P_t(V_w,\omega_t)}{\omega_t}, \tag{5.10}$$

where ω_r is the angular electrical frequency of the rotor of IG, θ_t is wind turbine angular position, θ_r is the electrical angle of the rotor of IG, p is the number of pole pairs of the IG, n is the gearbox ratio, T_t is the turbine torque generated by mechanical power, T_L is the load torque created by the spring-damper model of the the shaft

$$T_L = K_s\tilde{\theta} + B\left(\omega_t - \frac{\omega_r}{pn}\right), \tag{5.11}$$

where K_s is the stiffness coefficient of the spring and B is the damping ratio. The generator rotor angular speed equals ω_r/p. The numerical values of the parameters are given in Table 5.1.

Squirrel-cage IG's are relatively inexpensive, robust, and require little maintenance. When operated using vector control techniques, fast dynamic response, and accurate torque control is obtained [16]. From [44], the (α,β) model equations for the squirrel-cage IG are as follows:

$$\frac{\mathrm{d}}{\mathrm{d}t}i_\alpha = -a_0 i_\alpha + a_1\lambda_\alpha - a_2\omega_r\lambda_\beta + \frac{v_\alpha}{\sigma L_s} \tag{5.12}$$

$$\frac{\mathrm{d}}{\mathrm{d}t}i_\beta = -a_0 i_\beta + a_2\omega_r\lambda_\alpha + a_1\lambda_\beta + \frac{v_\beta}{\sigma L_s} \tag{5.13}$$

$$\frac{\mathrm{d}}{\mathrm{d}t}\lambda_\alpha = a_3 i_\alpha - a_4\lambda_\alpha + \omega_r\lambda_\beta \tag{5.14}$$

$$\frac{\mathrm{d}}{\mathrm{d}t}\lambda_\beta = a_3 i_\beta - a_4\lambda_\beta - \omega_r\lambda_\alpha \tag{5.15}$$

$$\frac{\mathrm{d}}{\mathrm{d}t}\omega_r = \frac{p}{J}\left(T_e - \frac{T_L}{n}\right), \tag{5.16}$$

Table 5.1: Definitions of parameters and their numerical values.

Parameter	Definition	Value	Unit
R	Blade length	10	m
β	Blade pitch angle	0	rad
A	Blade impact area	πR^2	m^2
V_w	Wind speed	–	m/s
ρ	Air density	1.25	kg/m^3
J_t	Rotor inertia of WT	100	Kgm^2
ω_t	Rotational speed of WT	–	rad/s
θ_t	Shaft angel of WT	–	rad
n	Gear box ratio	20	–
K_s	Stiffness coefficient	2×10^6	Nm/rad
B	Damping coefficient	5×10^5	Nm/rad/s
p	Number of pole pairs of SCIG	2	–
L_{ls}	Stator leakage inductance	3.2	mH
L_{lr}	Rotor leakage inductance	3.2	mH
L_m	Magnetizing inductance	143.36	mH
J	Moment of inertia of SCIG	11.06	Kgm^2
R_s	Stator resistance	0.262	Ω
R_r	Rotor resistance	0.187	Ω
ω_r	Rotor electrical frequency	–	rad/s
ω_o	Stator electrical frequency	–	rad/s
V_{im}	Input voltage peak amplitude	1880	V

Table 5.2: Constant Parameters

a_0	$a_2a_3 + R_s/(\sigma L_s)$	b_0	$a_5a_9/(pn)$
a_1	a_2a_4	b_1	$a_8/a_9 + a_7/(pn) - a_9$
a_2	$L_m/(\sigma L_s L_r)$	b_2	a_8^2/a_9
a_3	$L_m R_r/L_r$	b_3	$a_8/a_9 + a_7/(pn)$
a_4	R_r/L_r	b_4	$b_1 - a_0 - a_4$
a_5	$3p^2L_m/(2JL_r)$	b_5	$a_0b_1 + a_4b_1 - b_2/a_9$
a_6	$pK_s/(Jn)$	b_6	$a_0b_2 + a_4b_2 - a_8b_2/a_9$
a_7	$pB/(Jn)$	b_7	$a_2b_0 + a_4b_0/a_3$
a_8	K_s/J_t	b_8	$b_0/(2a_3)$
a_9	B/J_t	b_9	$a_0b_3 + a_4b_3 - b_2/a_9$
c_0	$a_9 - c_3$	b_{10}	$b_3 - a_0 - a_4$
c_1	$K_s^2/(BJ_t)$	b_{11}	$a_0 + 3a_4$
c_2	$a_5B/(npJ_t)$	b_{12}	$2a_1a_3 - 2a_0a_4 - 2a_4^2$
c_3	$K_s/B + B/(n^2J)$	b_{13}	$2a_3/b_0$

where i_α and i_β are stator currents, λ_α and λ_β are rotor flux linkages, v_α and v_β are stator voltages, and the electromagnetic torque generated by the IG is

$$T_e = \frac{3}{2} p \frac{L_m}{L_r} \left(i_\alpha \lambda_\beta - i_\beta \lambda_\alpha \right), \tag{5.17}$$

where L_m is the mutual inductance, $L_s = L_{ls} + L_m$ is stator inductance, $L_r = L_{lr} + L_m$ is rotor inductance, and $\sigma = 1 - L_m^2 / \left(L_r L_s \right)$. The numerical values of the parameters are defined in Table 5.1 and 5.2. Furthermore, the generated active and reactive power can be expressed as follows

$$P_e = \frac{3}{2} \left(v_\alpha i_\alpha + v_\beta i_\beta \right) \tag{5.18}$$

$$Q_e = \frac{3}{2} \left(v_\alpha i_\beta - v_\beta i_\alpha \right). \tag{5.19}$$

As shown in Fig. 5.1 the generator is connected to the AC grid through a MC which includes 9 bidirectional switches operating in 27 different combinations. Matrix converters provide bidirectional power flow, sinusoidal input/output currents, and controllable input power factor. Due to the absence of components with significant wear out characteristics (such as electrolytic capacitors), MC can potentially be very robust and reliable. The amount of space saved by an MC, when compared to a conventional back-to-back converter, has been estimated as a factor of three. Therefore, due to its small size, in some applications, the MC can be embedded in the machine.

Furthermore, there is no intrinsic limitation to the power rating of an MC [16]. Consequently, we use MCs instead of conventional back-to-back converters. The model for MCs that we use is based on [8,33,78]. The input phase voltage of MC, which is connected to the AC grid, is given by

$$v_i = V_{im} \left[\cos\theta_i \;\; \cos\left(\theta_i - \frac{2\pi}{3} \right) \;\; \cos\left(\theta_i + \frac{2\pi}{3} \right) \right]^T, \tag{5.20}$$

where V_{im} is the peak value of the input voltage amplitude and

$$\theta_i = \int_0^t \omega_i \mathrm{d}\tau \tag{5.21}$$

is the input electrical angle where $\omega_i = 2\pi f_i$ is the input electrical frequency of the MC. In this case, due to the inductive nature of the IG, the output phase current can be assumed sinusoidal, and hence given by

$$i_o = I_{om} \begin{bmatrix} \cos\left(\theta_o + \phi_o\right) \\ \cos\left(\theta_o + \phi_o - \frac{2\pi}{3}\right) \\ \cos\left(\theta_o + \phi_o + \frac{2\pi}{3}\right) \end{bmatrix}, \tag{5.22}$$

where I_{om} is the peak value of the output current amplitude, ϕ_o is the load displacement angle at the output frequency $\omega_o = 2\pi f_o$, and

$$\theta_o = \int_0^t \omega_o \mathrm{d}\tau \tag{5.23}$$

is the output electrical angle.

It is desired that the local-averaged output phase voltage (the stator voltage of IG), and the local-averaged input phase current (the AC grid current) be sinusoidal

$$\bar{v}_o = V_{om} \left[\cos\theta_o \ \cos\left(\theta_o + \frac{2\pi}{3}\right) \ \cos\left(\theta_o + \frac{2\pi}{3}\right)\right]^T, \tag{5.24}$$

$$\bar{i}_i = I_{im} \begin{bmatrix} \cos\left(\theta_i + \phi_i\right) \\ \cos\left(\theta_i + \phi_i - \frac{2\pi}{3}\right) \\ \cos\left(\theta_i + \phi_i + \frac{2\pi}{3}\right) \end{bmatrix}, \tag{5.25}$$

where ϕ_i is the input displacement angle which controls the power factor at the grid connection. We are interested in finding modulation matrices such that

$$\bar{v}_o = S \times v_i \tag{5.26}$$

$$\bar{i}_i = S^T \times i_o. \tag{5.27}$$

The solutions to the modulation problem should satisfy: (1) restrictions on the duty cycle of the MC switches that prevent short circuit of the input sources and open-circuit of the inductive load, (2) sinusoidal output voltages with controllable frequency and magnitude, (3) sinusoidal input currents, and (4) desired input displacement power factor [8]. There are two basic solutions which satisfy (1)–(3)

$$S_1 = \frac{1}{3}\begin{bmatrix} 1 & 1 & 1 \\ 1 & 1 & 1 \\ 1 & 1 & 1 \end{bmatrix} + \frac{2}{3}mT_1 \tag{5.28}$$

$$S_2 = \frac{1}{3}\begin{bmatrix} 1 & 1 & 1 \\ 1 & 1 & 1 \\ 1 & 1 & 1 \end{bmatrix} + \frac{2}{3}mT_2 \tag{5.29}$$

where

$$m = \frac{V_{om}}{V_{im}}, \qquad 0 \le m \le \frac{\sqrt{3}}{2} \tag{5.30}$$

is the MC output-to-input voltage gain and

$$T_1 = \begin{bmatrix} \cos\theta_1 & \cos\left(\theta_1 - \frac{2\pi}{3}\right) & \cos\left(\theta_1 + \frac{2\pi}{3}\right) \\ \cos\left(\theta_1 + \frac{2\pi}{3}\right) & \cos\theta_1 & \cos\left(\theta_1 - \frac{2\pi}{3}\right) \\ \cos\left(\theta_1 - \frac{2\pi}{3}\right) & \cos\left(\theta_1 + \frac{2\pi}{3}\right) & \cos\theta_1 \end{bmatrix} \tag{5.31}$$

$$T_2 = \begin{bmatrix} \cos\theta_2 & \cos\left(\theta_2 - \frac{2\pi}{3}\right) & \cos\left(\theta_2 + \frac{2\pi}{3}\right) \\ \cos\left(\theta_2 - \frac{2\pi}{3}\right) & \cos\left(\theta_2 + \frac{2\pi}{3}\right) & \cos\theta_2 \\ \cos\left(\theta_2 + \frac{2\pi}{3}\right) & \cos\theta_2 & \cos\left(\theta_2 - \frac{2\pi}{3}\right) \end{bmatrix}, \tag{5.32}$$

where $\theta_1 = \theta_i - \theta_o$ and $\theta_2 = \theta_i + \theta_o$. The solution in (5.28) yields $\phi_i = \phi_o$, giving the same phase displacement at the input and output ports, whereas the solution in (5.29) yields $\phi_i = -\phi_o$, giving reversed phase displacement. Combining the two solutions provides the means for input displacement factor control [8, 78]

$$S = c \times S_1 + (1 - c) \times S_2, \qquad 0 \le c \le 1, \tag{5.33}$$

where c controls the power factor at the grid side. Reactive power control is not the focus of this research, so we simply set $c = 0.5$ to obtain unity displacement power factor at the MC input terminals. However, this does not result in a unity displacement power factor at input source terminals.

Considering zero losses in MC, the input and output powers are equal and related as follows:

$$P_i \equiv \tfrac{3}{2}V_{im}I_{im}\cos\phi_i \tag{5.34}$$

$$P_o \equiv \tfrac{3}{2}V_{om}I_{om}\cos\phi_o. \tag{5.35}$$

From (5.30) and equating (5.34) and (5.35) we have

$$I_{im} = m\frac{\cos\phi_o}{\cos\phi_i} I_{om}. \tag{5.36}$$

We perform our design in the (α, β) framework. We need to transform the grid voltage to the stationary frame and calculate the supplied current to the grid based on the stator current. The local-averaged voltage of the stator is $\bar{v}_o = S \times v_i$. Three-phase variables are transformed to two-phase stationary frame [57]

$$\begin{bmatrix} v_\alpha \\ v_\beta \end{bmatrix} = \begin{bmatrix} 1 & 0 & 0 \\ 0 & -\frac{1}{\sqrt{3}} & \frac{1}{\sqrt{3}} \end{bmatrix} \bar{v}_o = \begin{bmatrix} V_{om}\cos\theta_o \\ -V_{om}\sin\theta_o \end{bmatrix}. \tag{5.37}$$

Some designs use v_α and v_β as inputs instead of ω_o and V_{om}. We remind the reader that the output electrical angle and the peak amplitude of the output voltage can be calculated from v_α and v_β as

$$V_{om} = \sqrt{v_\alpha^2 + v_\beta^2} \tag{5.38}$$

$$\theta_o = -\arctan\left(\frac{v_\beta}{v_\alpha}\right). \tag{5.39}$$

To calculate the local averaged current supplied to the grid we use (5.27) where

$$i_o = -\frac{1}{2}\begin{bmatrix} -2 & 0 \\ 1 & \sqrt{3} \\ 1 & -\sqrt{3} \end{bmatrix} \begin{bmatrix} i_\alpha \\ i_\beta \end{bmatrix}. \tag{5.40}$$

Denoting (5.9), (5.10), (5.12)–(5.16), and (5.23) we summarize the state space dynamics of WECS as follows

$$\frac{\mathrm{d}}{\mathrm{d}t}i_\alpha = -a_0 i_\alpha + a_1\lambda_\alpha - a_2\omega_r\lambda_\beta + \frac{\cos\theta_o}{\sigma L_s}V_{om} \tag{5.41}$$

$$\frac{\mathrm{d}}{\mathrm{d}t}i_\beta = -a_0 i_\beta + a_2\omega_r\lambda_\alpha + a_1\lambda_\beta - \frac{\sin\theta_o}{\sigma L_s}V_{om} \tag{5.42}$$

$$\frac{\mathrm{d}}{\mathrm{d}t}\lambda_\alpha = a_3 i_\alpha - a_4\lambda_\alpha + \omega_r\lambda_\beta \tag{5.43}$$

$$\frac{\mathrm{d}}{\mathrm{d}t}\lambda_\beta = a_3 i_\beta - a_4\lambda_\beta - \omega_r\lambda_\alpha \tag{5.44}$$

$$\frac{\mathrm{d}}{\mathrm{d}t}\omega_r = \frac{3p^2 L_m}{2L_r J}(i_\alpha\lambda_\beta - i_\beta\lambda_\alpha) - \frac{pK_s}{nJ}\tilde{\theta} - \frac{pB}{nJ}\left(\omega_t - \frac{\omega_r}{pn}\right) \tag{5.45}$$

$$\frac{\mathrm{d}}{\mathrm{d}t}\theta_o = \omega_o \tag{5.46}$$

$$\frac{\mathrm{d}}{\mathrm{d}t}\tilde{\theta} = \omega_t - \frac{\omega_r}{pn} \tag{5.47}$$

$$\frac{\mathrm{d}}{\mathrm{d}t}\omega_t = -\frac{P_t(V_w,\omega_t)}{J_t\omega_t} - \frac{K_s}{J_t}\tilde{\theta} - \frac{B}{J_t}\left(\omega_t - \frac{\omega_r}{pn}\right), \tag{5.48}$$

where ω_o and V_{om} are actuated by the MC. The wind speed V_w is an unknown disturbance that determines the maximum power level of the WT. A block diagram of WECS that highlights the structure of the state space model (5.41)–(5.48) is shown in Fig. 5.5. Assuming that the blade pitch angle is zero, we can employ the shaft speed of the WT, ω_t, for MPPT of the WT for wind speeds between cut-in and rated wind speed.

5.3 Conventional Direct Field-Oriented Control

In many motor drive systems, it is desirable to make the drive act as a torque transducer wherein the electromagnetic torque can nearly instantaneously be made equal to a torque command. In such a system, speed or position control is dramatically simplified because the electrical dynamics of the drive become irrelevant to the speed or position control problem. In the case of induction machine drives, such performance can be achieved using a class of algorithms collectively known as field-oriented control (FOC) [44]. There are three main categories of FOC known as stator flux, air-gap flux, and rotor flux orientations. The rotor flux scheme is easy to implement and popular in both AC drives and wind energy

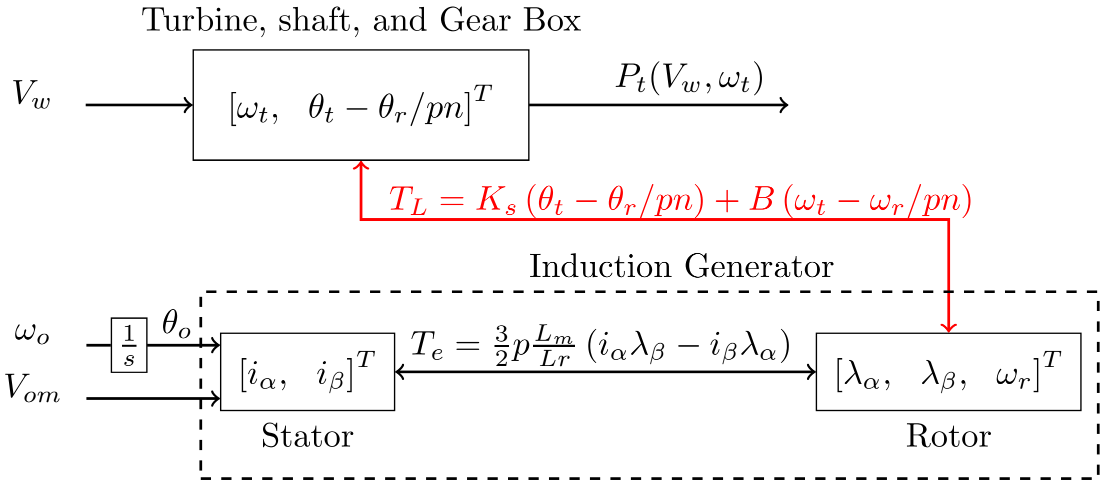

Figure 5.5: Block diagram of WECS.

systems. The FOC decouples the rotor flux

$$|\lambda| = \sqrt{\lambda_\alpha^2 + \lambda_\beta^2} \tag{5.49}$$

and electromagnetic torque T_e of the generator to achieve high dynamic performance. Using the rotor flux orientation, the stator current of the generator can be decomposed into a flux-producing component, which produces the rotor flux $|\lambda|$, and a torque-producing component, which produces the torque T_e. These two components are then controlled independently [80].

The FOC is designed in synchronous reference frame which is introduced as (q, d) frame or dynamic equivalent framework. Aligning the d-axis of the synchronous reference frame with the rotor flux vector results in $\lambda_q = 0$ and $\lambda_d = |\lambda|$, where $|\lambda|$ is the magnitude of the flux vector. From (5.17) we have

$$T_e = \frac{3}{2} p \frac{L_m}{L_r} i_q \lambda_d, \tag{5.50}$$

which shows that a constant rotor flux results in direct changes of torque by the q-axis stator current, i_q. The d-axis current in synchronous reference frame, i_d, is the flux-producing current, whereas the q-axis current i_q is the torque-producing current. In FOC, i_d is normally kept at its rated value while i_q is controlled independently. The stator current vector rotates in space at the synchronous speed and therefore i_d and i_q are DC currents in steady state.

To achieve these conditions we introduce the position of synchronous reference frame as follows

$$\varphi = \frac{\pi}{2} - \arctan\left(\frac{\lambda_\beta}{\lambda_\alpha}\right). \tag{5.51}$$

The estimate of the rotor flux angle φ is a key issue for field orientation. If the angle is obtained through the measurement of generator terminal voltages and currents, the method is known as direct field-oriented control [80]. To apply the FOC we introduce the following transformations

$$\begin{bmatrix} i_q \\ i_d \end{bmatrix} = \begin{bmatrix} \cos\varphi & -\sin\varphi \\ \sin\varphi & \cos\varphi \end{bmatrix} \begin{bmatrix} i_\alpha \\ i_\beta \end{bmatrix} \tag{5.52}$$

$$\begin{bmatrix} \lambda_q \\ \lambda_d \end{bmatrix} = \begin{bmatrix} \cos\varphi & -\sin\varphi \\ \sin\varphi & \cos\varphi \end{bmatrix} \begin{bmatrix} \lambda_\alpha \\ \lambda_\beta \end{bmatrix}. \tag{5.53}$$

Since $\cos\varphi = \lambda_\beta/|\lambda|$ and $\sin\varphi = \lambda_\alpha/|\lambda|$ from (5.52) and (5.53) we have

$$\begin{aligned} i_q &= \frac{\lambda_\beta i_\alpha - \lambda_\alpha i_\beta}{|\lambda|} && (5.54)\\ i_d &= \frac{\lambda_\alpha i_\alpha + \lambda_\beta i_\beta}{|\lambda|} && (5.55)\\ \lambda_q &= 0 && (5.56)\\ \lambda_d &= \sqrt{\lambda_\alpha^2 + \lambda_\beta^2} = |\lambda|. && (5.57) \end{aligned}$$

Here we use v_α and v_β as inputs. We show FOC as a state feedback transformation of a simpler form using the following state space change of coordination

$$\begin{aligned} i_d &= \frac{\lambda_\alpha i_\alpha + \lambda_\beta i_\beta}{\lambda_d} && (5.58)\\ \lambda_d &= \sqrt{\lambda_\alpha^2 + \lambda_\beta^2} && (5.59)\\ i_q &= \frac{\lambda_\beta i_\alpha - \lambda_\alpha i_\beta}{\lambda_d} && (5.60)\\ \omega_t &= \omega_t && (5.61)\\ \alpha_t &= \frac{\mathrm{d}}{\mathrm{d}t}\omega_t && (5.62)\\ \tilde{\theta} &= \tilde{\theta} && (5.63)\\ \varphi &= \frac{\pi}{2} - \arctan\left(\frac{\lambda_\beta}{\lambda_\alpha}\right) && (5.64) \end{aligned}$$

and the state feedback

$$\begin{bmatrix} v_\alpha \\ v_\beta \end{bmatrix} = |\lambda| \begin{bmatrix} \lambda_\beta & -\lambda_\alpha \\ \lambda_\alpha & \lambda_\beta \end{bmatrix}^{-1} \begin{bmatrix} u_q \\ u_d \end{bmatrix} \tag{5.65}$$

under which the system (5.9), (5.10), and (5.12)–(5.16) becomes

$$\frac{\mathrm{d}}{\mathrm{d}t} i_d = -a_0 i_d + a_1 \lambda_d + \omega_r i_q + a_3 \frac{i_q^2}{\lambda_d} + \frac{u_d}{\sigma L_s} \tag{5.66}$$

$$\frac{\mathrm{d}}{\mathrm{d}t} \lambda_d = -a_4 \lambda_d + a_3 i_d \tag{5.67}$$

$$\frac{\mathrm{d}}{\mathrm{d}t} i_q = -a_0 i_q - (i_d + a_2 \lambda_d) \omega_r - a_3 \frac{i_d i_q}{\lambda_d} + \frac{u_q}{\sigma L_s} \tag{5.68}$$

$$\frac{\mathrm{d}}{\mathrm{d}t} \omega_t = \alpha_t \tag{5.69}$$

$$\frac{\mathrm{d}}{\mathrm{d}t} \alpha_t = -c_0 \alpha_t + c_1 \tilde{\theta} + c_2 i_q \lambda_d + c_3 \frac{T_t}{J_t} - \frac{\dot{T}_t}{J_t} \tag{5.70}$$

$$\frac{\mathrm{d}}{\mathrm{d}t} \tilde{\theta} = -\frac{K_s}{B} \tilde{\theta} - \frac{J_t}{B} \alpha_t - \frac{T_t}{B} \tag{5.71}$$

$$\frac{\mathrm{d}}{\mathrm{d}t} \varphi = \omega_r + a_3 \frac{i_q}{\lambda_d} \tag{5.72}$$

where

$$\omega_r = pn \left(\omega_t + \frac{J_t}{B} \alpha_t + \frac{K_s}{B} \tilde{\theta} + \frac{T_t}{B} \right). \tag{5.73}$$

Defining the nonlinear state feedback control

$$\begin{bmatrix} u_q \\ u_d \end{bmatrix} = \sigma L_s \begin{bmatrix} \omega_r i_d + a_2 \omega_r \lambda_d + a_3 \frac{i_d i_q}{\lambda_d} + w_q \\ -a_1 \lambda_d - \omega_r i_q - a_3 \frac{i_q^2}{\lambda_d} + w_d \end{bmatrix} \tag{5.74}$$

the following closed-loop system

$$\frac{\mathrm{d}}{\mathrm{d}t} i_d = -a_0 i_d + w_d \tag{5.75}$$

$$\frac{\mathrm{d}}{\mathrm{d}t} \lambda_d = -a_4 \lambda_d + a_3 i_d \tag{5.76}$$

$$\frac{\mathrm{d}}{\mathrm{d}t} i_q = -a_0 i_q + w_q \tag{5.77}$$

$$\frac{\mathrm{d}}{\mathrm{d}t} \omega_t = \alpha_t \tag{5.78}$$

$$\frac{\mathrm{d}}{\mathrm{d}t} \alpha_t = -c_0 \alpha_t + c_1 \tilde{\theta} + c_2 i_q \lambda_d + c_3 \frac{T_t}{J_t} - \frac{\dot{T}_t}{J_t} \tag{5.79}$$

$$\frac{\mathrm{d}}{\mathrm{d}t} \tilde{\theta} = -\frac{K_s}{B} \tilde{\theta} - \frac{J_t}{B} \alpha_t - \frac{T_t}{B} \tag{5.80}$$

$$\frac{\mathrm{d}}{\mathrm{d}t} \varphi = \omega_r + a_3 \frac{i_q}{\lambda_d} \tag{5.81}$$

is obtained. When flux amplitude, λ_d, is regulated to a constant reference value, and considering the fact that the dynamics of ω_t are considerably slower than the electrical dynamics, we can assume that the dynamics are linear, but during flux transient the system has nonlinear terms and it is coupled. This method can be improved by achieving exact input-output decoupling and linearization via a nonlinear state feedback that is not more complex than the conventional field-oriented control [52]. In the next section we present our decoupling control based on FOC method.

5.4 Controller Design

As shown in Fig. 5.5 one can manipulate stator voltage amplitude, V_{om}, and its frequency, ω_o, through the matrix converter to obtain the desired closed-loop performance for WECS. Referring to [49, 50, 52] and employing FOC idea we introduce an integrator and an auxiliary input, u_2, to achieve input-output decoupling in WECS dynamics. Using (5.41)–(5.48) and one step of integration in front of V_{om} the extended equations of WECS are introduced as follows:

$$\dot{x}_1 = -a_0 x_1 + a_1 x_3 - a_2 x_4 x_7 + \frac{x_6 \cos x_5}{\sigma L_s} \tag{5.82}$$

$$\dot{x}_2 = -a_0 x_2 + a_2 x_3 x_7 + a_1 x_4 - \frac{x_6 \sin x_5}{\sigma L_s} \tag{5.83}$$

$$\dot{x}_3 = a_3 x_1 - a_4 x_3 + x_4 x_7 \tag{5.84}$$

$$\dot{x}_4 = a_3 x_2 - a_4 x_4 - x_3 x_7 \tag{5.85}$$

$$\dot{x}_5 = u_1 \tag{5.86}$$

$$\dot{x}_6 = u_2 \tag{5.87}$$

$$\dot{x}_7 = a_5 \left(x_1 x_4 - x_2 x_3\right) - a_6 x_8 - a_7 \left(x_9 - \frac{x_7}{pn}\right) \tag{5.88}$$

$$\dot{x}_8 = x_9 - \frac{x_7}{pn} \tag{5.89}$$

$$\dot{x}_9 = -a_9 \left(x_9 - \frac{x_7}{pn}\right) - a_8 x_8 - \frac{T_t}{J_t}, \tag{5.90}$$

where $x = \left[i_\alpha,\ i_\beta,\ \lambda_\alpha,\ \lambda_\beta,\ \theta_o,\ V_{om},\ \omega_r,\ \tilde{\theta},\ \omega_t\right]^T$, u_1 is the electrical frequency of the stator, ω_o , and u_2 is an auxiliary input (voltage amplitude rate) which generates the voltage amplitude of the stator. The constant parameters are defined in the Table 5.2. The extended dynamics of the WECS are of the form

$$\dot{x} = f(x) + g_1 u_1 + g_2 u_2, \quad x \in \mathbb{R}^9, \quad u \in \mathbb{R}^2, \tag{5.91}$$

where

$$f(x) = \begin{bmatrix} -a_0 x_1 + a_1 x_3 - a_2 x_4 x_7 + \frac{x_6 \cos x_5}{\sigma L_s} \\ -a_0 x_2 + a_2 x_3 x_7 + a_1 x_4 - \frac{x_6 \sin x_5}{\sigma L_s} \\ a_3 x_1 - a_4 x_3 + x_4 x_7 \\ a_3 x_2 - a_4 x_4 - x_3 x_7 \\ 0 \\ 0 \\ a_5 \left(x_1 x_4 - x_2 x_3 \right) - a_6 x_8 - a_7 \left(x_9 - \frac{x_7}{pn} \right) \\ x_9 - \frac{x_7}{pn} \\ -a_9 \left(x_9 - \frac{x_7}{pn} \right) - a_8 x_8 - \frac{T_t}{J_t} \end{bmatrix} \tag{5.92}$$

$$g_1 = [0\ 0\ 0\ 0\ 1\ 0\ 0\ 0\ 0]^T \tag{5.93}$$

$$g_2 = [0\ 0\ 0\ 0\ 0\ 1\ 0\ 0\ 0]^T . \tag{5.94}$$

From (5.6) and Fig. 5.4 we know that the turbine shaft speed controls the power generation. Also we are interested in decoupling the rotor flux and electromagnetic torque to obtain the benefits of FOC. For these reasons, we introduce wind turbine speed, $y_1 = \omega_t$, and flux amplitude, $\eta_1 = |\lambda|^2$, as measurable outputs. Based on the selected outputs and following the idea of feedback linearization, the following change of variables is applied to WECS dynamics

$$y_1 = \Psi_1(x) = x_9 \tag{5.95}$$

$$y_2 = \mathcal{L}_f \Psi_1(x) = -a_9 \left(x_9 - \frac{x_7}{pn} \right) - a_8 x_8 - \frac{T_t}{J_t} \tag{5.96}$$

$$y_3 = \mathcal{L}_f^2 \Psi_1(x) = b_0 \xi_1 + b_1 \mathcal{L}_f \Psi_1(x) + b_2 x_8 + b_3 \frac{T_t}{J_t} - \frac{\dot{T}_t}{J_t} \tag{5.97}$$

$$\begin{aligned} y_4 = \mathcal{L}_f^3 \Psi_1(x) &= b_4 \mathcal{L}_f^2 \Psi_1(x) + b_5 \mathcal{L}_f \Psi_1(x) + b_6 x_8 + \\ &+ \frac{b_0}{\sigma L_s} x_6 \lambda_d - x_7 \Big(b_7 \Psi_2(x) + b_8 \mathcal{L}_f \Psi_2(x) \Big) + \\ &+ b_9 \frac{T_t}{J_t} + b_{10} \frac{\dot{T}_t}{J_t} - \frac{\ddot{T}_t}{J_t} \end{aligned} \tag{5.98}$$

$$\eta_1 = \Psi_2(x) = x_3^2 + x_4^2 \tag{5.99}$$

$$\eta_2 = \mathcal{L}_f \Psi_2(x) = 2a_3 \xi_2 - 2a_4 \Psi_2(x) \tag{5.100}$$

$$\begin{aligned} \eta_3 = \mathcal{L}_f^2 \Psi_2(x) &= b_{12} \Psi_2(x) - b_{11} \mathcal{L}_f \Psi_2(x) + \\ &+ b_{13} x_7 \left(\mathcal{L}_f^2 \Psi_1(x) - b_1 \mathcal{L}_f \Psi_1(x) - b_2 x_8 - b_3 \frac{T_t}{J_t} + \frac{\dot{T}_t}{J_t} \right) + \\ &+ 2a_3^2 \frac{\xi_1^2 + \xi_2^2}{\Psi_2(x)} + \frac{2a_3}{\sigma L_s} x_6 \lambda_q \end{aligned} \tag{5.101}$$

$$\tilde{\theta} = x_8 \tag{5.102}$$

$$\varphi = \frac{\pi}{2} - \arctan\left(\frac{x_4}{x_3} \right), \tag{5.103}$$

where $\xi_1 = x_1 x_4 - x_2 x_3,\ \xi_2 = x_1 x_3 + x_2 x_4$, and

$$\begin{bmatrix} \lambda_q \\ \lambda_d \end{bmatrix} = \begin{bmatrix} \cos x_5 & -\sin x_5 \\ \sin x_5 & \cos x_5 \end{bmatrix} \begin{bmatrix} x_3 \\ x_4 \end{bmatrix}. \tag{5.104}$$

The change of variables (5.95)–(5.103) is one to one in $X = \{x \in \mathbb{R}^9 : x_3^2 + x_4^2 \neq 0, x_9 \neq 0\}$ and onto $Y = \{(y, \eta, \tilde{\theta}, \varphi) \in \mathbb{R}^9 : \eta_1 > 0, 0 \leq \varphi \leq \pi\}$. The inverse transformation of (5.95)–(5.103) is

$$x_1 = \frac{-\Upsilon_1 \sin\varphi + \Upsilon_2 \cos\varphi}{\sqrt{\eta_1}} \tag{5.105}$$

$$x_2 = \frac{\Upsilon_1 \cos\varphi + \Upsilon_2 \sin\varphi}{\sqrt{\eta_1}} \tag{5.106}$$

$$x_3 = \sqrt{\eta_1} \cos\varphi \tag{5.107}$$

$$x_4 = \sqrt{\eta_1} \sin\varphi \tag{5.108}$$

$$x_5 = \arctan\left(\frac{\Upsilon_4}{\Upsilon_3}\right) \tag{5.109}$$

$$x_6 = \sqrt{\Upsilon_3^2 + \Upsilon_4^2} \tag{5.110}$$

$$x_7 = pn\left(y_1 + \frac{y_2}{a_9} + \frac{a_8}{a_9}\tilde{\theta} + \frac{T_t}{a_9 J_t}\right) \tag{5.111}$$

$$x_8 = \tilde{\theta} \tag{5.112}$$

$$x_9 = y_1 \tag{5.113}$$

where

$$\Upsilon_1 = \frac{1}{b_0}\left(y_3 - b_1 y_2 - b_2\tilde{\theta} - b_3\frac{T_t}{J_t} + \frac{\dot{T}_t}{J_t}\right) \tag{5.114}$$

$$\Upsilon_2 = \frac{\eta_2 + 2a_4\eta_1}{2a_3} \tag{5.115}$$

$$\Upsilon_3 = \frac{\Phi_1 \cos\varphi + \Phi_2 \sin\varphi}{\sqrt{\eta_1}} \tag{5.116}$$

$$\Upsilon_4 = \frac{-\Phi_1 \sin\varphi + \Phi_2 \cos\varphi}{\sqrt{\eta_1}}, \tag{5.117}$$

with

$$\begin{aligned}\Phi_1 = \frac{\sigma L_s}{2a_3}\Bigg(&\eta_3 + b_{11}\eta_2 - b_{12}\eta_1 - 2a_3^2\frac{\Upsilon_1^2 + \Upsilon_2^2}{\eta_1} - \\ &-b_{13}x_7\left(y_3 - b_1 y_2 - b_2\tilde{\theta} - b_3\frac{T_t}{J_t} + \frac{\dot{T}_t}{J_t}\right)\Bigg)\end{aligned} \tag{5.118}$$

$$\begin{aligned}\Phi_2 = \frac{\sigma L_s}{b_0}\Bigg(&y_4 - b_4 y_3 - b_5 y_2 - b_6\tilde{\theta} + x_7\left(b_7\eta_1 + b_8\eta_2\right) - \\ &-b_9\frac{T_t}{J_t} - b_{10}\frac{\dot{T}_t}{J_t} + \frac{\ddot{T}_t}{J_t}\Bigg).\end{aligned} \tag{5.119}$$

The change of variables results in the following equations:

$$\dot{y}_1 = y_2 \tag{5.120}$$

$$\dot{y}_2 = y_3 \tag{5.121}$$

$$\dot{y}_3 = y_4 \tag{5.122}$$

$$\dot{y}_4 = g_1 + \frac{b_0 \lambda_q}{\sigma L_s} x_6 u_1 + \frac{b_0 \lambda_d}{\sigma L_s} u_2 \tag{5.123}$$

$$\dot{\eta}_1 = \eta_2 \tag{5.124}$$

$$\dot{\eta}_2 = \eta_3 \tag{5.125}$$

$$\dot{\eta}_3 = g_2 - \frac{2a_3 \lambda_d}{\sigma L_s} x_6 u_1 + \frac{2a_3 \lambda_q}{\sigma L_s} u_2 \tag{5.126}$$

$$\dot{\tilde{\theta}} = -\frac{y_2}{a_9} - \frac{a_8}{a_9}\tilde{\theta} - \frac{T_t}{a_9 J_t} \tag{5.127}$$

$$\dot{\varphi} = \omega_r + \frac{a_3}{b_0|\lambda|}\left(y_3 - b_1 y_2 - b_2\tilde{\theta} - b_3\frac{T_t}{J_t} + \frac{\dot{T}_t}{J_t}\right), \tag{5.128}$$

where (5.127) and (5.128) are zero dynamics of the system and

$$\begin{aligned} g_1 = {} & b_4 y_4 + b_5 y_3 - \frac{b_6}{a_9} y_2 - \frac{a_8 b_6}{a_9}\tilde{\theta} + \\ & + \frac{b_0 x_6}{\sigma L_s}\left(a_3 i_d - a_4 \lambda_d - x_7 \lambda_q\right) + \\ & + f_7(x)\left(b_7 \eta_1 + b_8 \eta_2\right) - x_7\left(b_7 \eta_2 + b_8 \eta_3\right) - \\ & - \frac{b_6}{a_9}\frac{T_t}{J_t} + b_9 \frac{\dot{T}_t}{J_t} + b_{10}\frac{\ddot{T}_t}{J_t} - \frac{\dddot{T}_t}{J_t} \end{aligned} \tag{5.129}$$

$$\begin{aligned} g_2 = {} & -b_{11}\eta_3 + b_{12}\eta_2 + b_0 b_{13} f_7(x)\xi_1 + \\ & + b_{13} x_7 \left(y_4 - b_1 y_3 - b_2 f_8(x) - b_3\frac{\dot{T}_t}{J_t} + \frac{\ddot{T}_t}{J_t}\right) + \\ & + 2a_3^2\left(2a_1\xi_3 - 2a_0\xi_2 - 2a_2 x_7 \xi_1 + \frac{2x_6}{\sigma L_s} i_q\right) + \\ & + \frac{2a_3 x_6}{\sigma L_s}\left(a_3 i_q - a_4 \lambda_q + x_7 \lambda_d\right), \end{aligned} \tag{5.130}$$

where

$$\begin{bmatrix} i_q \\ i_d \end{bmatrix} = \begin{bmatrix} \cos x_5 & -\sin x_5 \\ \sin x_5 & \cos x_5 \end{bmatrix} \begin{bmatrix} x_1 \\ x_2 \end{bmatrix}. \tag{5.131}$$

When the system settles down to a constant y_1 and η_1 under a constant wind speed, we have $y_2 = y_3 = y_4 = 0$, $\eta_2 = \eta_3 = 0$, and (5.127) gives

$$\tilde{\theta} = -\frac{T_t}{a_8 J_t}. \tag{5.132}$$

Then (5.128) results in

$$\dot{\varphi} = \omega_r + \frac{a_3(a_8 - b_3)}{b_0 J_t}\frac{T_t}{|\lambda|}. \tag{5.133}$$

The difference between flux angular speed, $\dot{\varphi}$, and rotor electrical speed, ω_r, is usually called slip speed, ω_{sl}, which can be expressed as

$$\omega_{sl} = \dot{\varphi} - \omega_r = \frac{a_3(a_8 - b_3)}{b_0 J_t}\frac{T_t}{|\lambda|} \tag{5.134}$$

which shows that a constant rotor flux amplitude causes direct changes of the slip with the variations of the mechanical torque. By defining control signals as follows

$$\begin{bmatrix} u_2 \\ \\ x_6 u_1 \end{bmatrix} = \frac{\sigma L_s}{\sqrt{\eta_1}} \begin{bmatrix} \cos(\varphi - \theta_o) & -\sin(\varphi - \theta_o) \\ \\ \sin(\varphi - \theta_o) & \cos(\varphi - \theta_o) \end{bmatrix} \begin{bmatrix} \frac{v_1 - g_1}{b_0} \\ \\ \frac{g_2 - v_2}{2a_3} \end{bmatrix}, \tag{5.135}$$

and applying another step of change of variables

$$z = \left[y_1 - \omega_t^{ref},\ y_2,\ y_3,\ y_4\right]^T \tag{5.136}$$

$$\zeta = \left[\eta_1 - \left(|\lambda|^{ref}\right)^2,\ \eta_2,\ \eta_3\right]^T \tag{5.137}$$

we obtain

$$\dot{z}_1 = z_2 \tag{5.138}$$

$$\dot{z}_2 = z_3 \tag{5.139}$$

$$\dot{z}_3 = z_4 \tag{5.140}$$

$$\dot{z}_4 = v_1 \tag{5.141}$$

$$\dot{\zeta}_1 = \zeta_2 \tag{5.142}$$

$$\dot{\zeta}_2 = \zeta_3 \tag{5.143}$$

$$\dot{\zeta}_3 = v_2 \tag{5.144}$$

$$\dot{\tilde{\theta}} = -\frac{z_2}{a_9} - \frac{a_8}{a_9}\tilde{\theta} - \frac{T_t}{a_9 J_t} \tag{5.145}$$

$$\dot{\varphi} = \omega_r + \frac{a_3}{b_0|\lambda|}\left(z_3 - b_1 z_2 - b_2\tilde{\theta} - b_3\frac{T_t}{J_t} + \frac{\dot{T}_t}{J_t}\right). \tag{5.146}$$

Linear state feedback

$$v_1 = -k'_1 z_1 - k'_2 z_2 - k'_3 z_3 - k'_4 z_4 \tag{5.147}$$

$$v_2 = -k''_1 \zeta_1 - k''_2 \zeta_2 - k''_3 \zeta_3 \tag{5.148}$$

stabilizes this system which results in the regulation of wind turbine speed, $\omega_t = y_1$, to its reference value ω_t^{ref} while amplitude of rotor flux, $|\lambda| = \sqrt{\eta_1}$, has converged to its desired value, $|\lambda|^{ref}$.

Remark 4 The closed-loop system (5.138)–(5.146) is input-output decoupled and linear. The input-output map consists of fourth-order and third-order systems. This allows for an independent regulation (or tracking) of the outputs using control signals (5.147) and (5.148). Transient response are now decoupled also when $|\lambda|^{ref}$ is varied, even independently of ω_t^{ref}. **This is an improvement over FOC.**

Remark 5 State space change of coordinates both in the FOC and in the decoupling control are valid when $\lambda_\alpha^2 + \lambda_\beta^2 \neq 0$ and $\omega_t \neq 0$ which is a physical singularity of WECS in starting conditions.

Remark 6 As in FOC, while measurements of $(i_\alpha, i_\beta, \omega_r)$ are available, measurements of $(\lambda_\alpha, \lambda_\beta)$ require installing flux sensing coils or Hall effect transducers in the stator which is not realistic in general purpose squirrel cage machines. But, $(\lambda_\alpha, \lambda_\beta)$ flux components can be reconstructed by means of an asymptotic observer of reduced order as shown in [11].

Remark 7 The torque-speed characteristic of an induction machine is normally quite steep in the neighborhood of synchronous speed and so the electrical rotor speed will be near the electrical frequency. This means that changing the reference value of the wind turbine speed which translates in variation of the rotor speed eventually results in changing the electrical frequency of the stator [44]. Thus, by controlling the frequency one can approximately control the speed or vice versa.

Furthermore, the a-phase voltage equation can be expressed as

$$v_{as} = R_s i_{as} + \frac{\mathrm{d}}{\mathrm{d}t}\lambda_{as}. \tag{5.149}$$

For steady-state conditions at intermediate to high speeds wherein the flux linkage term dominates the resistive term in the voltage equation, the magnitude of the applied voltage is related to the magnitude of the stator flux linkage by

$$V_s = \omega_o \Lambda_s \tag{5.150}$$

which suggests that in order to maintain constant flux linkage (to avoid saturation), the stator voltage magnitude should be proportional to frequency [44]. Since we regulate the flux to a constant value, the voltage will be proportional to the electrical frequency. In the next section we use our designed controller combined with an ES algorithm to extract maximum power from WECS under various wind speeds.

5.5 Maximum Power Point Tracking using ES

There are three main MPPT techniques for WECS: Wind Speed Measurement (WSM), P&O, and Power Signal Feedback (PSF). Measurement of wind velocity is required in WSM method. It is clear that accurate measurement of wind velocity is complicated and increases the system cost. Since the P&O method adds delay, it is not practical for medium- and large-inertia wind turbine systems. To implement PSF control, maximum power curve (maximum power versus shaft speed) is required. The maximum power is then tracked by shaft speed control [9].

Figure 5.6 shows a typical block diagram of WSM using direct FOC for the induction generator [16, 80]. To implement FOC scheme, the rotor flux magnitude $|\lambda|$ and its angle φ are identified by the rotor flux calculator based on the measured stator voltage (v_o) and current (i_o). The torque reference T_e^{ref} is generated by the MPPT scheme. The q-axis stator current reference can then be calculated by

$$i_q^{ref} = \frac{2L_r}{3pL_m} \frac{T_e^{ref}}{\lambda_d}. \tag{5.151}$$

Model-based MPPT algorithms require reliable and up-to-date information about the WT. In the simplest case they are look-up tables which link the proper reference value of electrical torque, T_e^{ref}, to the relevant turbine speed or wind speed. System

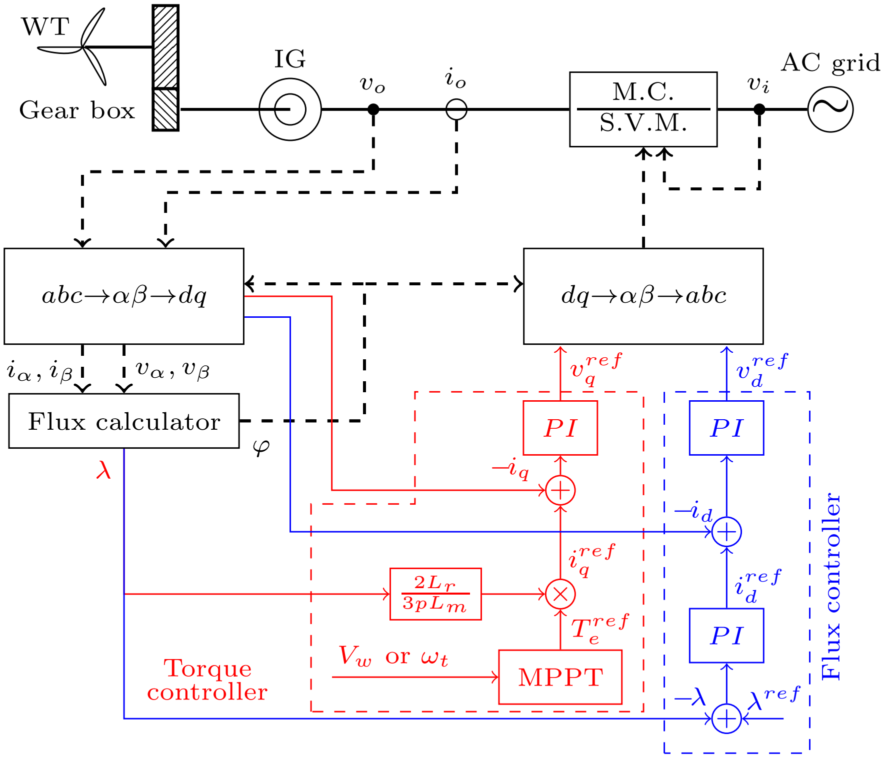

Figure 5.6: MPPT for a WECS based on WSM using conventional direct FOC.

identification and data acquisition are necessary on a per turbine basis prior to operating.

To overcome these challenges and remove the dependence of the MPPT algorithm on the system modeling and identification we propose extremum seeking algorithm which is a non-model-based real-time optimization technique to MPPT of WECS. First we try ES without the inner-loop control to clarify the advantages of the proposed controller on the closed-loop performance of the system. According to Remark 7, changes in the stator electrical frequency have the same effect as the changes in the rotor speed on the power generation. Consequently, Assumption 5 can be rephrased as follows:

Assumption 6 *The following holds for the turbine mechanical power around its* *peak point for every wind speed*

$$\begin{aligned} \frac{\partial P_t(V_w,\omega_o)}{\partial \omega_o}(\omega_o^*) &= 0 && (5.152)\\ \frac{\partial^2 P_t(V_w,\omega_o)}{\partial \omega_o^2}(\omega_o^*) &< 0. && (5.153) \end{aligned}$$

Also we know that the the Jacobian of WECS has left-half plane poles at each working point which makes the system exponentially stable. According to [45] these conditions are sufficient for convergence of an ES algorithm to the peak point of the cost function, P_t^*, when the initial condition is close enough to its optimal value, ω_t^*. A schematic of MPPT for WECS with extremum seeking without inner-loop nonlinear control is shown in Fig. 5.7. It is clear that the power is parametrized by ω_o, which is estimated by ES loop. The other input for WECS which generates the voltage amplitude has been set to zero which means the stator voltage has a constant peak amplitude. The parameters of the ES loop are defined as follows:

$$\begin{aligned} \Omega &= \epsilon\Omega' && (5.154)\\ \Omega_H &= \epsilon\Omega'_H = \epsilon\delta\Omega''_H = O(\epsilon\delta) && (5.155)\\ \Omega_L &= \epsilon\Omega'_L = \epsilon\delta\Omega''_L = O(\epsilon\delta) && (5.156)\\ k &= \epsilon k' = \epsilon\delta k'' = O(\epsilon\delta), && (5.157) \end{aligned}$$

where Ω' is a rational number, ϵ and δ are small positive constants, and Ω''_H, Ω''_L, and k'' are $O(1)$ positive constants. Also a needs to be small.

Our analytical results for this case (no inner-loop control) are summarized in the theorem below, the proof of which follows from [45].

Theorem 5 *Consider the system (5.91) with $u_2 = 0$ under Assumption 6 and recall that for any fixed electrical frequency $u_1 = \omega_o$ system (5.91) is exponentially stable. For the system in Fig. 5.7 there exists a ball of initial conditions around the point $(x, \hat{\omega}_o, \hat{g}, \bar{p}) = (l(\omega_o^*), \omega_o^*, 0, P_t^*)$ and constants $\bar{\epsilon}$, $\bar{\delta}$, and $\bar{a}$ such that for all $\epsilon \in (0, \bar{\epsilon})$, $\delta \in (0, \bar{\delta})$, and $a \in (0, \bar{a})$, the solution $(x(t), \hat{\omega}_o(t), \hat{g}(t), \bar{p}(t))$ exponentially converges to an $O(\epsilon+\delta+a)$-neighborhood of that point. Furthermore, $P_t(t)$ converges to an $O(\epsilon+\delta+a)$-neighborhood of P_t^*.*

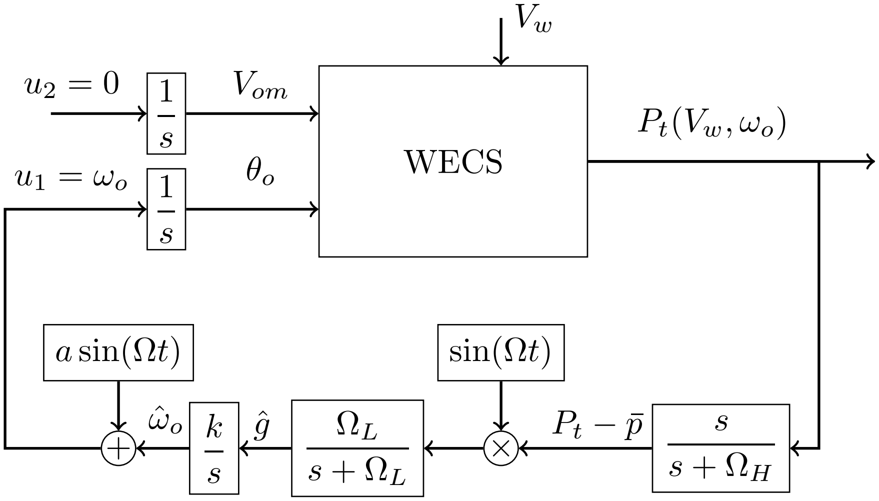

Figure 5.7: MPPT for a WECS based on extremum seeking without the inner-loop control.

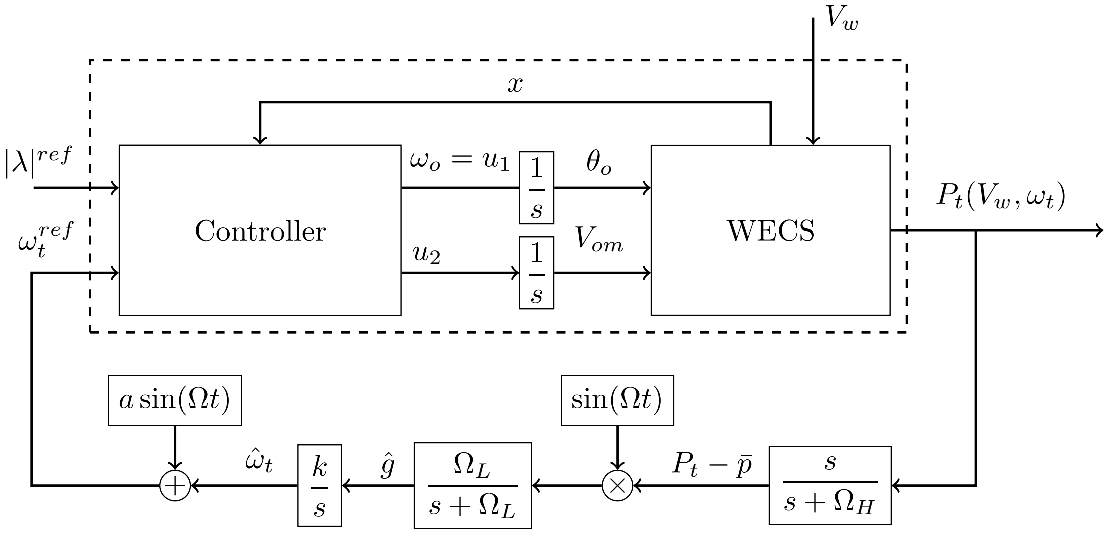

Figure 5.8: Extremum seeking for MPPT in WECS with the inner-loop control.

We use the mechanical power at the wind turbine shaft as the cost function as the input of ES scheme. The optimization parameter for ES without the inner-loop control is the electrical frequency of IG stator, ω_o. Stability of system dynamics is a sufficient condition for convergence of ES algorithm to its peak point. It is also required that the ES algorithm works more slowly than the WECS system dynamics. As previously mentioned, since WECS in Fig. 5.7 without the inner-loop controller shows a slow transient, the entire system has a lengthy convergence process.

To overcome these issues we propose to employ the nonlinear control from Section 5.4 to achieve the desired closed-loop performance, including faster response time, and preventing magnetic saturation. In this case, the reference inputs of the inner-loop control are ω_t^{ref} and $|\lambda|^{ref}$. From Assumption 5, we know that the peak power is defined by the optimal shaft speed at each wind speed which is estimated by the ES loop. The other control input, $|\lambda|^{ref}$ defines the level of the flux linkage of the rotor which prevents IG from magnetic saturation.

Remark 8 From (5.5) and (5.6) we observe that the torque on the wind turbine shaft depends on the wind speed and shaft speed. Also to implement the controller in Section 5.4 we need to have access to the first, second, and third order derivatives of the torque. Because of the separation of time scales in the dynamics of the inner-loop and the wind turbine, it is reasonable to assume that (for the inner-loop design) variation of the wind speed is negligible in comparison to the dynamics of WECS and controller. Since the convergence time of the estimate of the shaft speed generated by ES loop is considerably slower than the response time of the combination of WECS and controller we can assume that the derivatives of the torque are zero. Using this observation, the inner-loop becomes independent of the turbine power map, but it still relies on the IG dynamics and measurements of the turbine power, the shaft speed (ω_t), and angle displacement caused by the shaft model ($\tilde{\theta}$). The ES algorithm generates the estimate of the shaft speed which is the reference input for the inner-loop and maximizes the power generated by the WT, and governs the system to its peak power, despite high uncertainty in the turbine power map.

The ES scheme of [45] is shown in Fig. 5.8. Combination of the Controller and WECS includes fast dynamics and ES algorithm contains slow and medium speed dynamics. The ES algorithm estimates the optimal turbine speed, $\omega_t^{ref} = \omega_t^*$ which can be considered as a constant value with respect to the fast dynamics of the controller-system. The ES scheme estimates the gradient of the cost function, P_t, by injecting a small perturbation, $a\sin(\Omega t)$, which is very slow with respect to the dynamics of the WECS and its amplitude is enough small in comparison to ω_t. The highpass filter removes the DC part of the signal. The multiplication of the resulting signal by $\sin(\Omega t)$ creates an estimate of the gradient of the cost function, which is smoothed using a lowpass filter. When ω_t is larger than its optimal value the estimate of the gradient, $\hat{g}$, is negative and causes ω_t to decrease. On the other hand, when ω_t is smaller than ω_t^* then $\hat{g} > 0$ which increases the ω_t toward ω_t^*. It should be noted that Ω is small enough in comparison to the slowest dynamic of the system-controller, with an order less than 10%.

The analytical results for the closed-loop system with the ES design are summarized in the theorem below, the proof of which also follows from [45].

Theorem 6 *Consider the feedback system in Fig. 5.8 which includes the plant (5.91) under Assumption 5 with control input (5.135) where* v_1 *and* v_2 *are defined as (5.147) and (5.148). There exists a ball of initial conditions around the point* $(x, \hat{\omega}_t, \hat{g}, \bar{p}) = (l(\omega_t^*), \omega_t^*, 0, P_t^*)$ *and constants* $\bar{\epsilon}$, $\bar{\delta}$ *, and* $\bar{a}$ *such that for all* $\epsilon \in (0, \bar{\epsilon})$, $\delta \in (0, \bar{\delta})$*, and* $a \in (0, \bar{a})$*, the solution* $(x(t), \hat{\omega}_t(t), \hat{g}(t), \bar{p}(t))$ *exponentially converges to an* $O(\epsilon + \delta + a)$*-neighborhood of that point. Furthermore,* $P_t(t)$ *converges to an* $O(\epsilon + \delta + a)$*-neighborhood of* P_t^**. Also the magnetic saturation is avoided by selecting a constant reference for the flux amplitude,* $|\lambda|^{ref}$*.*

5.6 Simulation Results

First, we simulate the ES without the inner-loop control, according to the scheme in Fig. 5.7. The open-loop response time of the system with the selected parameters in Table 5.1 is about 500 ms. We know that the ES loop has to be considerably slower than the main dynamics with an order about 10 which results

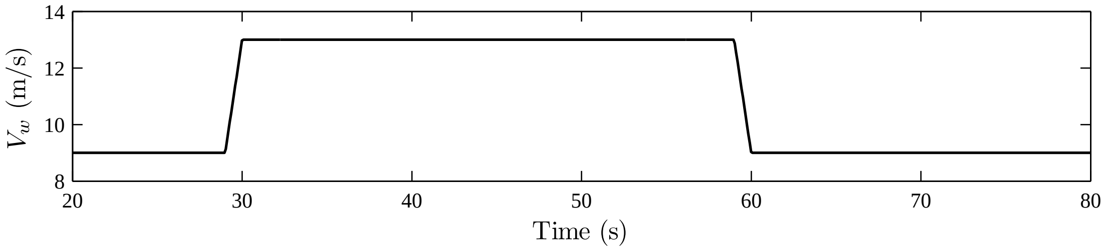

Figure 5.9: Variation of wind speed versus time.

in low probing frequency for the perturbation signal. We select $\Omega = 20$ rad/s, $\Omega_L = 2$ rad/s, and $\Omega_H = 1$ rad/s. Denoting the fact that the ES convergence time is about 30 cycles of the probing function oscillation, the system reaches its peak point in 10 s. Figure 5.9 shows the wind regime applied to the WECS. The wind speed changes happen at time 29 s and 59 s with a duration of 1 s. In this simulation (no inner-loop control) the peak amplitude of the stator is fixed at 1000 V which force $u_2 = 0$ and the ES gain is $k = 0.02$. The MPPT process is shown in Fig. 5.10. It is clear from Fig. 5.10 (portions in blue) that during wind speed increases, the MPPT responds slowly, and the efficiency of WECS reduces. The recovery time is also considerable when the wind speed drops.

To improve the response time of the MPPT, we add the inner-loop control shown in Fig. 5.8, and repeat the above simulation. By appropriate selection of the feedback gains in (5.147) and (5.148) and using (5.135) we can obtain the desired closed loop response time. Control signals are designed such that the poles of z-error subsystem (5.138)–(5.141) and ζ-error subsystems (5.142)–(5.144) move to $P_z = [-550\ -600\ -650\ -700]$ and $P_\zeta = [-570\ -620\ -670]$, respectively. The response time of the closed-loop system is about 20 ms which is 25 times faster than the open-loop system. We select the parameters of the extremum seeking loop as follows: $\Omega = 100$ rad/s, $\Omega_L = 6$ rad/s, $\Omega_H = 5$ rad/s, $a = 0.1$, and $k = 0.004$. The amplitude of the perturbation function is selected proportional to the wind turbine shaft speed. Higher values of a reduce the precision of the MPPT, as shown in Theorem 6. For the same wind speed profile in Fig. 5.9, our simulation results, shown in Fig. 5.10 (in red) show that the MPPT with the inner loop converges to its optimal value in less than 10 cycles of the probing function,

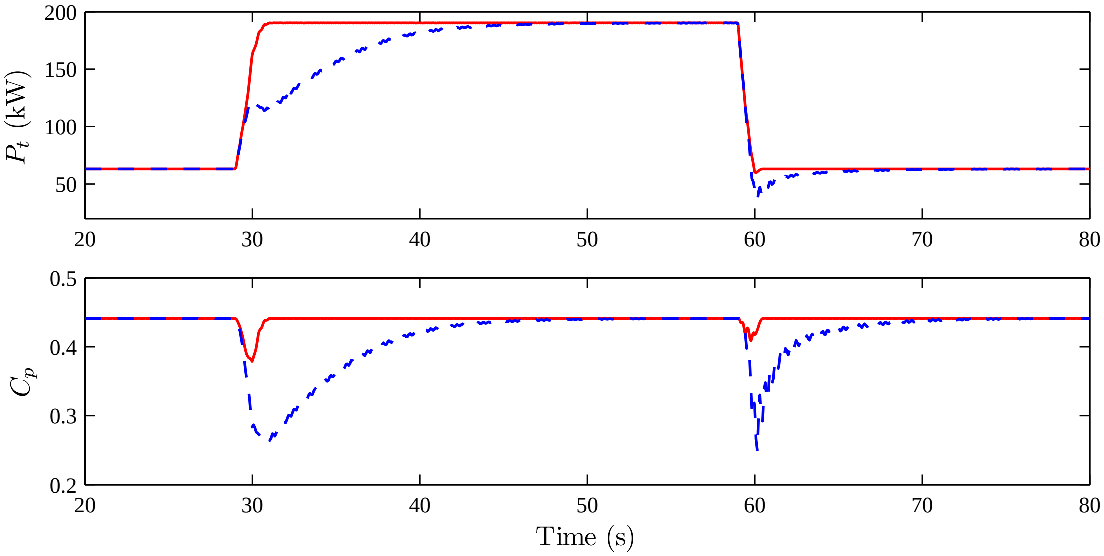

Figure 5.10: MPPT, (solid red) with and (dashed- blue) without the inner-loop control.

resulting in near instant tracking of the MPP. Consequently, the performance of the MPPT in response to the sudden changes in wind speed is dramatically better with the inner-loop control than without.

We argued that the inner-loop control can regulate the rotor flux amplitude to a constant value which provides the system with the extra benefit of constant v/f. Fig. 5.11 shows that for the constant flux amplitude, $|\lambda|^{ref} = \sqrt{10}$ Vs, the ratio of voltage to frequency in the MPPT with the inner-loop control is almost constant, despite wind speed variation, which implies that magnetic saturation is prevented. On the other hand, without inner-loop control, the system exhibits variations of v/f when wind speed changes, as is seen in Fig. 5.11, that might cause flux saturation.

5.7 Conclusions

We presented an extremum-seeking algorithm to extract maximum power from a WECS for wind speed from cut-in wind speed to rated wind speed. The design employed an inner-loop nonlinear controller based on field-oriented approach

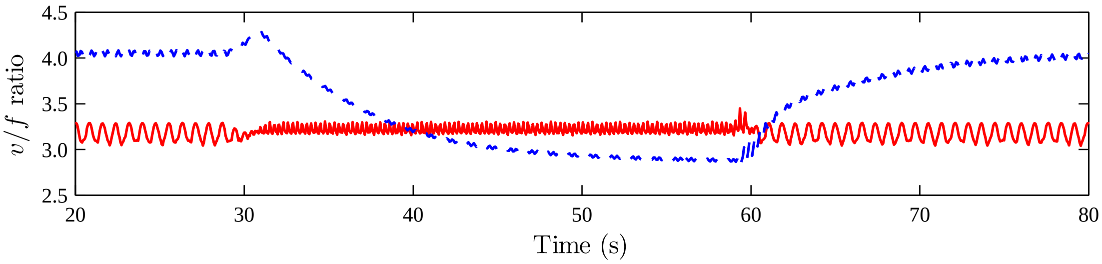

Figure 5.11: Variation of v/f for MPPT, (solid red) with and (dashed blue) without the inner-loop control.

and feedback linearization technique to control the closed-loop transient performance, with respect to which the ES had to be tuned. Without this inner-loop control, the convergence rate of the closed-loop system would be much slower. This optimization/control algorithm can readily be extended to other classes of WECS without major changes. The main parameters that need to be adjusted are the probing frequency and amplitude of the perturbation signal. Furthermore, the proposed control strategy prevents magnetic saturation in the induction generator.

This chapter contains material from A. Ghaffari, M. Krstić, and S. Seshagiri, "Power Optimization and Control in Wind Energy Conversion Systems using Extremum Seeking," Submitted to the *IEEE Transactions on Control Systems Technology*. Of which the dissertation author was the primary author.

Chapter 6

Summary and Suggestions for Future Work

Since environmental parameters like solar irradiance and wind speed define the power map and peak power of Photovoltaic modules and Wind Energy Conversion Systems (WECS), we propose Extremum Seeking (ES), which is a non-model-based optimization algorithm, for power maximization of PV modules and WECS. The conventional Maximum Power Point Tracking (MPPT) algorithm in a micro-converter architecture uses one scalar MPPT for each PV module. The scalar algorithm gives no consideration to the interaction between the PV modules and it requires two measurements per each module. On the other hand, the existing MPPT algorithms, including the ES, work based on the estimate of the gradient of the power map. Hence, a non-symmetric power map creates vastly different transients depending on the initial condition and direction of power changes in the system. From the analysis of the multivariable gradient-based ES algorithm we realize that the Hessian of the power map has a dominant role in the closed-loop performance. The Newton algorithm removes the performance dependence on the Hessian. We develop the Newton algorithm based on the ES scheme which includes two main parts: the perturbation matrix to generate the estimate of the Hessian and the dynamic filter to estimate the inverse of the Hessian. We developed the theoretical basis for the multivariable Newton-based ES using the averaging and singular perturbation analysis. We successfully verified the effectiveness of our proposed algorithm on the experimental setup.

Our proposed WECS includes four different parts: (1) wind turbine , (2) gearbox, (3) Induction Generator (IG), and (4) matrix converter. The open-loop dynamics of the WECS has left half-plane poles, but they are very slow which make the response time of the ES even slower. In order to achieve fast closed-loop response and extra features like constant v/f or vector control in the system, we design an inner-loop control based on the concept of Field-Oriented Control (FOC). The combination of the inner-loop controller and the ES algorithm improves the performance of the WECS.

6.1 Towards the Future

Computed power densities in high altitude winds exceed a 10 kW/m^2 seasonal average at the jet streams typical latitudes and altitudes. This is the highest power density for a large renewable energy resource anywhere on Earth. It exceeds the power densities of sunlight, near surface winds, ocean currents, hydropower, tides, geothermal, and other large-scale renewable resources. For comparison, Earth surface solar energy is typically about 0.24 kW/m^2, and Photovoltaic (PV) systems electrical efficiency is several times less than that of wind power. Various systems have been examined to capture this energy, and these include tethered balloons, tethered fixed-winged craft, tethered kites, and rotorcraft.

The wind energy potential is a function of the height above the ground due to the presence of the so-called “wind shear”, i.e., the growth of wind speed with elevation. An example of wind shear curve is shown in Figure 6.1. High power densities would be uninteresting if only a small amount of total power were available. However, wind power is roughly 100 times the power used by all human civilization. Removing 1% of high altitude winds available energy is not expected to have adverse environmental consequences. High altitude winds are a very attractive potential power source, because this vast energy is high density and persistent. Furthermore, high altitude winds are typically just a few kilometers away from energy users. No other energy source combines potential resource size, density,

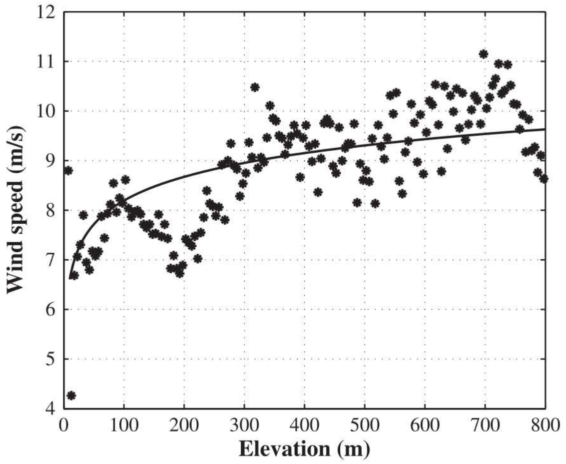

Figure 6.1: A typical wind shear model (asterisks) experimental data and (sloid line) wind shear model [27].

and proximity so attractively.

Because High Altitude Wind Generators (HAWGs) could move north or south to follow seasonal shifts in wind patterns or power demand, it could be advantageous to have "plug-in" HAWGs at pre-arranged sites along an existing grid 33 kV. The HAWGs envisioned for commercial power production have a rated capacity in the 3–30 MW range. To supply all the US energy needs, airspace for power generation is calculated to restrict far less airspace than is already restricted from civil aviation for other purposes.

6.2 History

The idea of using airborne windmills for electricity generation was investigated at least as far back as the 1930s. The company Sheldahl, Inc., placed a French-made generator (4-blade, 2 m diameter) on a tethered balloon in the late 1960s and generated about 350 W of power. The idea of harnessing high altitude wind power using a tethered aircraft is as old as the 1970s. Several proposals were placed to the National Science Foundation and the Energy Resources Development Administration in the US in the mid-70s to research the possibility of generating power from an airborne windmill. These were denied because of possible hazards to aircraft and were deemed not to be economical.

6.3 Tethered Kite Generator

The concept of Tethered Kite Generator (TKG) is to use wings, linked to the ground by two cables, to extract energy from wind blowing at higher heights with respect to those of the Wind Turbines (WTs). The flight of the wings is suitably driven by an automatic control unit. Wind energy is collected at ground level by converting the traction forces acting on the wing lines into electrical power with the use of suitable rotating mechanisms and electric generators placed on the ground. The wings are able to exploit wind flows at higher altitudes than those of the WTs (up to 1000 m, using 1200–1500 m cables), where stronger and more constant wind can be found basically everywhere in the world. In this way, high altitude wind energy can be harvested with the minimal effort in terms of generator structure, cost, and land occupation.

In wind turbines, the outermost 30% of the blade surface approximately contributes for 80% of the generated power. The main reason is that the effective wind speed on the blade is higher in the outer part, and wind power grows with the cube of the effective wind speed. Yet, the structure of the WT determines most of its cost and imposes a limit to the elevation that can be reached. To understand the concept of tethered kite, one can imagine removing all the bulky structure of a WT and just keeps the outer part of the blades, which becomes a much lighter wing flying fast in crosswind conditions (Figure 6.2), connected to the ground by the cables. Thus, the rotor and the tower of the present wind technology are replaced by the wing and its cables, realizing a wind generator that is largely lighter and cheaper. For example, in a 2 MW wind turbine, the weight of the rotor and the tower is typically about 300 tons. A TKG of the same rated power can be obtained using a 500 m^2 wing and 1000 m cables, with a total weight of about 2–3 tons only.

The TKG operating principle is to mechanically drive a ground-based elec-

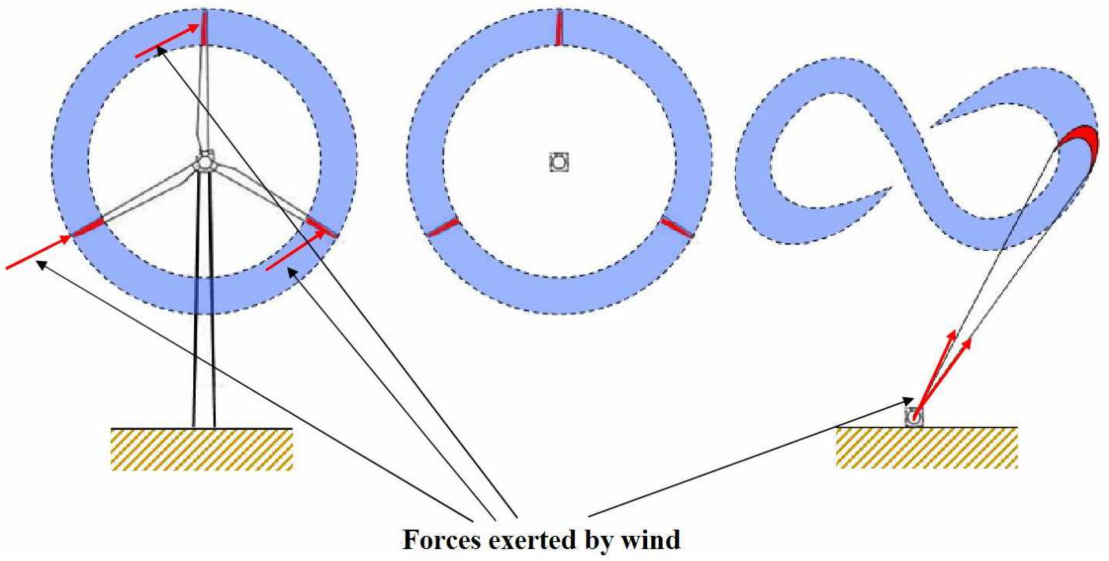

Figure 6.2: Basic concept of TKG technology [27].

tric generator using a tethered kite, instead of attempting to locate a WT system at high altitudes. On the ground-station the lower portion of the tether is wound around a drum connected to the generator. Energy is extracted from high altitude by letting the kite fly at a lying-eight orbit with high crosswind speed (Figure 6.3). During the fast crosswind motion the kite develops a large pulling force, and thus the generator generates electricity while the kite pulls the tether out of the ground-station. Then the kite is controlled so, that the pulling force is reduced, and the lower part of the tether is wound back onto the drum using the generator as a motor. This cycle is repeated, and thus the system is called a pumping kite generator. It should be emphasized that the requirement for energy generation with this system is that the kite dynamics must be controlled to get large and small pulling force alternately.

Figure 6.4 shows a comparison between the power curves of a 2 MW, 500 m^2 TKG and a 2 MW, 90 m diameter WT. The rated power is reached with 9 m/s wind speed by the TKG, while about 13 m/s are needed by the WT. Moreover, the WT cut-out speed is about 25 m/s, while about 40 m/s is obtained for the TKG.

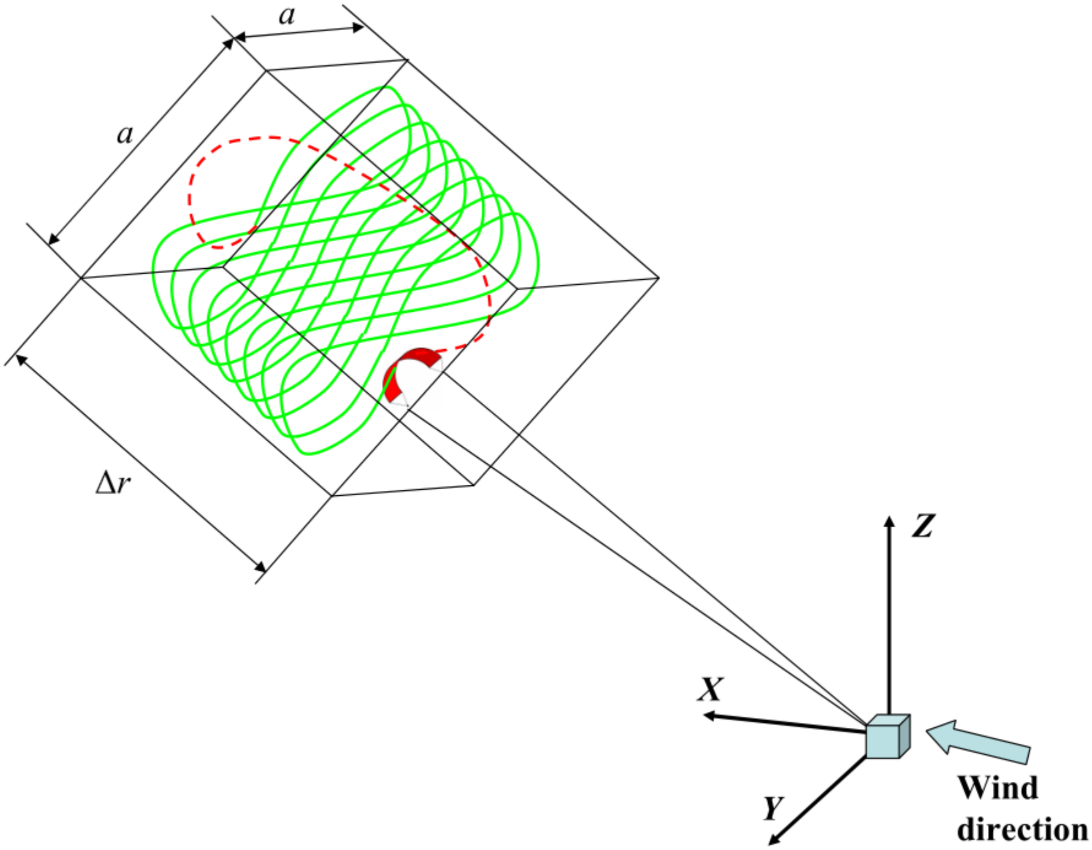

Figure 6.3: Wing glide maneuver (solid) traction and (dashed) passive phases. The kite is kept inside a polyhedral space region whose dimensions are $(a \times a \times \Delta r)$ meters [27].

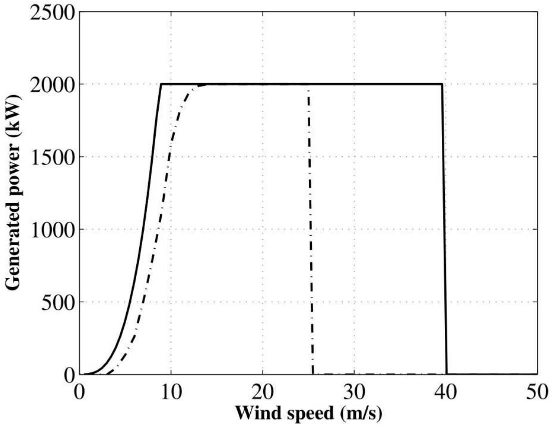

Figure 6.4: Typical power curve of (solid line) TKG and (dashed) WT [27].

6.4 Energy Storage Systems

High altitude wind generators will have a relatively high availability, around 80%. Reliability and peak premium sales could be enhanced by a link to a pumped storage facility for off-peak filling/storage and peak-release energy sales and delivery. Energy could be stored as hydrogen gas produced from electrolysis, or as water pumped-back and re-released for hydroelectric generation.

Electric utilities want constantly available “dispatchable” power, which cannot be provided economically if capacity factors are low, such as the 30% that is typical of the WT sites. However, with the high capacity factors, such as 80%, that are expected at average HAWG sites in the US and many other places in the world (especially in the mid-latitudes), this dispatchable electricity becomes economical. This is because the expected storage requirement in connection with HAWG derived electrical energy is required for only the shorter periods when HAWGs are grounded due to inadequate winds or bad storms. Pumped water storage, where available, is a very economical means used now for such temporary storage. A well known example is used by Pacific Gas and Electric Company in California to pump water up to a high lake during low demand hours and then have that water generate electricity at high demand times on the way back to a lower lake.

Existing hydroelectric power at dams may be considered to be the equivalent of pumped water storage facilities by deliberately phasing in and out generation in complementary fashion to wind availability at a nearby HAWG. In that combination the combined output could be dispatchable power with as much as four times the capacity of the existing hydroelectric site.

Compressed Air Energy Storage (CAES) is another energy storage means presently coming into use. In special circumstances, where pumping compressed air into existing large caves or porous rock strata is feasible, it may well be especially economic. Commercial tanks built for the purpose may be the most economic storage means where very short-term energy storage is needed.

6.5 Economical Considerations

Annual Operating Expenses (AOE) includes Land Lease Costs (LLC), Operations & Maintenance (O&M) and Levelized Replacement/Overhaul Costs (LRC). AOE projections are necessarily subjective, since no plant like this currently exists. O&M costs are derived from an $82,000/yr estimate for a 3.4 MW HAWG, multiplied by 29.4 HAWGs for a 100 MW plant. Life-limited components are anticipated to require replacement at 10 years and 20 years. Tether longevity is a risk. Replacement cost is estimated at 80% of the initial capital cost for the whole system. Expressed in per kWh terms, the AOE for the Topeka, Detroit, and San Diego sites are estimated at $0.0102/kWh, $0.0103/kWh, and $0.0129/kWh, respectively.

Wind industry has the largest share of renewable energy generation, apart from hydropower, with a yearly global growth of the installed capacity of about 30% in the last years. Indeed, only by exploiting 20% of the world land sites that are profitable for the actual wind technology, based on WTs, in principle, the global energy demand could be supplied. However, the current wind technology has limitations in terms of energy production costs, which are still too high with respect to fossil sources, and in terms of land occupation, because wind farms based on modern WTs with 2–3 MW rated power have an average power density of 3.5–4 MW/km^2, about 200–300 times lower than that of large thermal plants.

Table 6.1: Projected cost in 2030 of energy from different sources [27].

Source	Minimal estimated ($/MWh)	Maximal estimated ($/MWh)	Averaged estimated ($/MWh)
Coal	25	50	34
Gas	37	60	47
Nuclear	21	31	29
WT	35	95	57
PV	180	500	325
TKG	10	48	20

Wind turbines already operate at a height of about 150 m over the ground, a value hardly improvable, because of structural constraints that give rise to technological and economical limits. Yet the wind speed generally increases with the height above the ground: for example, at the height of 500–1000 m, the mean wind power density is about four times the one at 50–150 m. This point suggests that a breakthrough in wind energy generation can be realized by capturing wind power at altitudes over the ground that cannot be reached by wind turbines.

The content of this chapter is borrowed from [1, 2, 26, 27, 30, 34, 75, 79]

Bibliography

[1] M. Ahmed, A. Hably, and S. Bacha, "Power maximization of a closed-orbit kite generator system," in *Proc. of the IEEE Conf. on Decision and Control and European Control Conf.*, 2011.

[2] ——, "High altitude wind power systems: A survey on flexible power kites," in *Proc. of the International Conf. on Electrical Machines*, 2012.

[3] R. Airapetyan, "Continuous newton method and its modification," *Applicable Analysis*, vol. 73, pp. 463–484, 1999.

[4] P. M. Anderson and A. Bose, "Stability simulation of wind turbine systems," *IEEE Trans. Power App. Syst.*, vol. PAS-102, pp. 3791–3795, 1983.

[5] K. B. Ariyur and M. Krstić, "Analysis and design of multivariable extremum seeking," in *Proc. of the American Control Conf.*, 2002.

[6] ——, *Real-Time Optimization by Extremum Seeking Feedback.* Wiley-Interscience, 2003.

[7] A. Banaszuk, K. B. Ariyur, M. Krstić, and C. A. Jacobson, "An adaptive algorithm for control of combustion instability," *Automatica*, vol. 40, pp. 1965–1972, 2004.

[8] S. M. Barakati, "Modeling and controller design of a wind energy conversion system including a matrix converter," Ph.D. dissertation, Department of Electrical and Computer Engineering, University of Waterloo, 2008.

[9] S. M. Barakati, M. Kazerani, and J. D. Aplevich, "Maximum power tracking control for a wind turbine system including a matrix converter," *IEEE Trans. Energy Conversion*, vol. 24, pp. 705–713, 2009.

[10] R. Becker, R. King, R. Petz, and W. Nitsche, "Adaptive closed-loop separation control on a high-lift configuration using extremum seeking," *AIAA Journal*, vol. 45, pp. 1382–1392, 2007.

[11] A. Bellini, G. Figalli, and G. Ulivi, “Analysis and design of a microcomputer-based observer for an induction machine,” *Automatica*, vol. 24, pp. 549–555, 1988.

[12] A. Bratcu, I. Munteanu, S. Bacha, D. Picault, and B. Raison, “Cascaded DC-DC converter photovoltaic systems: power optimization issues,” *IEEE Trans. Ind. Electron.*, vol. 58, pp. 403–411, 2011.

[13] A. I. Bratcu, E. C. Iulian Munteanu, and S. Epure, “Energetic optimization of variable speed wind energy conversion systems by extremum seeking control,” in *The International Conf. on “Computer as a Tool”*, 2007.

[14] J. Bratt, “Grid connected PV inverters: Modeling and Simulation,” Master’s thesis, Department of Electrical and Computer Engineering, San Diego State University, 2011.

[15] S. Brunton, C. Rowley, S. Kulkarni, and C. Clarkson, “Maximum power point tracking for photovoltaic optimization using ripple-based extremum seeking control,” *IEEE Trans. Power Electron.*, vol. 25, pp. 2531–2540, 2010.

[16] R. Cardenas, R. Pena, J. Clare, and P. Wheeler, “Analytical and experimental evaluation of a WECS based on a cage induction generator fed by a matrix converter,” *IEEE Trans. Energy Conversion*, vol. 26, pp. 204–215, 2011.

[17] D. Carnevale, A. Astolfi, C. Centioli, S. Podda, V. Vitale, and L. Zaccarian, “A new extremum seeking technique and its application to maximize RF heating on FTU,” *Fusion Engineering and Design*, vol. 84, pp. 554–558, 2009.

[18] D. S. H. Chan and J. C. H. Phang, “Analytical methods for the extraction of solar-cell single- and double-diode model parameters from I-V characteristics,” *IEEE Trans. Electron Devices*, vol. ED-34, pp. 286–293, 1987.

[19] M. Chinchilla, S. Arnaltes, and J. C. Burgos, “Control of permanent-magnet generators applied to variable-speed wind-energy systems connected to the grid,” *IEEE Trans. Energy Conversion*, vol. 21, pp. 130–135, 2006.

[20] J.-Y. Choi, M. Krstić, K. B. Ariyur, and J. S. Lee, “Extremum seeking control for discrete-time systems,” *IEEE Trans. Automat. Contr.*, vol. 47, pp. 318–323, 2002.

[21] J. Cochran, E. Kanso, S. D. Kelly, H. Xiong, and M. Krstić, “Source seeking for two nonholonomic models of fish locomotion,” *IEEE Trans. Robot. Automat.*, vol. 25, pp. 1166–1176, 2009.

[22] J. Cochran and M. Krstić, “Nonholonomic source seeking with tuning of angular velocity,” *IEEE Trans. Automat. Contr.*, vol. 54, pp. 717–731, 2009.

[23] S. V. Dhople, J. L. Ehlmann, A. Davoudi, and P. L. Chapman, "Multiple-input boost converter to minimize power losses due to partial shading in photovoltaic modules," in *Proc. of IEEE Energy Conversion Congress and Exposition*, 2010.

[24] R. W. Erickson and D. Maksimović, *Fundamentals of Power Electronics.* New York: Springer-Verlag, 2001.

[25] T. Esram and P. Chapman, "Comparison of photovoltaic array maximum power point tracking techniques," *IEEE Trans. Energy Conversion*, vol. 22, pp. 439–449, 2007.

[26] L. Fagiano and M. Milanese, "Airborne wind energy: an overview," in *Proc. of the American Control Conf.*, 2012.

[27] L. Fagiano, "Control of tethered airfoils for highaltitude wind energy generation," Ph.D. dissertation, Doctorate School, Polytechnic University of Turin, 2009.

[28] A. Ghaffari, M. Krstić, and D. Nešić, "Multivariable Newton–based extremum seeking," *Automatica*, vol. 48, pp. 1759–1767, 2012.

[29] A. Ghaffari, S. Seshagiri, and M. Krstić, "Power optimization for photovoltaic micro-converters using multivariable gradient-based extremum-seeking," in *Proc. of the American Control Conf.*, 2012.

[30] J. Gillis, J. Goos, K. Geebelen, J. Swevers, and M. Diehl, "Optimal periodic control of power harvesting tethered airplanes: how to fly fast without wind and without propellor?" in *Proc. of the American Control Conf.*, 2012.

[31] M. Guay, M. Perrier, and D. Dochain, "Adaptive extremum seeking control of nonisothermal continuous stirred reactors," *Chemical Engineering Science*, vol. 60, pp. 3671–3681, 2005.

[32] D. P. Hohm and M. E. Ropp, "Comparative study of maximum power point tracking algorithms," *Progress in Photovoltaics: Research and Applications*, vol. 11, pp. 47–62, 2003.

[33] L. Huber and D. Borojevic, "Space vector modulated three-phase to three-phase matrix converter with input power factor correction," *IEEE Trans. Ind. Applicat.*, vol. 31, pp. 1234–1246, 1995.

[34] M. W. Isaacs, J. B. Hoagg, I. I. Hussein, and D. Olinger, "Retrospective cost adaptive control for a ground tethered energy system," in *Proc. of the IEEE Conf. on Decision and Control and European Control Conf.*, 2011.

[35] S. Jain and V. Agarwal, "Comparison of the performance of maximum power point tracking schemes applied to single-stage grid-connected photovoltaic systems," *IET Electric Power Applications*, vol. 1, pp. 753–762, 2007.

[36] K. E. Johnson, L. Y. Pao, M. J. Balas, and L. J. Fingersh, "Control of variable-speed wind turbines: standard and adaptive techniques for maximizing energy capture," *IEEE Control Syst. Mag.*, vol. 26, pp. 70–81, 2006.

[37] S. J. Johnson and C. P. C. van Dam, "Active load control techniques for wind turbines," Sandia National Laboratories, Tech. Rep., 2008.

[38] M. K. Kazimierczuk, *Pulse-width Modulation DC-DC Power Converters*. John Wiley and Sons, 2008.

[39] S. M. R. Kazmi, H. Goto, H.-J. Guo, and O. Ichinokura, "A novel algorithm for fast and efficient speed-sensorless maximum power point tracking in wind energy conversion systems," *IEEE Trans. Ind. Electron.*, vol. 58, pp. 29–36, 2011.

[40] H. K. Khalil, *Nonlinear Systems*, 2nd ed. NJ: Englewood Cliffs: Prentice Hall, 1996.

[41] N. J. Killingsworth, S. M. Aceves, D. L. Flowers, F. Espinosa-Loza, and M. Krstić, "HCCI engine combustion-timing control: Optimizing gains and fuel consumption via extremum seeking," *IEEE Trans. Contr. Syst. Technol.*, vol. 17, pp. 1350–1361, 2009.

[42] N. Killingsworth and M. Krstić, "Auto-tuning of PID controllers via extremum seeking," in *Proc. of the American Control Conf.*, 2005.

[43] M. Komatsu, H. Miyamoto, H. Ohmori, and A. Sano, "Output maximization control of wind turbine based on extremum control strategy," in *Proc. of American Control Conf.*, 2001.

[44] P. C. Krause, O. Wasynczuk, and S. D. Sudhoff, *Analysis of Electric Machinery and Drive Systems*. Wiley-Interscience, 2002.

[45] M. Krstić and H.-H. Wang, "Stability of extremum seeking feedback for general nonlinear dynamic systems," *Automatica*, vol. 36, pp. 595–601, 2000.

[46] V. Kumar, R. R. Joshi, and R. C. Bansal, "Optimal control of matrix-converter-based WECS for performance enhancement and efficiency optimization," *IEEE Trans. Energy Conversion*, vol. 24, pp. 264–273, 2009.

[47] P. Lei, Y. Li, Q. Chen, and J. Seem, "Extremum seeking control based integration of MPPT and degradation detection for photovoltaic arrays," in *Proc. of American Control Conf.*, 2010.

[48] R. Leyva, C. Alonso, I. Queinnec, A. Cid-Pastor, D. Lagrange, and L. Martinez-Salamero, “MPPT of photovoltaic systems using extremum seeking control,” *IEEE Trans. Aerosp. Electron. Syst.*, vol. 42, pp. 249–258, 2006.

[49] A. D. Luca and G. Ulivi, “Dynamic decoupling of voltage frequency controlled induction motors,” in *the 8th Int. Conf Analysis Optimiz. Syst.*, 1988.

[50] ——, “Design of exact nonlinear controller for induction motors,” *IEEE Trans. Automat. Contr.*, vol. 34, pp. 1304–1307, 1989.

[51] L. Luo and E. Schuster, “Mixing enhancement in 2d magnetohydrodynamic channel flow by extremum seeking boundary control,” in *Proc. of the American Control Conf.*, 2009.

[52] R. Marino, S. Peresada, and P. Valigi, “Adaptive input-otput linearizing control of induction motors,” *IEEE Trans. Automat. Contr.*, vol. 38, pp. 208–221, 1993.

[53] M. Miyatake, M. Veerachary, F. Toriumi, N. Fuji, and H. Ko, “Maximum power point tracking of multiple photovoltaic arrays: a PSO approach,” *IEEE Trans. Aerosp. Electron. Syst.*, vol. 47, pp. 367–380, 2011.

[54] W. H. Moase, C. Manzie, and M. J. Brear, “Newton-like extremum-seeking for the control of thermoacoustic instability,” *IEEE Trans. Automat. Contr.*, vol. 55, pp. 2094–2105, 2010.

[55] S. Moura and Y. Chang, “Asymptotic convergence through Lyapunov-based switching in extremum seeking with application to photovoltaic systems,” in *Proc. of American Control Conf.*, 2010.

[56] D. Nešić, Y. Tan, W. H. Moase, and C. Manzie, “A unifying approach to extremum seeking: adaptive schemes based on estimation on the estimation of derivatives,” in *Proc. of IEEE Conf. on Decision and Control*, 2010.

[57] B. Ozpineci and L. M. Tolbert, “Simulink implementation of induction machine model - a modular approach,” in *. IEEE International Conf. on Electric Machines and Drives*, 2003.

[58] F.-S. Pai, R.-M. Chao, S. H. Ko, and T.-S. Lee, “Performance evaluation of parabolic prediction to maximum power point tracking for PV array,” *IEEE Trans. on Sustainable Energy*, vol. 2, pp. 60–68, 2011.

[59] T. Pan, Z. Ji, and Z. Jiang, “Maximum power point tracking of wind energy conversion systems based on sliding mode extremum seeking control,” in *Proc. IEEE Energy 2030 Conf.*, 2008.

[60] L. Y. Pao and K. E. Johnson, "Control of wind turbines," *IEEE Control Syst. Mag.*, vol. 31, pp. 44–62, 2011.

[61] G. Petrone, G. Spagnuolo, and M. Vitelli, "A multivariable perturb-and-observe maximum power point tracking technique applied to a single-stage photovoltaic inverter," *IEEE Trans. Ind. Electron.*, vol. 58, pp. 76–84, 2011.

[62] J. C. H. Phang, D. S. H. Chan, and J. R. Phillips, "Accurate analytical method for the extraction of solar cell model parameters," *Electronics Letters*, vol. 20, pp. 406–408, 1984.

[63] C. A. Ramos-Paja, G. Spagnuolo, G. Petrone, M. Vitelli, and J. Bastidas, "A multivariable MPPT algorithm for granular control of photovoltaic systems," in *Proc. of IEEE International Symposium on Industrial Electronics*, 2010.

[64] E. Rogers, "Understanding boost power stages in switchmode power supplies," Texas Instruments, Tech. Rep., 1999.

[65] ——, "Understanding buck power stages in switchmode power supplies," Texas Instruments, Tech. Rep., 1999.

[66] M. A. Rotea, "Analysis of multivariable extremum seeking algorithms," in *Proc. of the American Control Conf.*, 2000.

[67] T. Senjyu, R. Sakamoto, N. Urasaki, T. Funabashi, H. Fujita, and H. Sekine, "Output power leveling of wind turbine generator for all operating regions by pitch angle control," *IEEE Trans. Energy Conversion*, vol. 21, pp. 467–475, 2006.

[68] D. Sera, R. Teodorescu, and P. Rodriguez, "PV panel model based on datasheet values," in *Proc. of the IEEE International Symposium on Industrial Electronics*, 2007.

[69] J. G. Slootweg, S. W. H. de Haan, H. Polinder, and W. L. Kling, "General model for representing variable speed wind turbines in power system dynamics simulations," *IEEE Trans. Power Syst.*, vol. 18, pp. 144–151, 2003.

[70] M. S. Stankovic, K. H. Johansson, and D. M. Stipanovic, "Distributed seeking of nash equilibria in mobile sensor networks," in *Proc. of IEEE Conf. on Decision and Control*, 2010.

[71] M. S. Stankovic and D. M. Stipanovic, "Extremum seeking under stochastic noise and applications to mobile sensors," *Automatica*, vol. 46, pp. 1243–1251, 2010.

[72] Y. Tan, D. Nešić, and I. Mareels, "On non-local stability properties of extremum seeking control," *Automatica*, vol. 42, pp. 889–903, 2006.

[73] A. R. Teel and D. Popovic, “Solving smooth and nonsmoooth multivariable extremum seeking problems by the methods of nonlinear programming,” in *Proc. of the American Control Conf.*, 2001.

[74] G. Vachtsevanos and K. Kalaitzakis, “A hybrid photovoltaic simulator for utility interactive studies,” *IEEE Trans. Energy Conversion*, vol. EC-2, pp. 227–231, 1987.

[75] C. Vermillion, T. Grunnagle, and I. Kolmanovsky, “Modeling and control design for a prototype lighter-than-air wind energy system,” in *Proc. of the American Control Conf.*, 2012.

[76] H.-H. Wang and M. Krstić, “Extremum seeking for limit cycle minimization,” *IEEE Trans. Automat. Contr.*, vol. 45, pp. 2432–2437, 2000.

[77] H.-H. Wang, S. Yeung, and M. Krstić, “Experimental application of extremum seeking on an axial-flow compressor,” *IEEE Trans. Contr. Syst. Technol.*, vol. 8, pp. 300–309, 2000.

[78] P. W. Wheeler, J. Rodriguez, J. C. Clare, L. Empringham, and A. Weinstein, “Matrix converters: A technology review,” *IEEE Trans. Ind. Electron.*, vol. 49, pp. 276–288, 2002.

[79] P. Williams, B. Lansdorp, and W. Ockels, “Optimal cross-wind towing and power generation with tethered kites,” in *Proc. of the AIAA Guidance, Navigation and Control Conf. and Exhibit*, 2007.

[80] B. Wu, Y. Lang, N. Zargari, and S. Kouro, *Power Conversion and Control of Wind Energy Systems.* Wiley-Interscience, 2011.

[81] C. Zhang, D. Arnold, N. Ghods, A. Siranosian, and M. Krstić, “Source seeking with nonholonomic unicycle without position measurement and with tuning of forward velocity,” *Systems & Control Letters*, vol. 56, pp. 245–252, 2007.

[82] S. Zhang, K. J. Tseng, and T. D. Nguyen, “Modeling of AC-AC matrix converter for wind energy conversion system,” in *IEEE Conf. on Industrial Electronics and Applications*, 2009.